Research on Final Beam Transport and Beam-Target Interaction in Heavy Ion Inertial Confinement Fusion

Tetsuo Someya

A dissertation submitted to the Utsunomiya University in conformity with the requirements for the degree of Doctor of Philosophy.

Utsunomiya, Tochigi, Japan
March 2006

dedicated to my dear wife AKIKO

Contents

List of Figures

List of Tables

Chapter 1

Introduction

Our energy comes mainly from fossil fuels and nuclear fission. Both have undesirable consequences. Nuclear fission is leaving us with an accumulating supply of depleted nuclear fuel rods, which will remain radioactive for centuries. And though well-designed nuclear reactors are inherently safe, a nuclear accident as happened at Chernobyl can be disastrous.

Fossil fuels, oil, gas and coal power our cars and electric generating plants, polluting the air with COx and sulfur emissions. Sulfur dioxide combines with atmospheric oxygen to form sulfur trioxide, which reacts with water vapor to form sulfuric acid. The result is acid rain, which some scientists think could be causing damage to forests on the earth.

Other energy sources, such as solar, wind, ocean wave and geothermal are under development, but none of these will be able to supply the large amounts required in the foreseeable future.

More efficient electrical devices and building insulation (conservation) can reduce the rate of increase of demand but cannot generate energy. All our energy comes from the sun. Our problem is to convert enough of it to useful forms.

1.1 Fusion

Our best hope for an abundant energy source here on earth is nuclear fusion. While it is nuclear (involving the nuclei of atoms) it is quite different from the presently used nuclear fission. Fission starts with a heavy element that has large atoms, such as uranium. Uranium nuclei, orbited by clouds of

electrons, are so large that they are unable to remain in one piece and tend to lose fragments. These emitted fragments dissipate their energy as heat, but they are still radioactive and continue to break down into smaller atoms in time. This is the fission process (see Fig. 1.1), and these radioactive fragments create a serious waste disposal problem.

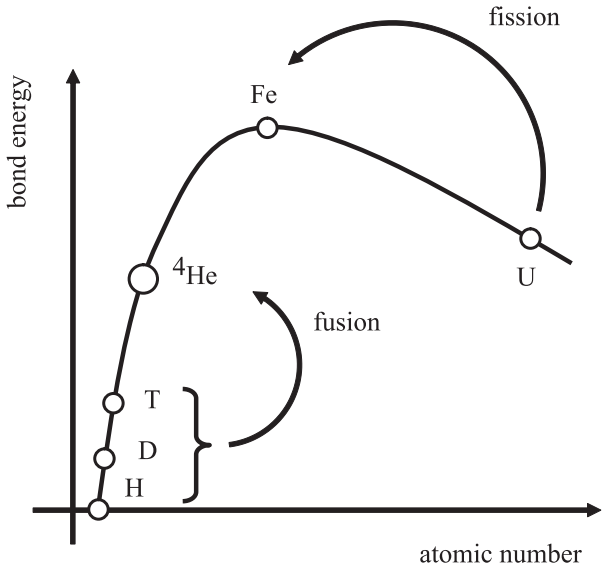

Figure 1.1: Nuclear fission and fusion.

Nuclear fusion begins instead with atoms of the lightest element, hydrogen, abundant in water. Fuel cost is negligible. Instead of breaking them apart, hydrogen nuclei are fused together to form non-radioactive helium and neutrons as by-products. Fusion is not easy to achieve, though it happens naturally in stars because gravity causes large amounts of gaseous matter in space to collapse in upon itself. The hydrogen bomb works on fusion, but the energy release is uncontrolled.

The central problem for physicists and engineers working on controlled nuclear fusion is due to the electrical nature of matter. Nuclei consist of positively charged protons and neutral neutrons, and are surrounded by negatively charged electrons. From basic electricity, like charges repel while opposite charges attract. As two nuclei are brought together, the force of

repulsion becomes immense. This keeps matter from collapsing but makes fusion difficult. Large amounts of energy are needed to force nuclei together. When nuclei are close enough, another basic force (the "strong force") within the nucleus itself causes them to attract, overcoming the electric force (overcome the Coulomb barrier), and they fuse into a heavier element (see Fig. 1.2). In fusing, some mass is converted to energy according to the Einstein's famous formula: $E = mc^2$.

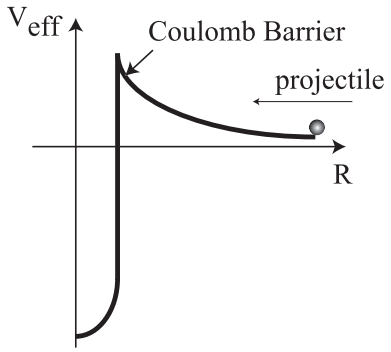

Figure 1.2: The Coulomb barrier.

In order to be applied a strong force within the nucleus, the nuclei and electrons must be separately. Therefore, the atom (the hydrogen etc...) temperature should be high (10 to 100 million degrees). Under those conditions, first of all, the electrons will be stripped away from the nuclei. We will have a system with no atoms, just electrically charged nuclei and free electrons. This is called a plasma. Nuclei and electrons will be moving very rapidly in random directions. If the plasma is hot enough, nuclei overcome the electrical barrier, undergo fusion reactions, and produce more energy, increasing the plasma's temperature further.

The problem is that the very hot plasma cannot be kept in a container, because any solid container would be vaporized at temperatures of millions of degrees. If the plasma is not contained, then as it is heated it will just dissipate, like cigarette smoke into a room. There are three approaches to containing the plasma:

- Gravity confinement

- Confinement by strong magnetic field (magnetic confinement fusion)
- Inertial confinement (inertial confinement fusion)

Building a star is impractical because the amount of matter required for gravitational confinement far exceeds that available on earth. However it is impossible to be realize this confinement type on the earth clearly.

The Inertial confinement fusion (ICF) and magnetic confinement fusion (MCF) are two main approach to controlled fusion. While MCF aims for a steady-state plasma confined by a magnetic field, ICF is an inherently pulsed concept, igniting and burning small fuel capsules at a rate of a few Hz. The basic fusion reactions are the same and require similar plasma temperatures, but density and pressure regimes are completely different as shown in Table 1.1.

Table 1.1: Orders of magnitude of ion temperature, number density and pressure for MCF and ICF thermonuclear plasma states.

	MCF	ICF
T (keV)	10	10
n (cm^{-3})	10^{14}	10^{25}
p (bar)	10	10^{12}

1.1.1 Magnetic fusion

The magnetic confinement takes advantage of the very nature of the plasma as a gas of charged particles. In a strong magnetic field, charged particles can move freely only in the direction of the field lines, while transverse motion is nearly suppressed. It is therefore possible to confine the plasma particles in devices with appropriate magnetic field configurations as the tokamaks and ITER and so on.

In magnetic confinement, the density of the confined plasma is given by the strength of the magnetic field. The essential observation is that the kinetic pressure of the plasma cannot be larger than a fraction β_{max} of the magnetic field pressure. The value of β_{max} depends on details of the configuration and is typically smaller than 10 % for a tokamak. The magnetic

field is limited to about 100 kG by material strength considerations. On the other hand, plasma temperature have to be in the order of 10 keV. This leads to maximum particle density the order of 10^{14} cm^{-3} for a tokamak reactor. This density is five orders of magnitude below that of air at standard conditions. Plasma with such low density is practically transparent to their bremsstrahlung radiation and to the fusion neutrons.

1.1.2 Inertial confinement fusion

Inertial confinement involves no external means of confinement, but exclusively relies on mass inertia. Suppose a fusion plasma has been assembled in a small spherical volume. Mass inertia then keeps it together for a short moment given by the time a sound wave needs to travel from the surface to the center. Fusion burn bas to occur in this period of time.

In contrast to the stationary confinement in MCF, the confinement time is very short in ICF (typically one tenth of a nanosecond) [1]. This bas two immediate consequences:

- In order to burn a substantial part of the fuel in such a short time, one has to apply extremely high plasma density to achieve high reaction rates. The DT fuel has to be compressed to about 1000 times its solid density.
- Power production by inertial confinement is necessarily a pulsed process. Ignition and burn of small amounts of fuel have to occur repetitively, and the energy is released in a sequence of micro-explosions.

This required density can be obtained by imploding spherical shells by particle beam irradiation or laser irradiation [2]. This scheme is called direct-drive ICF. The another scheme is that the capsule ablation is driven by thermal radiation inside a cavity, the so-called "hohlraum". This scheme is called indirect-drive ICF [3–8].

1.1.3 Heavy Ion Fusion

Figure 1.3 shows the HIF concept. The HIBs are extracted from ion sources. The extracted HIBs are transported and accelerated up to 10 GeV by RF and/or induction accelerator modules. After the HIBs attain the high energy, the beam pulse is longitudinally compressed for the effective pellet implosion

[9]. Finally, the intense-HIBs are transversely focused and transported to the target pellet in the reactor environment.

Figure 1.4 shows the stages of a HIB direct-drive implosion. Irradiation leads to surface ablation and drives the fuel implosion. As the imploding material stagnates in the center its kinetic energy is converted into inertial energy. The fuel consists of a high compressed shell enclosing a hot spot of igniting fuel in the center. A burn wave starting from the hot spot then ignites the whole fuel, which explodes.

Figure 1.5 present the hohlraum target. It is cylindrically symmetric with respect to a horizontal axis. The cavity wall is made of gold or other high-Z materials. The cavity is heated by heavy ion beam or laser, entering through holes on the axis and shining on its inner surface. The fuel capsule is then driven by X-ray emerging from heated high Z materials. In this scheme, the heavy ion beam or laser do not drive the fuel capsule directly.

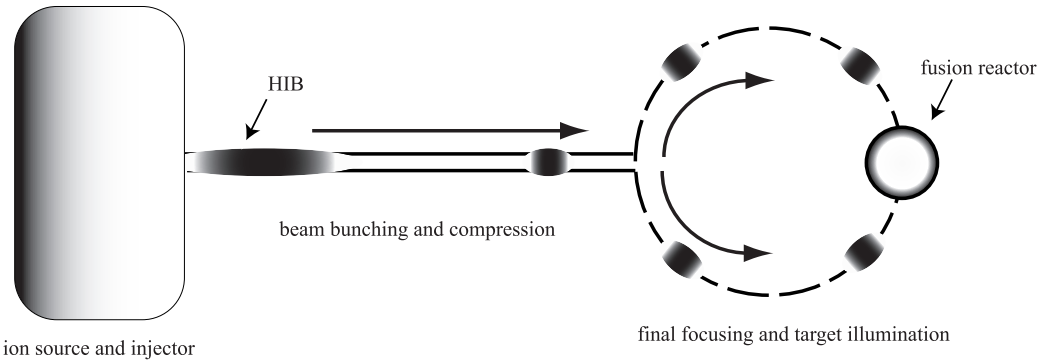

Figure 1.3: Schematic view of HIF concept.

1.2 Lawson criteria

To keep a fusion reaction, a fuel plasma should be confined for a while. We know a necessary confinement time to keep the fusion reaction from the Lawson criteria. Here, we define a confinement time τ sec, a number density n $1/\mathrm{m}^3$, a plasma temperature T keV. The condition is as follows:

$$n\tau \;>\; 10^{20}. \tag{1.1}$$

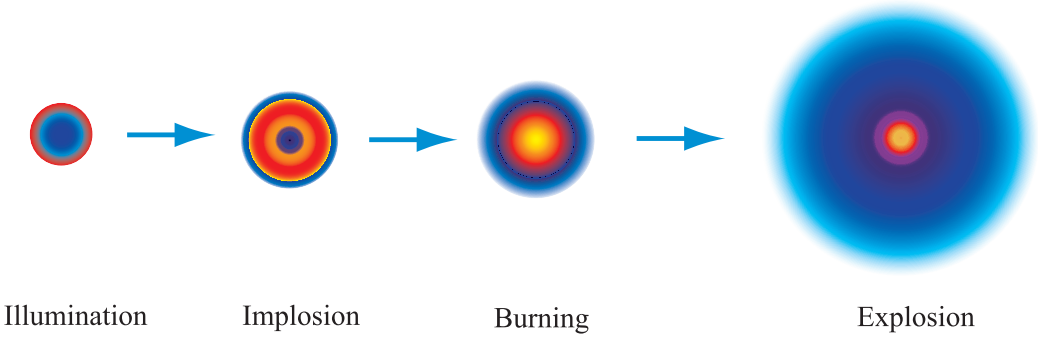

Figure 1.4: Inertial confinement fusion concept

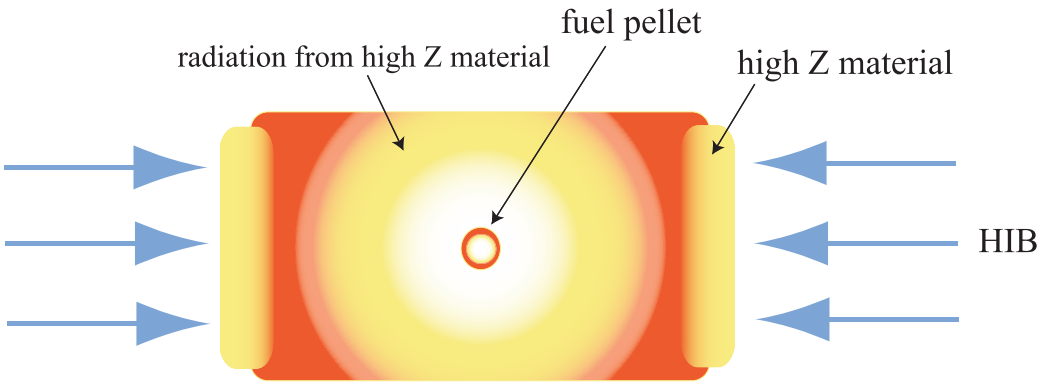

Figure 1.5: Indirect-driven pellet inertial confinement fusion

We define a fusion output energy E_{out},

$$E_{out} = \frac{n^2}{4}\langle\sigma\nu\rangle_{DT}\tau E_f, \tag{1.2}$$

Here, τ and E_f are a plasma confinement time and fusion energy per one reaction (17.6 MeV for DT reaction).

We define that a input energy to heat the plasma temperature T is E_{inp},

$$\begin{aligned} E_{inp} &= \frac{3}{2}nkT_i + \frac{3}{2}nkT_e \\ &= 3nkT. \end{aligned} \tag{1.3}$$

Here k, T_i and T_e are the Boltzman constant, an ion temperature and an electron temperature, respectively. From Eqs. 1.2 and 1.3, the requirement

condition is $E_{out} > E_{inp}$. Therefore,

$$\frac{n^2}{4}\langle\sigma\nu\rangle_{DT}\tau E_f \;>\; 3nkT, \tag{1.4}$$

$$n\tau \;>\; \frac{12kT}{\langle\sigma\nu\rangle_{DT}E_f}. \tag{1.5}$$

If the plasma temperature is $T = 10$ keV, we can lead Eq. 1.1. The Lawson criteria means that the requirement confinement time need 1 sec if the plasma density is 10^{20} m^{-3}.

Next, we introduce a ρR condition to be done an effective fuel ignition. Here ρ and R are a target density and radius, respectively. We define the confinement time τ and a sound velocity C_s,

$$\tau \;\approx\; \alpha\frac{R}{C_s}, \tag{1.6}$$

$$C_s \;=\; \sqrt{\frac{kT}{m_i}}. \tag{1.7}$$

The α and m_i are constant value ($< 1.$) and an ion mass. Then we apply the Lowson criteria,

$$\begin{aligned} n\tau &\approx \frac{\rho}{m_i}\alpha\frac{R}{C_s} \\ &= \frac{\rho R}{4m_iC_s}. \end{aligned} \tag{1.8}$$

Therefore,

$$\rho R \;=\; 4n\tau\sqrt{m_ikT_i}. \tag{1.9}$$

Here, we calculate the ρR using this example condition: kT is 10 keV, m_i is $2.5 \times 1.67 \times 10^{-27}$ kg. Then we can get,

$$\rho R \;>\; 1 \sim 2[g/cm^2]. \tag{1.10}$$

The Eq. 1.10 is important condition for an inertial confinement fusion in order to achieve an effective fuel ignition.

1.3 Purposes of this thesis

This paper contains the following chapters: In Chapter 2,a heavy ion beam (HIB) final transport is focused and studied. In the HIB final transport, the key factors are as follows: a final small focal radius (a few mm), a low emittance growth relating to a HIB particle energy and a momentum divergences, a HIB space charge and a current neutralizations, an electrostatic and electromagnetic instabilities, and collision effects between the HIB and a background reactor gas. Therefore, we should establish a charged-particle-beam-transport control method for the above purposes. The results demonstrate that the heavy ion beam propagates efficiently and is focused well through an insulator beam guide, which may be made of one kind of ceramics and may absorb a part of reactor gas leaked to a beam port.

Chapter 3 shows a HIB-target interaction. In HIB ICF, a beam irradiation non-uniformity on a direct-driven fuel pellet must be suppressed less than few % in order to achieve a symmetric fuel pellet implosion. Therefore, a multi-HIB illumination is required to achieve a low beam non-uniformity in the pellet implosion. On the other hand, the total HIB number should be restricted to a realistic number, for example, less than a few hundred beams. Therefore, in this study, we simulate a HIB illumination on the spherical direct-driven target using 12, 20, 32, 60, 92 and 120-beam irradiation systems. The simulation results present that the HIB deposition energy RMS non-uniformity on the target is suppressed to a low value: for example, less than 2.0 % in the case of the 32 or more HIB-illumination system.

In Chapter4, a direct-indirect mixture implosion mode is proposed and discussed in heavy ion beam (HIB) inertial confinement fusion (HIF) in order to release sufficient fusion energy in a robust manner. On the other hand, the HIB illumination non-uniformity depends strongly on a target displacement gdzh in a reactor. In a direct-driven implosion mode dz of $\sim$ 20 μm was tolerance and in an indirect-implosion mode dz of $\sim$ 100 μm was allowable [10–13]. In the direct-indirect mixture mode target, a low-density foam layer is inserted, and radiation energy is confined in the foam layer. In the foam layer the radiation transport is expected in the lateral direction for the HIB illumination non-uniformity smoothing. Two-dimensional implosion simulations are performed, and show that the HIB illumination non-uniformity is well smoothed.

At last, the results mentioned above and a prospect of the HIF system are summarized as a conclusion of this thesis in Chapter 5.

Chapter 2

Final Beam Transport

2.1 Beam final transport in heavy ion fusion

In addition to laser beams, heavy ion beams (HIB) may be one of promising energy-driver candidates in inertial confinement fusion (ICF). The HIB should be focused and transported against the beam space charge onto a fuel pellet, the radius of which is in the order of mm [14]. Therefore the key issues in HIB ICF include an accelerator design for the intense HIB, a HIB focusing, a HIB transport in a fusion reactor, interactions between neighboring HIBs, a HIB-target interaction, a reactor design and so on. It was confirmed by D.A.Callahan that the interaction between neighboring HIBs is not serious in a HIB fusion reactor [5]. In this chapter the HIB final transport is focused and studied. In the HIB final transport, the key factors are as follows: final small focal radius (a few mm), low emittance growth relating to the HIB particle energy and momentum divergences, HIB space charge and current neutralizations, electrostatic and electromagnetic instabilities, and collision effects between the HIB and a background reactor gas [15, 16]. After the acceleration of beam ions to, for example, about 8-10 GeV, HIB should be transported in a fusion reactor of a few m to 10 m diameter and focused on a few mm fuel pellet (see Fig.2.1) [3]. In a reactor, HIB particles interact with each other and with background plasma or a reactor gas ($\sim$ few mTorr) [17]. In the long distance transport of HIB, the HIB space charge and current should be neutralized, and electrostatic and electromagnetic instabilities should be suppressed. Consequently, we should establish a charged-particle-beam-transport control method for the above purposes.

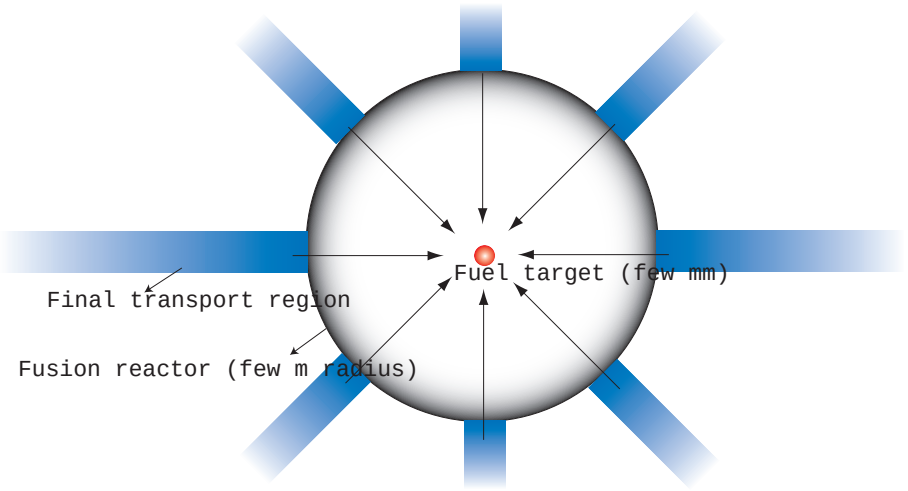

Figure 2.1: Fusion reactor has few m to 10 m radius, and the fuel pellet has a few mm radius.

In our previous papers [18], we proposed a transport system for electron and ion beams through an insulator beam guide. We reported that the particle beam charge is neutralized efficiently by electrons or protons extracted from a plasma generated on the surface insulator guide, and the charged-particle beam is efficiently transported through an insulator beam guide without an increase in a beam radius caused by the beam space charge.

In this section, in order to neutralize the beam space charge and obtain a HIB fine focus in ICF, first we study on a focusing heavy ion beam transport through the insulator beam guide by a particle-in-cell (PIC) simulation code. We also analyze two-stream and filamentation instabilities [19] of HIB, propagating in a background reactor gas.

The results obtained in this study present that the HIB space charge is neutralized well by using the insulator guide settled at the final transport just before a fusion reactor. After the neutralized HIB enters a reactor gas, the electrons co-moving with the focusing HIB are gradually scattered by collisions by reactor gas electrons. However the HIB space charge is still well neutralized by reactor gas electrons. Without the neutralization mechanism at the final transport part just before the reactor, the HIB final fine focus onto a fuel pellet can not be realized. In addition, HIB instability estimations in a reactor gas plasma show that HIB can propagate without serious influences of the instabilities.

2.2 Physical mechanism of insulator guide and simulation model

In a HIB ICF reactor system a HIB accelerator and final focusing elements should stand away from a reactor vessel in order not to be damaged by neutrons and fusion debris. Therefore the HIB space charge should be effectively neutralized after the final focusing element in an accelerator for a fine focus on a fuel pellet. In order to neutralize the focusing HIB space charge and current, we proposed a HIB transport system through an annular insulator beam guide. The physical mechanism of the insulator beam guide is as follows: a HIB creates a local electric field on an inner surface of the insulator beam guide. The local electric field induces local discharges, and a plasma is produced on the insulator inner surface. Then, electrons are extracted from the plasma generated on the inner surface of the insulator beam guide, because of the HIB net space charge as shown in Fig.2.2. The emitted electrons follow the ion beam, and the beam space charge is effectively neutralized by the emitted electrons. Therefore, the HIB can be transported efficiently and one can realize a fine focus through the insulator beam guide. In this study, we employ a Pb^+ ion beam in order to demonstrate the viability of the proposed insulator beam guide system. Our simulation model is shown in Fig.2.3. We assume that the phenomenon concerned is cylindrically symmetric (see Fig.2.3(a)). The PIC code used is a 2.5-dimensional electromagnetic one. The Pb^+ ion-beam-parameter values are as follows: the maximum current is 5 kA, the particle energy is 8 GeV, the pulse width is 10 nsec and the rise and fall times are 2 nsec (see Fig.2.4). The initial beam radius is 4 cm. The initial mean velocity of a focusing Pb^+ beam is given to focus at Z=210 cm, and the average longitudinal speed of the beam ions injected is determined by the waveform. The beam temperature is 10 eV and the beam ions enter uniformly at the beam entrance, that is, Z=0. The transport area is in vacuum. In our simulation, local plasma is generated on the insulator guide surface, when the magnitude of the electric field exceeds the threshold for the local discharge. The threshold is 1.0×10^7 V/m in this study [20].

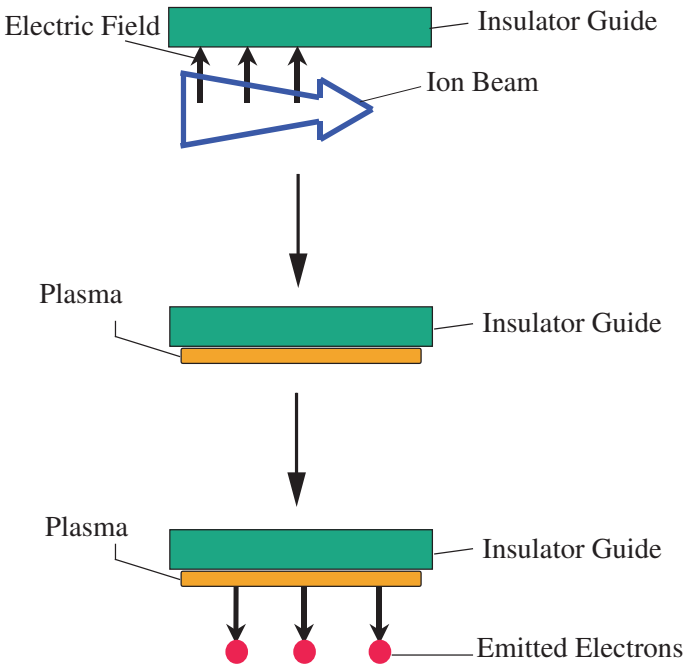

Figure 2.2: Physical mechanism of an insulator guide.

2.3 Simulation results

First, we simulate a Pb^+ ion beam propagation in a vacuum without the insulator beam guide. The particle map of the Pb^+ beam ions is shown in Fig. 2.5. In this case, due to the beam space charge, the beam radius at Z=210 cm (focal point) expands to about 6 mm (see Fig. 2.6). Figure 2.7 presents the particle maps of the beam particles and the electrons emitted from the insulator beam guide for the case with a proposed insulator guide system with the same initial conditions. The electrons extracted from the plasma generated on the insulator inner surface move along with the Pb^+ ion beam. The emitted electrons neutralize the space charge of the beam ions effectively (see Figs. 2.8(a) and (b)), and suppress the radial expansion of the beam. Figure 2.8 shows the history of the total space charge and current of the beam ions and the electrons in the whole transport region. The beam space charge and current are neutralized rather well by the electrons emitted from the insulator beam guide. Figure 2.9 show the beam radius at

(a) cylindrical coordinate

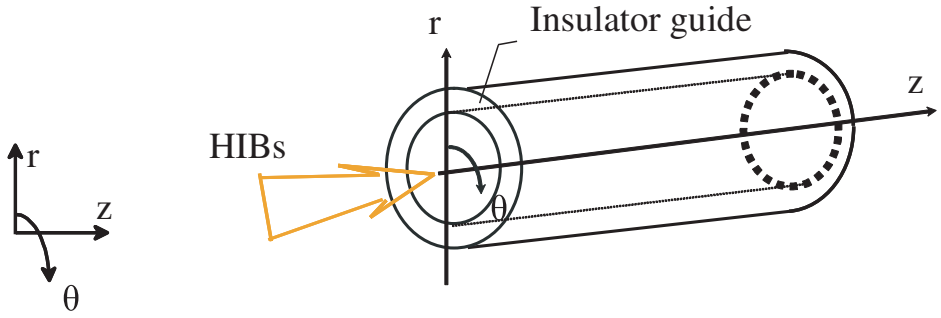

(b) simulation mode

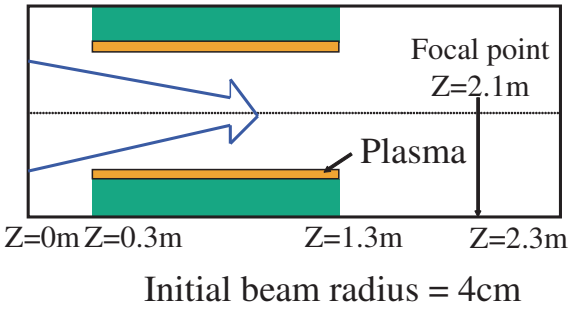

Figure 2.3: (a) Cylindrically symmetric (b) The position of insulator guide, transport distance and focal spot.

Z=200 cm and at Z=210 cm (focal point) in the case of with the insulator beam guide. The final focal radius is about 2 mm in the case with the insulator guide. In Fig. 2.9 we confirm that the focused HIB space charge is neutralized efficiently through an insulator beam guide compared the case without an insulator guide. Therefore the beam is focused well at the focal point, when the insulator beam guide is employed. We also calculate that the HIB average velocities and standard deviations in order to know the focused HIB quality. Table 2.1 shows the beam average velocities, normalized emittance and standard deviations. The normalized emittance values are 8.6×10^{-6} at Z=100 cm and 5.2×10^{-6} at Z=210 cm (focal point) in the case with the guide. On the other hand, the normalized emittance values are 1.5×10^{-5} at Z=100 cm and 1.1×10^{-5} at Z=210 cm (focal point) in the case

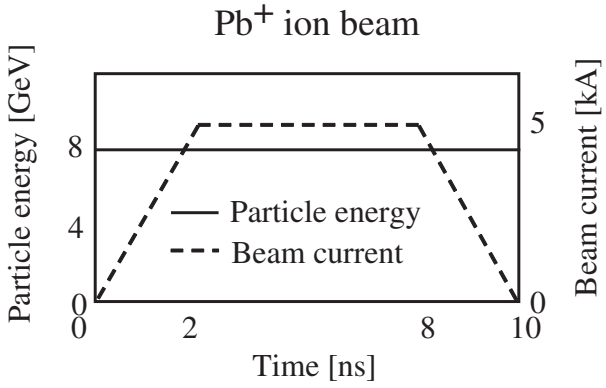

Figure 2.4: HIB pulse, particle energy and maximum current.

without the insulator guide. Therefore we can confirm that the emittance growth is suppressed and that the initial HIB quality is kept well through the insulator guide as shown in Table 2.1. Moreover we can see that the HIB ion temperature in Z direction and r direction for the case with the insulator guide, and the corresponding electron temperature in Z direction and r direction become high as it approaches the focal point as shown in Fig. 2.10.

2.4 Interaction with background gas

First we estimate the energy loss of the co-moving electrons by collisions with the background reactor gas, after the focusing HIB and co-moving electrons enter a HIB ICF reactor gas. The electron-electron collision frequency [21] is given by $\nu = 2.4\times10^{-8}\times N_e \ln\Lambda T_e^{-3/2}$, where N_e is background electrons density, $\ln\Lambda$ is the Coulomb logarithm for collisions between co-moving electrons with HIB and reactor gas electrons, and T_e is background electrons temperature. The collision time of ν^{-1} is about a few nsec, when N_e=3 mTorr and T_e=10 eV. The co-moving electron energy loss by collisions is given by

$$\langle\frac{d\epsilon}{dt}\rangle \simeq -\frac{e^4 ln\Lambda}{4\pi\epsilon_0^2}\frac{N_e}{m_e}\frac{1}{v_{ge}}, \tag{2.1}$$

where $d\epsilon/dt$ is an energy loss by collisions, e is an electron charge, ϵ_0 is permittivity in vacuum, m_e is an electron mass, v_{ge} is a co-moving electron

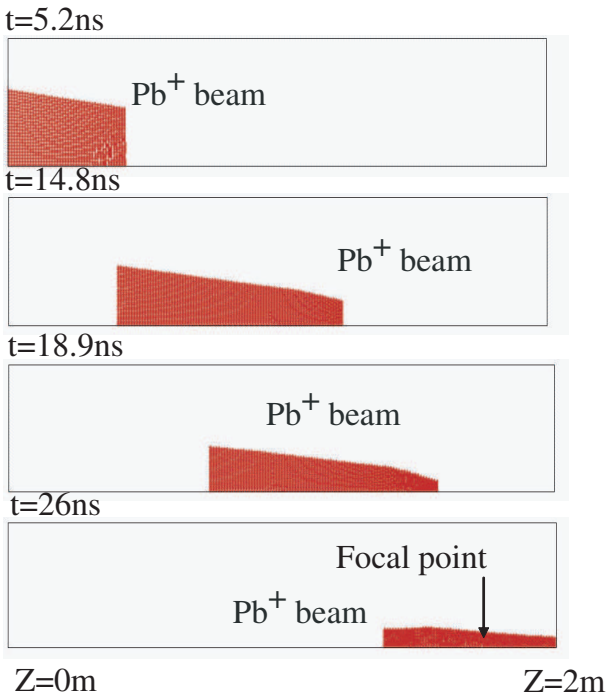

Figure 2.5: HIB particle without the insulator guide.

speed. The co-moving electron energy loss estimated by Eq. (2.1) is a few eV (we change background gas pressure from 0 to 100mTorr). The co-moving initial electron energy is about 22 keV at the entrance to the HIB ICF reactor gas.

Therefore the co-moving electrons is not lose their energy by the collisions between co-moving electrons and background electrons. From this estimation, after the HIB and co-moving electrons enter the HIB ICF reactor gas, the electrons keep on moving with HIBs, and the HIB space charge neutralization is kept.

The HIB also experiences the two-stream and the filamentation instabilities [22–26]. Here we also analyze the two-stream and the filamentation instabilities in a reactor chamber. The maximum growth rate of the two-stream instability between beam ions and background electrons is given by Eq. (2.2).

$$\gamma_{max} = -\frac{\nu}{2} + \sqrt{\frac{\pi}{2}}\frac{\omega_b^2}{\omega_e}\frac{V_b^2}{u_b^2}\exp(-\frac{1}{2}), \tag{2.2}$$

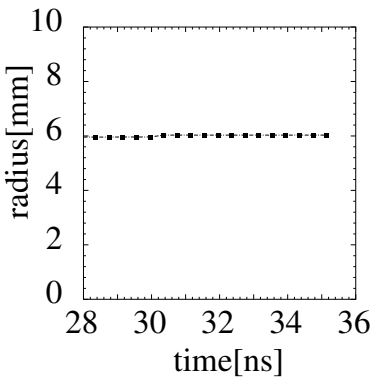

Figure 2.6: HIB radius at the focal spot without guide.

where the collision frequency ν is characterized by the electron-ion collision frequency $\nu = 1.5\times10^{-6}\times N_e \ln\Lambda T_e^{-3/2}$, where $\ln\Lambda$ is the Coulomb logarithm for background electrons-beam ions collision, N_e is the background electron density and T_e is the background electrons temprature. ω_b is the beam ion plasma frequency, ω_e is the background electron plasma frequency, V_b is the beam speed, and ub is the beam thermal speed. The maximum growth rate of the filamentation instability is given by Eq. (2.3).

$$\gamma_{max} = 2\frac{\omega_b^2}{\omega_p^2}\frac{V_b^2}{u_b^2}\nu, \tag{2.3}$$

where V_b is the beam speed and u_b is the beam thermal speed given by $u_b = \sqrt{kT_b/m}$. Here the beam effective temperature T_b is estimated by the inward motion of the focusing beam ions. An outer part of the focusing beam moves inward and overlaps an inner part, so that the beam effective temperature T_b becomes high ($\sim$ MeV).

By Eq. (2.2), we calculate the density range in which the focusing HIB can propagate without severe influences of the two-stream instability ($\gamma\tau < 5$) as shown in Fig. 2.11, where the parameters employed are as follows: the focusing beam temperature T_b=0.3, 0.4, 0.5 MeV, the background plasma temperature T_e=10 eV, the beam drift velocity $V_b = 5.9\times10^8$ cm/s for 8 GeV, the focused beam density $N_b = 1.38\times10^{11} \sim 2.5\times10^{12}$ cm^{-3}, the beam current is I=5.0 kA, and the background plasma density $N_e = 10^{15} \sim 10^{16}$ cm^{-3} (3 $\sim$ 30 mTorr). For the filamentation instability, $\gamma\tau$ estimated by Eq. (2.3) is 0.0040 $\sim$ 0.0005, and therefore we confirm that the HIB is

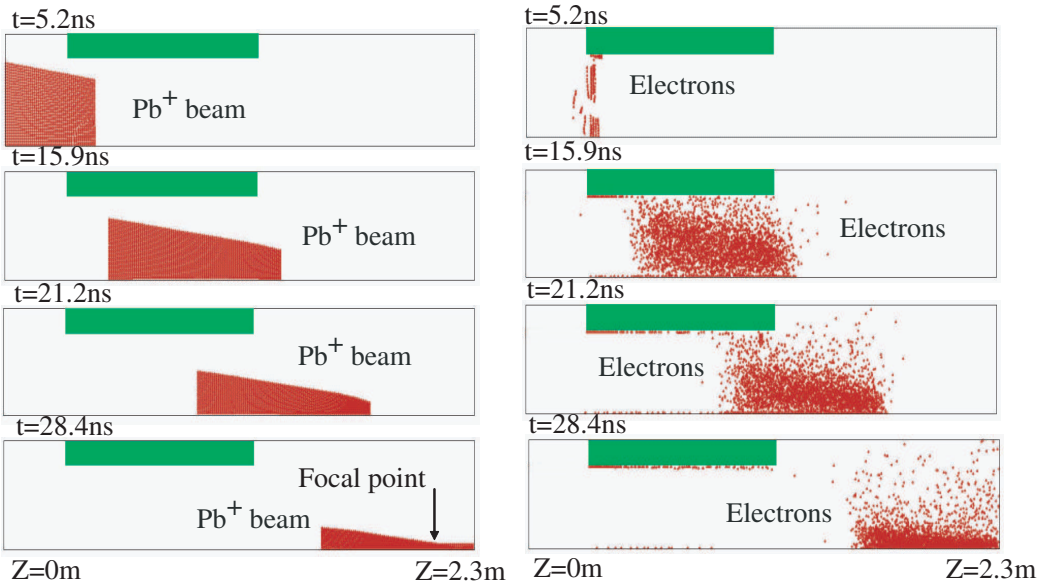

Figure 2.7: HIB particle and emitted electrons maps with insulator guide.

safe from the filamentation instability, and the parameters employed are as follows: the beam temperature T_b=10 keV $\sim$ 1.0 MeV, the background plasma temperature T_e=10 eV, the beam drift velocity $V_b = 5.9 \times 10^8$ cm/s for 8 GeV, the focused beam density $N_b = 1.38 \times 10^{12}$ cm^{-3}, the beam current is I=5.0 kA, and the background plasma density $N_e = 10^{15} \sim 10^{16}$ cm^{-3} (3 $\sim$ 30 mTorr). We expect that the HIB is not influenced seriously by both the instabilities, as long as the background reactor gas electron density is kept low as shown in Fig. 2.11 concerning to the two-stream instability (for example, T_b=0.5 MeV, $N_b = 1.0 \times 10^{12}$ cm^{-3}, $N_e = 6.0 \times 10^{15}$ cm^{-3}). We have also checked that the HIB is safe from instabilities of a mode between HIB ions and reactor gas ions and a mode between co-moving electrons and reactor gas ions.

2.5 Discussions

In this chapter, we proposed the insulator beam guide for the focusing heavy ion beam neutralization. Plasma electrons are emitted from the plasma generated on the insulator inner surface. The electrons move with the heavy ion beam, and the beam space charge is neutralized effectively by the electrons.

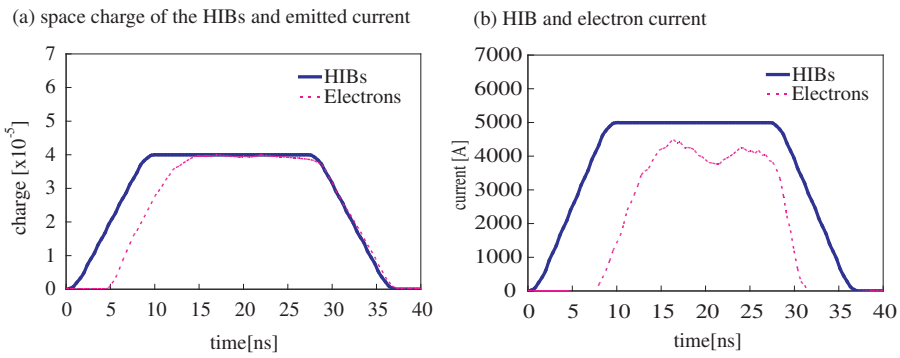

Figure 2.8: (a) The total space charge of the HIBs and emitted electrons and (b) beam ions and electrons current in the whole transport region.

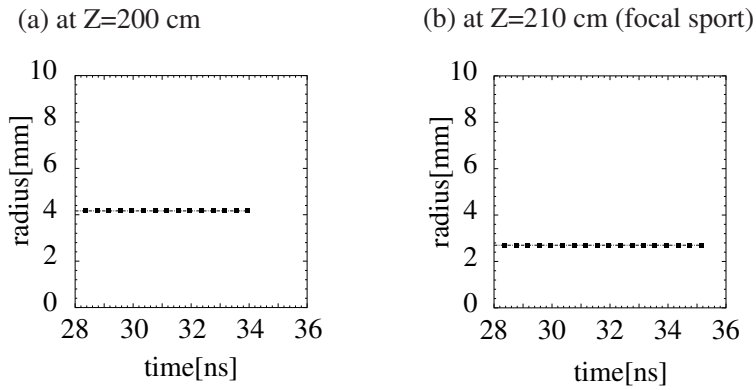

Figure 2.9: Beam radius at Z=200cm and Z=210cm (focal sport) with the insulator guide.

By the PIC simulation, it is confirmed that the heavy ion beam propagates efficiently and is focused well through the insulator beam guide, which may be made of one kind of ceramics and may absorb a part of reactor gas leaked to a beam port. We also confirm that the heavy ion beam is kept in a high quality and an emittance growth is suppressed through the insulator guide. We also presented the HIB stability analyses. Figure 2.11 shows a stability boundary for a focusing HIB propagating without an influence of the two-stream instability. The focusing HIB is also safe from the filamentation instability. Therefore the results shown in this paper presented that the HIB ions are focused successfully onto a fuel pellet located at a reactor center without severe influences of instabilities.

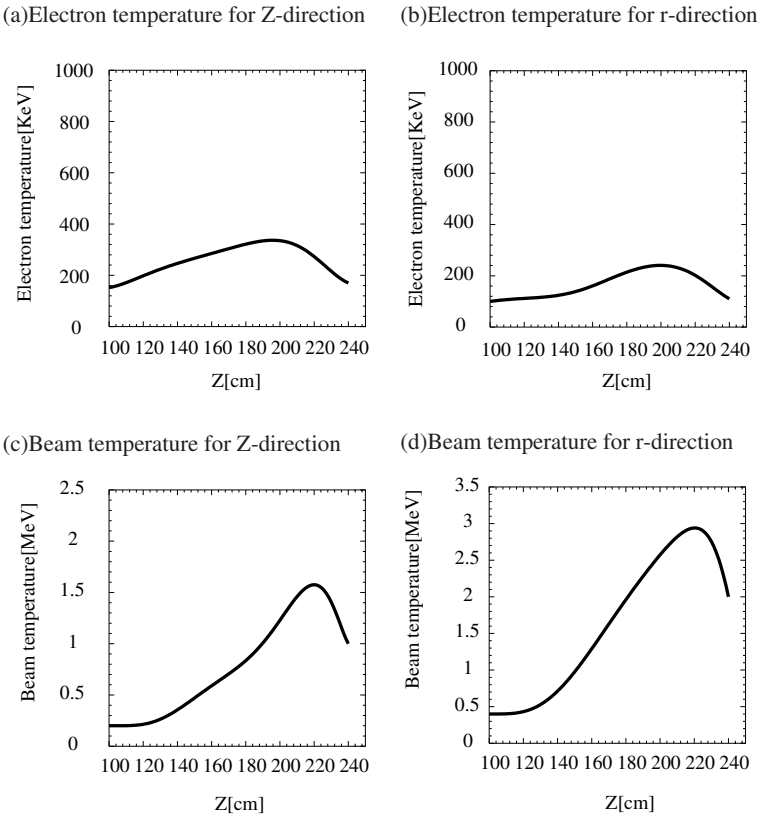

Figure 2.10: The emitted electron temperature for (a) longitudinal and (b) transverse direction, respectively. The HIB temperature for (c) longitudinal and (d) transverse direction, respectively.

Table 2.1: Pb^+ ion beam average velocities and the standard deviations a) with the insulator guide b) without the insulator guide. Here c is a light speed in a vacuum. $\bar{v}$ shows the beam average speed and σ the standard deviations. All value is normalized by light velocity.

a) with the insulator guide

Z [cm]	$\bar{v_z}$	$\bar{v_r}$	$\bar{v_\theta}$
0	2.79×10^{-1}	-2.49×10^{-3}	4.39×10^{-7}
100	2.79×10^{-1}	-2.51×10^{-3}	6.93×10^{-7}
210	2.79×10^{-1}	-1.30×10^{-3}	9.08×10^{-8}
Z [cm]	σ_z	σ_r	σ_θ
0	2.97×10^{-3}	1.43×10^{-3}	2.00×10^{-5}
100	1.44×10^{-3}	1.44×10^{-3}	1.01×10^{-5}
210	1.46×10^{-3}	2.52×10^{-3}	7.76×10^{-6}

b) without the insulator guide

Z [cm]	$\bar{v_z}$	$\bar{v_r}$	$\bar{v_\theta}$
0	2.79×10^{-1}	-2.49×10^{-3}	2.64×10^{-7}
100	2.79×10^{-1}	-2.48×10^{-3}	7.41×10^{-7}
210	2.79×10^{-1}	-1.98×10^{-3}	3.05×10^{-7}
Z [cm]	σ_z	σ_r	σ_θ
0	5.79×10^{-6}	1.43×10^{-3}	2.16×10^{-5}
100	3.89×10^{-5}	1.45×10^{-3}	6.76×10^{-6}
210	2.31×10^{-4}	1.17×10^{-3}	4.70×10^{-6}

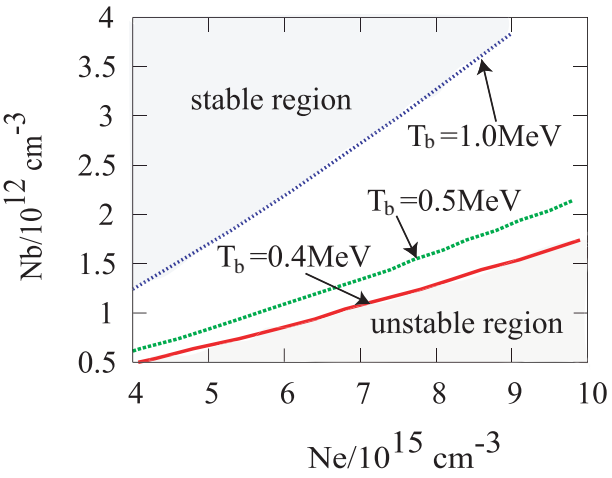

Figure 2.11: Stable region and unstable region for two stream instability.

Chapter 3

HIB-Target Interaction

3.1 Introduction

Key issues in heavy ion beam (HIB) inertial confinement fusion (ICF) include an accelerator design for intense HIBs, efficient HIB transport, a HIB-target interaction, a reactor design and so on [3–5, 27–32]. In this study, we focus on a HIB-target interaction in ICF. In HIB ICF, the beam irradiation non-uniformity on a direct-driven fuel pellet must be suppressed under a few % in order to achieve a symmetric fuel pellet implosion [29, 33–38]. Therefore, a multi-HIB illumination is required to achieve a low beam non-uniformity in the pellet implosion. On the other hand, the total HIB number should be restricted to a realistic number, for example, less than a few hundred beams. Therefore, in this study, we simulate a HIB illumination on the spherical direct-driven target using 12, 20, 32, 60, 92 and 120-beam irradiation systems. In next section we present a detail of beam illumination.

In heavy ion fusion (HIF), the HIB space charge should be neutralized by a plasma [39] or an insulator guide [31] or other methods [32] at the final transport region in order to suppress the beam divergence and the emittance growth; the HIB neutralization methods have been proposed and studied well as described in Chapter 2. After the HIB final transport, the neutralized HIBs illuminate a fuel target. In the fuel pellet implosion the HIB energy deposition non-uniformity should be suppressed to less than a few percent [29, 36–38] in order to realize a stable implosion and to obtain a high ρR of the compressed fuel core; the requirement for the implosion uniformity has been also well studied, and analyses of instabilities, including the Rayleigh-

Taylor instability have been performed intensively in the indirect-driven and the direct-driven implosion schemes. Each implosion scheme has merits and demerits [3, 4, 11, 29, 36]: the indirect-driven scheme may be robust against the beam non-uniformity, though its structure may be complicate and may be expensive relatively. The direct-driven pellet structure may be simple, though the scheme may be sensitive to the HIB illumination non-uniformity.

In HIF researches a study of a realistic HIBs illumination non-uniformity remains between the final HIB transport and the fuel pellet implosion studies, and is at present essentially important for progress in HIF studies. Therefore, in this study, we perform three-dimensional analyses of the HIB illumination non-uniformity in HIB ICF in order to know the detail information of energy non-uniformity on a spherical fuel target.

The HIB illuminates the spherical target and deposits its energy on the target. We calculate the deposition energy on the spherical target according to a stopping power [40–46]. We also show the detail of stopping power in next section. A three-dimensional computer code is developed for the simulation of a HIB irradiation onto a spherical fuel pellet in direct-driven heavy ion fusion. The main object of this section is to clarify a dependence of multi-HIB illumination non-uniformity on parameter values of HIB illumination in HIF. The HIB ions impinge the target surface, penetrate relatively deep into the deposition layer and deposit their energy in a rather wide region in the deposition layer: this HIB deposition feature influences the beam illumination non-uniformity. The HIB temperature and emittance effects are also evaluated. During the HIB illumination the temperature of the energy deposition layer increases to a few hundred eV. We also investigate the pellet temperature effect on the HIB illumination non-uniformity. We also investigate the relationship between a chamber radius and the HIB illumination non-uniformity, and study the effect of the total HIB number on the HIB illumination non-uniformity.

In an ICF power plant, a position of fuel pellet may shift from a reactor center, because a pellet may be injected from a pellet injection port at a reactor wall. The HIB illumination non-uniformity may be influenced by a little pellet displacement from the chamber center. In this section we also investigate the relation between the pellet displacement and the HIB illumination non-uniformity. For the evaluations of the illumination non-uniformity on the target, we compute the root mean square (RMS) and the peak to valley (PTV) non-uniformities on the target [47]. In addition, we also perform mode analyses of the HIB deposition energy on the spherical fuel

target using the Legendre polynomial and the Fast Fourier Transfer (FFT).

The simulation results present that the HIB deposition energy RMS non-uniformity on the target is suppressed to a low value: for example, less than 2.0 % even by a 32-beam system.

3.2 Simulation model

HIBs may be one of promising energy-driver candidates in ICF. In this study, we use a lead (Pb^+) beam as a HIB in ICF. The beam parameters are as follows: the mean particle energy is 8.0 GeV, and the maximal initial beam density is 1.3×10^{11} cm^{-3}. The HIB radius is 3.3 mm. The chamber radius varies from 2.0 m to 8.0 m in our study. In this study, we select two types of beam: the semi-Gaussian distribution of a flat constant density in transverse with the Maxwell-distributed particle energy (with 100 MeV beam longitudinal temperature) and the transverse number density in the Gauss distribution with the Maxwell-distributed particle energy (with 100 MeV beam longitudinal temperature). The Gaussian distribution is shown in Eq. (3.1).

$$n(r) = \frac{1}{\sqrt{2\pi\sigma^2}} \exp\Big(-\frac{r^2}{2\sigma^2}\Big). \tag{3.1}$$

Here, n_{rb} is a number density as a function of beam radius rb. The $\sigma$is standard deviation.

3.2.1 Stopping power

The HIB energy deposition comes mainly from the Coulomb collisions between bound/free electrons and beam ions. Moreover the Coulomb collisions between beam ions and target ions, nucleus scattering and the plasma wave excitation contribute the stopping power. We employ the widely-used expression of the HIB particle effective charge in Refs. [43–45] and calculate the effective charge of the HIB particles traveling through the target. The stopping power in the target is considered to be the sum of the energy deposited in a target nuclei, target bound, free electrons, and target ions [42]:

$E_{stop} = E_{nuc}+E_{free}+E_{ion}+E_{bound}$,where E_{stop} is the deposition energy in the target, E_{nuc} is the deposition energy by the nucleus scattering, E_{free} is by the free electron, and E_{ion} is by the target ion. The nucleus stopping power E_{nuc} becomes effective at the end of the stopping range and describes the elastic the Coulomb collisions between the projectile ions and target nuclei [48]. When a temperature of the target rises and the target is ionized, free electrons contribute the stopping power, through the Coulomb collisions and the plasma collective wave excitations. The free electron stopping power E_{free} is calculated by the Coulomb collision between projectile ions and the target free electrons [44, 45]. E_{ion} is evaluated by the Coulomb collisions between HIB particles and target ions. The Linhard and the Bethe-Bloch equations describe the bound electron stopping power E_{bound}. We use the Bethe equation to calculate the bound electron stopping power at the high beam energy region in this study [43]. In a middle beam energy region, we calculate the bound stopping power from the Bethe equation with the shell correction. At low beam energies, the stopping power theory is mostly evaluated using the Thomas-Fermi model of the atom. Therefore, we use the LSS equation at the low beam energy domain to calculate the bound electron stopping power.

3.2.2 Beam illumination scheme

In this chapter, we simulate a multi-HIB illumination on the spherical target using 12, 20, 32, 60, 92 and 120-beam irradiation systems. In HIF, the HIB space charge must be neutralized in order to overcome the beam divergence due to the self space charge as described in Chapter 2. Viable methods of HIB space charge neutralization have been already proposed and studied intensively at the final HIB transport. Therefore, we assume that HIBs are neutralized perfectly in this study based on these recent research progresses. Each beam position is decided as follows: in the 12-beam system each beam center coincides with the center of each face at the regular dodecahedron. In the same way the 20-beam system is based on the regular icosahedron. We employ the 32-beam system shown by Skupsky [35]. The 60-beam system is vertices of a soccer ball or fullerene [33, 34]. The 92-beam system is combination of 12, 20, and 60-beam systems. The 120-beam system is the combination of two 60-beam systems, each of which is shifted by 90 degree in the vertex direction.

3.2.3 Beam particle orbit in the target

In my study I select two types of target: one is an Al mono-layer pellet structure with the 4-mm external radius as shown in Fig. 3.1 (a), and another one is a Pb+Al pellet structure with the same external radius as shown in Fig. 3.1(b). In the latter pellet structure, the outer Pb layer thickness and mass density are 0.03 mm and 11.3 g/cm^3, respectively. The Al layer thickness and mass density are 0.97 mm and 2.69 g/cm^3, respectively. We employ the target temperature 1, 100, 200, 300, 400 eV in this study.

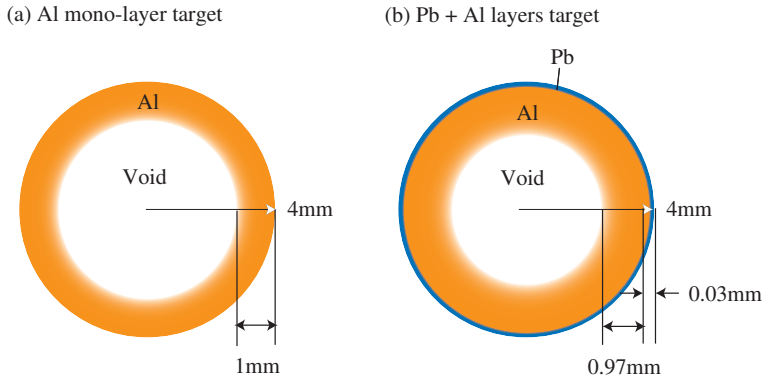

Figure 3.1: (a) Al mono-layer pellet structure with the 4-mm external radius and (b) Pb+Al pellet structure with the same external radius and the Pb layer thickness and mass density are 0.03 mm and 11.3 g/cm^3, respectively. The Al layer thickness and mass density are 0.97 mm and 2.69 g/cm^3, respectively.

In order to calculate the beam particle orbit we define the beam position at the tangential target surface (R, Θ, Φ) and the focal position (f, Θ_f, Φ_f) as shown in Fig. 3.2. Then we can calculate the beam particle orbit in the target (r, θ, ϕ) by the following Eq. 3.2 using the target radius r.

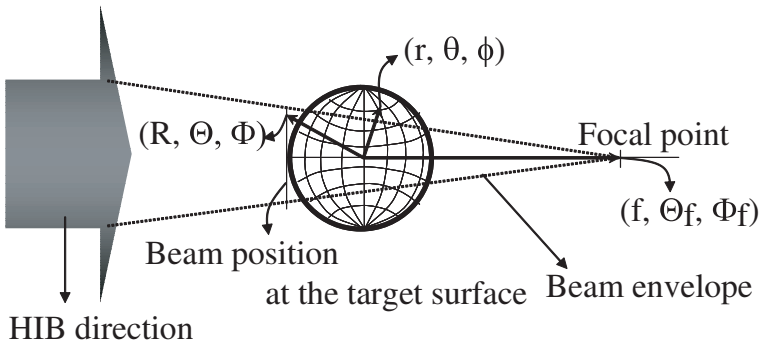

Figure 3.2: Beam focal spot and the target. $(R,\ \Theta,\ \Phi)$ means the beam position at the tangential target surface, $(f,\ \Theta_f,\ \Phi_f)$ is the focal position and $(r,\ \theta,\ \phi)$ is the beam particle orbit in the target.

$$\begin{aligned}
&\frac{r\sin\theta\cos\phi - R\sin\Theta\cos\Phi}{f\sin\Theta_f\cos\Phi_f - R\sin\Theta\cos\Phi} \\
&= \frac{r\sin\theta\sin\phi - R\sin\Theta\sin\Phi}{f\sin\Theta_f\sin\Phi_f - R\sin\Theta\sin\Phi} \\
&= \frac{r\cos\theta - R\cos\Theta}{f\cos\Theta_f - R\cos\Theta}.
\end{aligned} \tag{3.2}$$

From Eq. (3.2), we calculate the beam orbit, i.e. $(r,\ \theta,\ \phi)$ by the known values of the beam position $(R,\ \Theta,\ \Phi)$, the focal position $(f,\ \Theta_f,\ \Phi_f)$ and the value of target radius r.

3.2.4 Beam divergence

The beam particle may slightly diverge by a finite emittance in the transverse direction. Therefore, we include a beam emittance effect and change the beam radius not to miss the target so that all ions hit the target surface. In Fig. 3.4, we define a relation between a beam transverse emittance and a divergence angle α_{dvr}. R_{en} is the beam radius at the fusion reactor wall, R_{ch} is the reactor radius, f is the focal length between the beam focal position and the target center, R_f is the focal spot radius, R_p is the pellet radius, and R_{beam} is the beam radius at the target surface. The beam divergence angle

α_{dvr} is defined as follows:

$$\alpha_{dvr} = \frac{\epsilon_r}{R_{en}}. \tag{3.3}$$

Here, ϵ_r is a beam transverse emittance.

$$R_f = (R_{ch} + f)\tan(\alpha_{dvr}). \tag{3.4}$$

In this study, we calculate a beam divergence angle from the beam transverse emittance ϵ_r. We change the beam transverse emittance from 2.0 mm mrad to 10 mm mrad in this study in order to know the emittance influence. From Eq. (3.3), the beam divergence angle α_{dvr} is calculated to be about 8.2×10^{-3} degree in the case of ϵ_r = 5.0 mm mrad and R_{en}=35 mm. In my study the relation between the focal length f and the beam radius R_{beam} is defined by

$$f = \frac{R_{beam}R_{ch} - R_pR_{en}}{R_{en} - R_{beam}}. \tag{3.5}$$

In addition, the beam focal position moves backward and forward by the beam divergence angle as shown in Fig. 3.4. Therefore, we use Eqs. (3.3) and (3.5) in order to calculate backward and forward focal positions:

$$f_{min} = R_{en}\tan\Big(\xi - 0.07145\alpha_{dvr}\Big) - R_{ch}, \tag{3.6}$$

$$f_{max} = R_{en}\tan\Big(\xi + 0.07145\alpha_{dvr}\Big) - R_{ch}. \tag{3.7}$$

Here, f_{min} is the backward focal position of beam focal spot, f_{max} is the forward focal position (see Fig. 3.4), and ξ is given by $\xi = \arctan[(R_{ch}+f)/R_{en}]$. Based on Eqs. (3.6) and (3.7), the beam radius at the fuel pellet surface changes between 2.7 mm and 3.8 mm in the case of 5.0 mm mrad emittance, so that any HIB ions do not miss impinging the pellet surface.

3.2.5 Deposition energy calculation procedure

In my study, we divide one HIB into 316 beam-lets in order to simulate a precise HIB illumination non-uniformity as shown in Fig. 3.4(a). Each beam-let

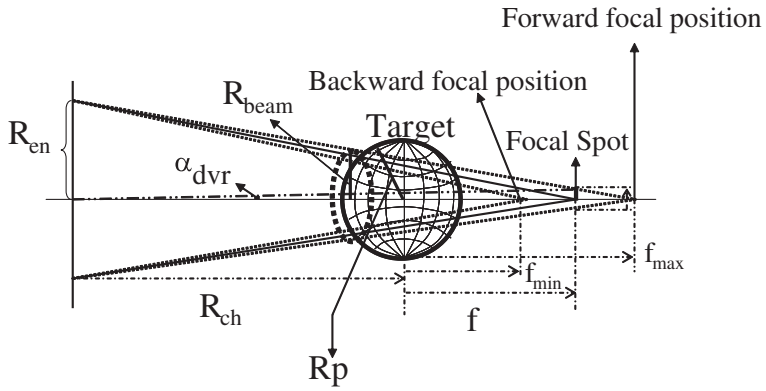

Figure 3.3: The relationship between a beam emittance and divergence angle at the beam port. R_{en} is the chamber radius in fusion reactor, R_{ch} is the reactor radius, f is the beam focal spot, R_f is the focal spot radius, R_p is the pellet radius, $\alpha_{dvr}$is the beam divergence angle, and R_{beam} is the beam radius in front of target.

deposits its energy on space meshes of the spherical target as shown in Fig. 3.4(b). Then in order to calculate the deposition energy of one HIB in one mesh, we use Eq. (3.8).

$$E_{stop} = \frac{dE}{dl} V n^{\frac{2}{3}}. \tag{3.8}$$

Here, dE/dl is the stopping power, that is, a beam-let deposition energy per unit length, n is the beam particle number density, and V is the volume of one cell in the target.

The deposition energy is distributed to the mesh points. Each beam-let has an effective area, and the deposition energy is distributed to the meshes by the beam-let effective area as shown in Fig. 3.4(b). When multi-HIBs illuminate the spherical target and deposit their energy on the target, the deposition energy is calculated by Eq. (3.9).

$$E_{ijk} = \sum_{N} E_{stop}. \tag{3.9}$$

Here, E_{ijk} is the deposition energy at each mesh point denoted by (i, j, k) in the three-dimensional space and N is the number of HIBs impinging the cell.

3.2.6 Evaluation of non-uniformity on the spherical target

In my study, we evaluate the energy non-uniformity at the target. In ICF, the beam irradiation non-uniformity on the fuel target must be suppressed under a few % in order to achieve a symmetric fuel pellet implosion. In HIB ICF the Bragg peak deposition area plays the most important role for a target implosion. Therefore, we define the total relative root-mean-square (RMS) and peak-to-valley (PTV) non-uniformity as follows:

$$\sigma_{RMS} = \sum_{i}^{n_r} w_i \sigma_{RMS_i}, \tag{3.10}$$

$$\sigma_{RMS_i} = \frac{1}{\langle E \rangle_i} \sqrt{\frac{\sum_{j}^{n_\theta} \sum_{k}^{n_\phi} \Big(\langle E \rangle_i - E_{ijk} \Big)^2}{n_\theta n_\phi}}, \tag{3.11}$$

$$w_i = \frac{E_i}{E}. \tag{3.12}$$

The peak-to-valley (PTV) non-uniformity is defined as follows:

$$\sigma_{PTV} = \sum_{i}^{n_r} w_i \sigma_{PTV_i}, \tag{3.13}$$

$$\sigma_{PTV_i} = \frac{E_i^{max} - E_i^{min}}{2\langle E \rangle_i}. \tag{3.14}$$

Here, σ_{RMS_i} and σ_{PTV_i} are the RMS and PTV non-uniformities on the i-th surface of deposition, respectively. w_i is the weight function in order to include the Bragg peak effect or the deposition profile. n_r, n_θ and n_ϕ are mesh numbers in each direction of the spherical coordinate. $\langle E \rangle_i$ is the mean deposition energy on the i-th surface, E_i is the total deposition energy on the i-th surface, and E is the total deposition energy. E_i^{max} and E_i^{min} are the maximal and minimal deposition energies on the i-th surface, respectively.

We also performed mode analyses on the spherical fuel target by using the spherical harmonic function $Y_n^m(\theta, \phi)$

$$s_n^m = \frac{1}{4\pi}\int_0^{\pi}\sin\theta d\theta\int_0^{2\pi}E(\theta,\phi)Y_n^m(\theta,\phi)d\phi. \quad (3.15)$$

Here, s_n^m is an amplitude of energy spectrum, n and m are the mode numbers, θ and ϕ are azimuthal and vertex angles, respectively. $E(\theta,\phi)$ is the deposition energy from the beam particles at each mesh point. By using the Legendre polynomial function $P_n^m(\cos\theta)$, the spherical harmonic function is described as follows:

$$Y_n^m = P_n^m(\cos\theta)e^{im\phi}. \quad (3.16)$$

Therefore, the spectrum of the deposition energy on a spherical target is

$$s_n^m = \frac{1}{4\pi}\int_{-1}^{1}d(\cos\theta)\int_0^{2\pi}E(\theta,\phi)P_n^m(\cos\theta)e^{-im\phi}d\phi. \quad (3.17)$$

In order to compute the energy spectrum s_n^m on a computer, Eq. (3.17) is modified by using the Gauss-Legendre integration and FFT as follows:

$$s_n^m = \frac{1}{2}\sum_{j=1}^{J}g_jF^m(\theta_j)P_n(\cos\theta_j), \quad (3.18)$$

where

$$F^m(\theta_j) = \frac{1}{K}\sum_{k=0}^{K-1}E(\theta_j,\phi_k)e^{-im\phi_k}. \quad (3.19)$$

Here, g_j is the Gaussian weight corresponding to the zero points, and J is the number of zero points. In our study, the Gaussian weight is given by Eq. (3.20).

$$g_j = \frac{2}{(1-\cos^2\theta_j)\{P_n'(\cos\theta_j)\}^2}. \quad (3.20)$$

Here, $P'_N(\cos\theta_j)$ is the Legendre polynomial differential coefficient. K is a mesh number in the vertex direction. In order to include the Bragg peak effect we calculate the spectrum of the deposition energy at the Bragg peak layer and we also calculate the global energy-spectrum using the weight function w_i. The summation of the energy spectrum amplitude is normalized to be 1.0 in our study.

3.3 Simulation results

3.3.1 Deposition non-uniformity

Figure 3.5(a) shows the deposition energy of beam particles at each surface without the beam temperature effect for Al layer target with the chamber radius of 5 m, 120-beam system, and the semi-Gaussian distribution. In Fig. 3.5(a), we can see the Bragg peak at the middle layer of the energy absorption region, and the RMS and PTV non-uniformities are low at the Bragg peak layer. At the end of the beam particle stopping region, the deposition energy is much small compared with the Bragg-peak-layerfs one. In actual the pressure peak generated by the HIBs deposition at the Bragg peak region drives the inner fuel to the implosion with a high speed (typically $\sim 3 \times 10^7$cm/s). Based on this reason and on results of the implosion studies previously performed [29, 31, 36, 44, 45], it is known that the HIBs deposition energy in the Bragg peak region contributes mainly to the implosion. Therefore, in this study, we calculated total RMS non-uniformity using the weight function wi in order to include the Bragg peak effect. The RMS non-uniformity is evaluated by Eq. (3.10), and the result is 4.44 %. Figure 3.5(b) shows the energy deposition in the case of 120-beam system, 5 m chamber radius, the semi-Gaussian distribution and the Al target including the longitudinal beam temperature of 100MeV and the transverse beam radial emittance of 5.0 mm mrad. In Fig. 3.5 we can see that the Bragg peak moves slightly outward in the radial direction and the RMS non-uniformity becomes 1.52 %. The HIB illumination non-uniformity in the realistic case including the beam temperature or the beam divergence becomes small compared with that in the case with the zero-temperature HIB. This result presents that the HIB illumination non-uniformity can be smoothed and suppressed due to the beam temperature or the transverse emittance.

We also calculate the deposition-energy spectra at the Bragg peak layer

for the zero-temperature beam (r=3.73 mm) and for the case with the beam temperature of 100 MeV (r=3.83 mm) as shown in Figs. 3.6(a) and (b). Figures 3.6(c) and (d) are the global non-uniformity spectra using the weight wi for the zero-temperature beam and for the case with the beam temperature of 100 MeV. In Fig. 3.6, (n, m) and s_n^m are the mode numbers and the amplitude of spectrum, respectively. If the deposition energy is distributed in complete spherically symmetric, the amplitude of spectrum is set to 1.0 in the mode (n, m)=(0, 0) in our study. In order to achieve a symmetric energy deposition in the direct-drive HIB ICF, the most spectrums should be concentrated on the mode (n, m)=(0, 0), and the amplitude of the mode (n, m)=(0, 0) has a large value near 1.0 in our simulation results, compared with those for other modes. For this reason, in this study, we focus on the amplitudes of spectrum modes except the mode (n, m)=(0, 0). Therefore our calculation results shown in spectrum figures present the spectrum without the mode of (n, m)=(0, 0). In Fig. 6 the amplitude of the spectra in the case of the Bragg peak layer is small compared with that for the global non-uniformity. This result means that the deposition energy at the Bragg peak layer is more uniform compared with the deposition energies at other layers. This is also confirmed by the results in Fig. 3.5. In HIB ICF the Bragg peak area plays an important role for the symmetric target implosion. Therefore, we expect that we may realize an effective compression of target and efficient target implosion. We also confirm that the amplitude in the case including the beam temperature becomes small compared with that in the case of the zero beam temperature, as expected by the results presented above. Moreover in Figs. 3.6(a) and (b) the amplitude of the deposition-energy spectrum at the mode (n, m)=(0, 0) is 0.97 in the case with the zero beam temperature, and the amplitude of the energy spectrum at the mode (n, m)=(0, 0) is 0.99 in the case including the beam temperature.

Figures 3.7 show the energy deposition in the target in the case of Pb+Al layers target structure (a) without the beam temperature (semi-Gaussian) and (b) with the beam temperature of 100MeV and the transverse beam emittance of 5.0 mm mrad. The number of HIBs is 120, the chamber radius is 5 m and particle number density is in the semi-Gaussian distribution in the both cases. The HIB energy is deposited in the Al energy-absorber layer as well as the Pb layer. However the energy deposited in the Al pusher/energy-absorption layer in our study is used effectively for the fuel implosion [29]. The Pb layer behaves as a tamper. In this type of the HIF pellet the thickness of the Al pusher layer is designed to be sufficiently thick so that a pertur-

bation of the Pb tamper layer can not reach the fuel during the HIB pulse duration and at the same time HIB particles do not reach the fuel in order to prevent a fuel pre-heating. Therefore, the HIB energy deposition non-uniformity is evaluated only in the Al layer in this study. In these cases, the RMS non-uniformity is 1.72 % for the case including the beam temperature of 100MeV, and 5.25 % for the case with the zero beam temperature.

We also calculate the spectra as shown in Figs. 3.8: (a) in the case with the zero beam temperature at the Bragg peak layer (r=3.79 mm), (b) with the 100 MeV beam temperature at the Bragg peak layer (r=3.87 mm), (c) the global non-uniformity in the case with the zero temperature beam, and (d) the global non-uniformity with the 100 MeV beam temperature. In Fig. 3.8, the amplitude of the energy spectra at the Bragg peak layer is small compared with that for the global non-uniformity. We also confirm that the amplitude in the case with the beam temperature of 100MeV and the 5.0 mm mrad transverse emittance is small compared with that in the case with the zero beam temperature. From these results, we found that the Pb tamper effect is minor. The energy spectrum value is 0.99 at the mode (n, m)=(0, 0) in the case including the beam temperature, and 0.96 at the mode (n, m)=(0, 0) in the case with the zero beam temperature. The RMS non-uniformity in the case of Pb+Al target is 1.72 %, and this result also shows a good result for a symmetric energy deposition.

3.3.2 Chamber radius effect

Figure 3.9 shows a relationship between the HIB-ICF reactor chamber radius Rch and the HIB illumination non-uniformity for the Al layer target with the beam temperature and the semi-Gaussian distribution in the cases of 32, 60 and 120-beam systems. In this case we fix the beam transverse emittance to 5.0 mm mrad and vary the focal spot radius R_f and distance f. The RMS non-uniformity changes gradually along with the change in the reactor chamber radius. In recent ICF designs, the chamber radius of fusion power plant is about $4.0 \sim 6.0$ m [28, 30]. In our results the optimal non-uniformity stays at around the $3.0 \sim 6.0$ m chamber radius in the 32, 60 and 120-beam systems for the fixed emittance of 5.0 π mm-mrad. These results present that the RMS non-uniformity is kept low enough even in the 32-beam system in the cases with a realistic ICF reactor chamber radius. We also perform another parameter study to demonstrate a requirement for the emittance in order to realize the low non-uniformity when the chamber radius varies. In

this study we fix R_p =4 mm and R_f =0.66 mm and change the chamber radius R_{ch}. By Eqs. (3.3) and (3.4) the emittance is computed as shown in Fig. 3.10. In this parameter study the non-uniformity is kept small (see σ_{RMS} in Fig. 3.10), though the requirement for the emittance becomes severe with the increase in the chamber radius R_{ch}. These results present that HIB accelerator should deliver HIBs with a low beam transverse emittance and that we should select the chamber radius.

3.3.3 The Gaussian beam

We use the Gaussian distribution in order to simulate more realistic case compared with the semi-Gaussian distribution as the beam particle transverse number density distribution. We optimize the standard deviation σ for any beam systems in order to suppress the beam irradiation non-uniformity. Figure 3.11 shows the Gaussian distributions with the various standard deviations σ selected as follows: σ=1.20R_{beam} (we call this type G1 in this thesis), σ=1.00R_{beam} (G2), σ=0.80R_{beam} (G3), σ=0.55R_{beam} (G4), and σ=0.50R_{beam} (G5). Figure 3.12 shows a relation between the RMS non-uniformity, the Gaussian types, and the beam numbers for the various σ in the case of Al layer target with the chamber radius of 5 m including the longitudinal beam temperature of 100 MeV and the transverse beam radial emittance of 5.0 π mm mrad. In Fig. 3.12 we confirm that the non-uniformities are suppressed low in the cases of G1-G3 for the lager number of beams ($\geq$ 32). This result shows that the sharp Gaussian distribution should be avoided.

3.3.4 Beam number effect

Figure 3.13 shows the RMS non-uniformity versus the HIB total number in the cases of (a) Al and (b) Pb+Al layer target with the chamber radius of 5 m. The marked diamonds, triangles, squares, and crosses mean the results in the cases of the Gaussian distribution (G2) with and without the temperature effect and of the semi-Gaussian distribution with and without the temperature effect, respectively. Particularly, in the case with the Gaussian distribution with the beam temperature of 100 MeV marked by diamonds in Fig. 3.13, the RMS non-uniformity in the case of 120-beam system is 1.49 % for Al structure and 1.60 % for Pb+Al structure. These values are close to the values in the semi-Gaussian distribution with the beam temperature: 1.52 % for Al structure and 1.72 % for Pb+Al structure in the case of 120-

beam system for the semi-Gaussian with the beam temperature. Therefore our calculation results also demonstrate that the realistic Gaussian beam is good for HIB ICF in order to achieve a symmetric implosion.

3.3.5 Target temperature effect

The target temperature increases in HIB ICF, when HIBs impinge on a fuel pellet. When the target temperature increases, the beam particle stopping range changes with a target temperature [41, 49]. When the stopping range changes, the non-uniformity of deposition energy at the target may change. Therefore, we should investigate the relationship between the deposition energy non-uniformity and the target temperature. From Fig. 3.14(a) we can confirm that the beam particle stopping range changes with a target temperature change. Figure 3.14(b) shows the target temperature versus the RMS non-uniformity. We use the Al layer target and the semi-Gaussian beam including the longitudinal beam temperature of 100 MeV and the transverse beam radial emittance of 5.0 mm mrad in the cases of 32, 60, and 120-beam systems. When the target temperature increases, the RMS non-uniformity does not change much in the target temperature range expected in HIB ICF. This result demonstrates that the HIB illumination non-uniformity is kept low during the HIB pulse duration, once the HIB illumination pattern is selected for the cold target.

3.3.6 Displacement of fuel pellet position in a reactor

In the above subsections, all calculations were performed with the assumption that a pellet is set just to the chamber center. Such the requirement is difficult to be realized in practice [11, 12, 50] Therefore, a little pellet displacement from the reactor chamber center is evaluated in this subsection. We assume that the pellet is injected into the chamber vertically, and simulate the effect of a little displacement dz as shown in Fig. 3.15(a). Our illumination pattern is a basically spherically symmetric pattern. So the vertical displacement of dz may be sufficiently general for our present purpose. The results for the HIB irradiation systems investigated are plotted in Fig. 3.15 in the cases of the Al layer target, the Gaussian beam (G2) including the beam temperature with the chamber radius of (b) 2 m and (c) 5 m. In Figs. 3.15(b) and (c) we can confirm that the HIB irradiation non-uniformity is sensitive to the pellet

position displacement in the both cases. This result means that the pellet displacement may be a serious problem in HIB ICF.

Therefore, we suggest the new illumination scheme to suppress the illumination non-uniformity even if the pellet displacement is occur. The new illumination scheme shows in Fig. 3.16. The Fig. 3.17 show the RMS non-uniformity v.s. target displacement from the reactor chamber center in the cases of nomal32-HIBs illumination, using the large HIB radius and large HIB radius + new illumination scheme. From this results, we can confirm that the RMS non-uniformity is kept low using the large HIB radius + new illumination scheme (especially dTheta=2deg). However the HIB energy loss using the large radius is serious problem as Fig. 3.18. This problem must be solved in the future.

3.4 Discussions

In HIF the HIB non-uniformity induces the pressure or acceleration non-uniformity and consequently induces the implosion and ρR non-uniformities. Here we discuss the relation between the HIB non-uniformity and the implosion radial acceleration non-uniformity following Ref. [51]: in [51] Sacks et al. also present an estimation of the HIB irradiation non-uniformity, as well as a discussion on a relation between an implosion non-uniformity and the HIB irradiation non-uniformity and suggest a pressure smoothing effect. First we define the radial acceleration non-uniformity $\delta a/\langle a \rangle$ as a summation of a ratio between the average acceleration $\langle a \rangle_i$ at the ith surface , including the weight fuction w_i [see Eq. 3.12]. The HIB energy deposition non-uniformity consisted of mainly the variation of the HIB deposition position; in our study the former factor is evaluated through δa_i and w_i represents the latter. The pressure in one cell at the deposition layer is estimated by $E_{ijk}/\delta V_{ijk}$. Here δV_{ijk} is the volume of one cell. Therefore we can estimate the radial acceleration a_{ijk} at each mesh point as follows:

$$a_{ijk} \propto \frac{E_{ijk}}{\delta V_{ijk} \cdot \lambda_{ijk}}. \tag{3.21}$$

Here, the λ_{ijk} is the scale length of the pressure gradient at each mesh point. Moreover the mean radial acceleration $\langle a \rangle_i$ at the i-th surface is given by

$$\langle a\rangle_{ijk} \propto \frac{\langle E\rangle_{ijk}}{\langle \delta V\rangle_i \cdot \lambda_i}. \tag{3.22}$$

Here, the $\langle \delta V\rangle_i$ is the mean volume of one cell at the i-th surface and λ_i is the mean scale length of the pressure gradient at the i-th surface.

In our study, we estimate the variation of radial acceleration at the i-th surface using the root-mean-square as follows:

$$\delta a_i \propto \frac{\sqrt{\sum_j \sum_k (\langle a\rangle_i - a_{ijk})^2}}{n_\theta n_\phi}. \tag{3.23}$$

From Eqs. (3.21) - (3.23), we can calculate the radial acceleration non-uniformity as follows:

$$\begin{aligned}
\frac{\delta a}{\langle a\rangle} &= \sum_i w_i \cdot \frac{\delta a_i}{\langle a\rangle_i} \\
&= \sum_i w_i \cdot \frac{\sqrt{\sum_j \sum_k (\frac{\langle E\rangle_i}{\langle \delta V\rangle_i \cdot \lambda_i} - \frac{E_{ijk}}{\delta V_{ijk}\cdot \lambda_{ijk}})^2}/n_\theta n_\phi}{\frac{\langle E\rangle_i}{\langle \delta V\rangle_i \cdot \lambda_i}} \\
&= \sum_i w_i \cdot \sqrt{\sum_j \sum_k (\frac{\frac{\langle E\rangle_i}{\langle \delta V\rangle_i \cdot \lambda_i} - \frac{E_{ijk}}{\delta V_{ijk}\cdot \lambda_{ijk}}}{\frac{\langle E\rangle_i}{\langle \delta V\rangle_i \cdot \lambda_i}})^2 \cdot \frac{1}{n_\theta n_\phi}}.
\end{aligned} \tag{3.24}$$

In an actual fuel target we can usually assume $\delta V_{ijk} \approx \langle \delta V\rangle_i$ and $\lambda_i \approx \lambda_{ijk}$ at each ith surface. Therefore we can rewrite Eq. (3.24) as follows:

$$\frac{\delta a}{\langle a\rangle} \approx \sum_i w_i \cdot \sqrt{\sum_j \sum_k (\frac{\langle E\rangle_i - E_{ijk}}{\langle E\rangle_i})^2 \cdot \frac{1}{n_\theta n_\phi}} = \sigma_{rms}. \tag{3.25}$$

Equation (3.25) shows that the global acceleration non-uniformity can be estimated by the RMS deposition-energy non-uniformity [see Eq. (3.10)]. Therefore, the results presented in this study serve important information in the HIF direct-driven pellet implosion.

In this section, we studied the HIB deposition non-uniformity in a direct-driven HIB-ICF pellet. For various beam parameters and different reactor chamber radii we investigated the energy deposition non-uniformity using 12, 20, 32, 60, 92 and 120-beam irradiation systems. The HIB diverges slightly by the beam temperature. We include the effect of a beam longitudinal temperature and the beam transverse emittance. In our simulation results we confirm that the HIB illumination non-uniformity is 1.52 % in the case of the Al mono-layer structure target, the beam temperature of 100MeV, the 120-beam system, and the semi-Gaussian particle density distribution. In the case of the Pb+Al target structure, 1.72 %. On the other hand, the RMS non-uniformity using the Gaussian beam including the beam temperature is close to the non-uniformity for the semi-Gaussian distribution with the temperature effect (1.49 % for Al layer, 1.60 % for Pb+Al layer). From these results, we expect that the fuel can be successfully imploded and the fusion energy can be released from a direct-driven fuel pellet in HIB ICF using the Gaussian or semi-Gaussian HIBs. Moreover we analyzed the spectrum of the HIB illumination non-uniformity in the spherical target. As a result, the deposition energy non-uniformity in the target includes higher modes with sufficiently low amplitudes. Therefore, the mode analyses also demonstrate that by using an appropriate illumination pattern and the selected HIB illumination parameter values the sufficiently low non-uniformity can be realized. From the relationship between the chamber radius and the HIB illumination non-uniformity in the cases of 32, 60, and 120-beam systems, with the beam temperature and the semi-Gaussian distribution particle number density, the RMS non-uniformity does not change much with the change in the reactor chamber radius as shown in Fig. 3.9 at a realistic chamber radius R_{ch} of about $3 \sim 6$ m. In this parameter range of R_{ch} we can expect that the HIB illumination non-uniformity is suppressed less than a few %. We also demonstrated the important effect of the HIB transverse emittance in Fig. 3.10. The results show that the beam transverse emittance should be sufficiently low and that the reactor chamber radius should be optimized.

In HIB ICF, the target temperature increases during the HIB pulse duration. Therefore, we also calculated the relationship between the target temperature and the HIB illumination non-uniformity. We found that even if the target temperature increases in a typical temperature range in HIB ICF, the RMS non-uniformity does not change much. This result presents that the RMS non-uniformity is kept low during the HIB pulse illumination onto a direct-driven pellet in ICF. Moreover we investigated the non-

uniformity growth due to the little pellet displacement of the pellet position from the chamber center. The calculation results demonstrated that the pellet displacement is a serious problem in HIF. We also estimate the effect of acceleration non-uniformity in radial direction. From this estimation, we expect that the effect of acceleration non-uniformity is not serious problem to archive an effective implosion. In order to investigate a dynamic HIB illumination non-uniformity, hydrodynamic implosion simulations coupled with our 3-D HIB illumination code should be performed, and this work is done in the next chapter.

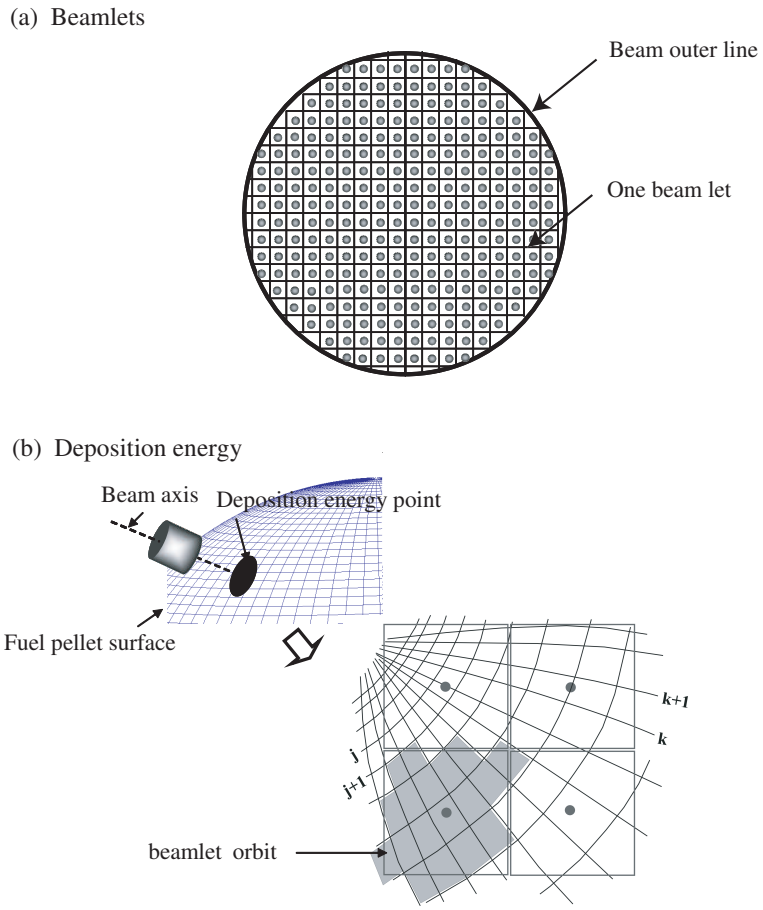

Figure 3.4: (a) Beam-let. Each beam-lets deposit its energy in the spherical target, then the deposition energy is divided each mesh points on the spherical target. (b) Deposition energy at each mesh point. The beam-let have an effective area. The deposition energy at a mesh point is defined from the beam-let effective area.

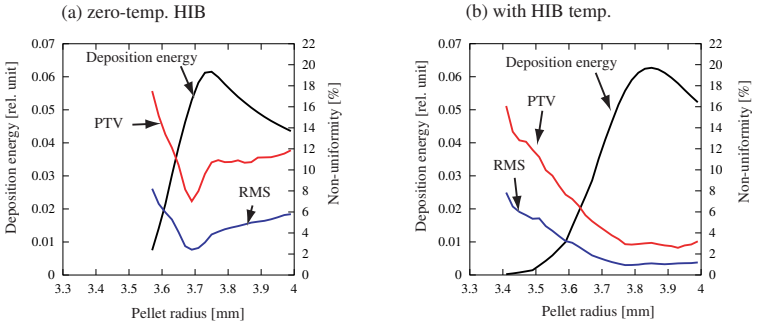

Figure 3.5: The deposition energy of beam particles in the relative unit and non-uniformities at each surface in the cases (a) without the beam temperature effect and (b) with the temperature effect for Al layer target for the chamber radius of 5 m, 120-beam system, and the semi-Gaussian distribution.

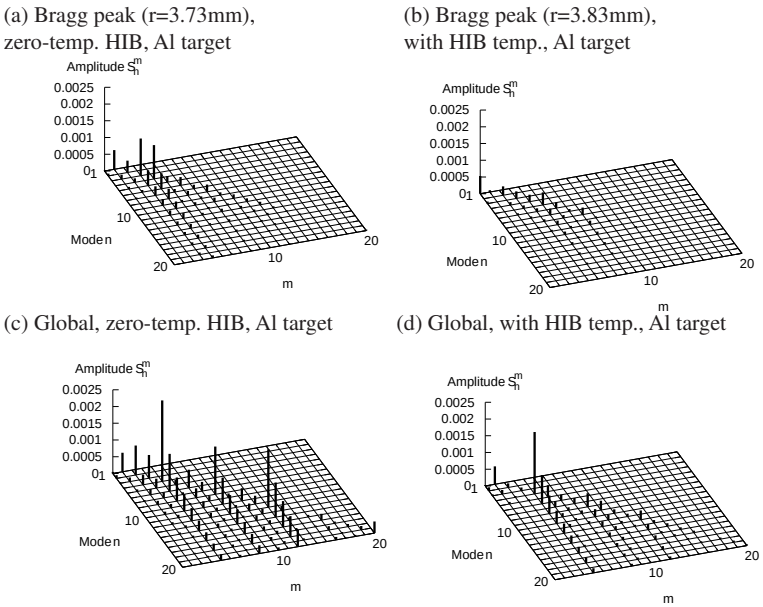

Figure 3.6: The energy spectra at the Bragg peak layer (a) for the zero-temperature beam (r=3.73 mm) and (b) with the beam temperature (r=3.83 mm) for Al layer target. The global non-uniformity spectra using the weight w_i for the (c) zero-temperature beam and (d) with the beam temperature for Al layer target.

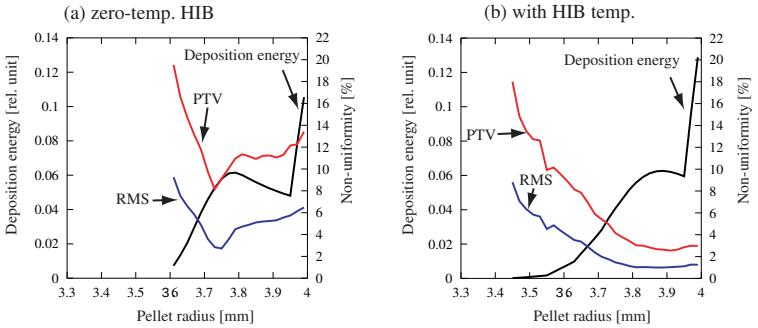

Figure 3.7: The deposition energy of beam particles in the relative unit and non-uniformities at each surface in the cases (a) without the beam temperature effect and (b) with the temperature effect for Pb+Al layer target for the chamber radius of 5 m, 120-beam system, and the semi-Gaussian distribution.

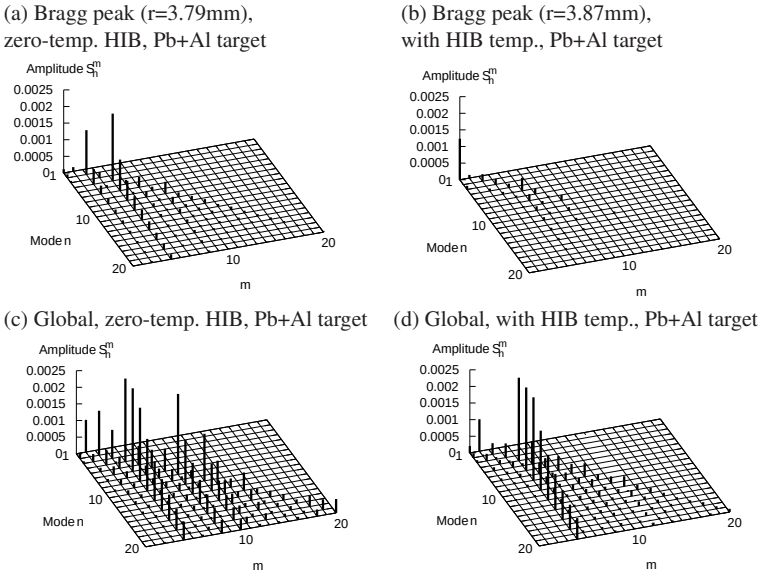

Figure 3.8: The energy spectra at the Bragg peak layer (a) for the zero-temperature beam (r=3.79 mm) and (b) with the beam temperature (r=3.87 mm) for Pb+Al layer target. The global non-uniformity spectra using the weight w_i for the (c) zero-temperature beam and (d) with the beam temperature for Pb+Al layer target.

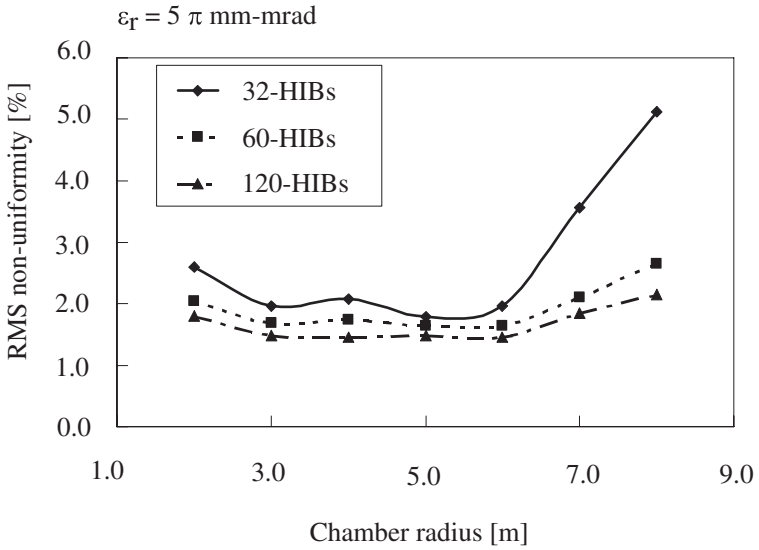

Figure 3.9: The chamber radius versus the RMS non-uniformity in the cases of Al layer target with the semi-Gaussian distribution including the beam temperature for the 32, 60, and 120-beam systems.

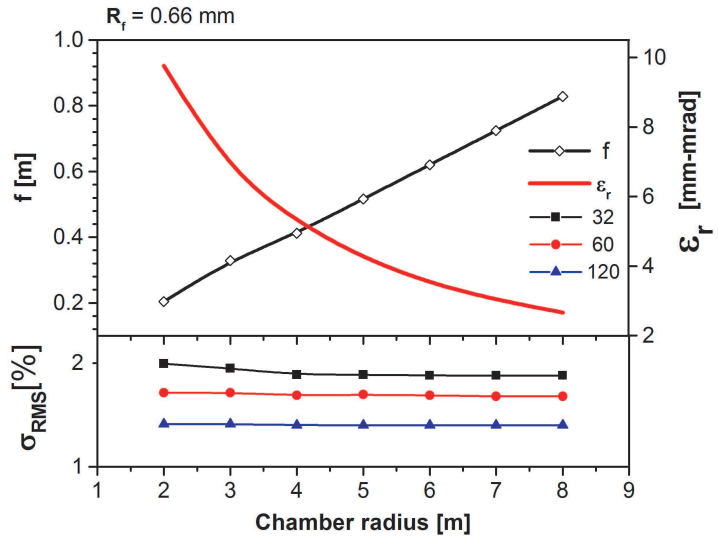

Figure 3.10: The relationship between the beam transverse emittance, focal distance, and the RMS non-uniformity. The beam emittance should decrease and the focal distance f should increase with the increase in the chamber radius R_{ch}.

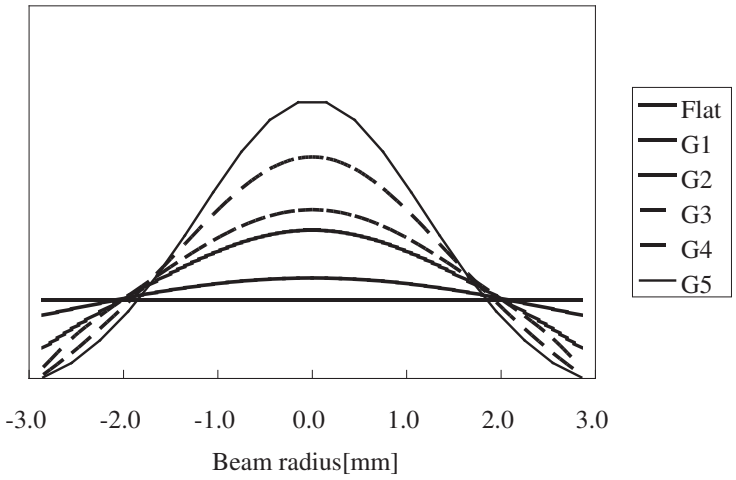

Figure 3.11: The Gaussian distribution. The standard deviation σ of the Gaussian distribution is defined as follows: G1; σ =1.20R$_{beam}$, G2; σ =1.00R$_{beam}$, G3; σ =0.80R$_{beam}$, G4; σ =0.55R$_{beam}$, and G5; σ =0.50R$_{beam}$.

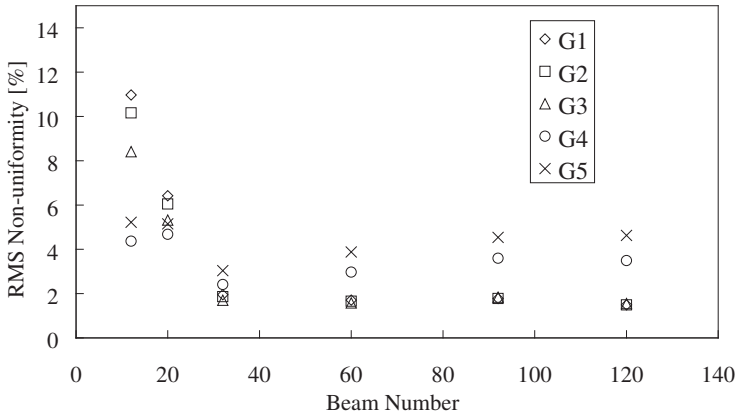

Figure 3.12: The RMS non-uniformity versus HIB total number in the case of Al layer target with the chamber radius of 5 m including the longitudinal beam temperature of 100 MeV and the transverse beam radial emittance of 5.0 mm mrad using five Gaussian types.

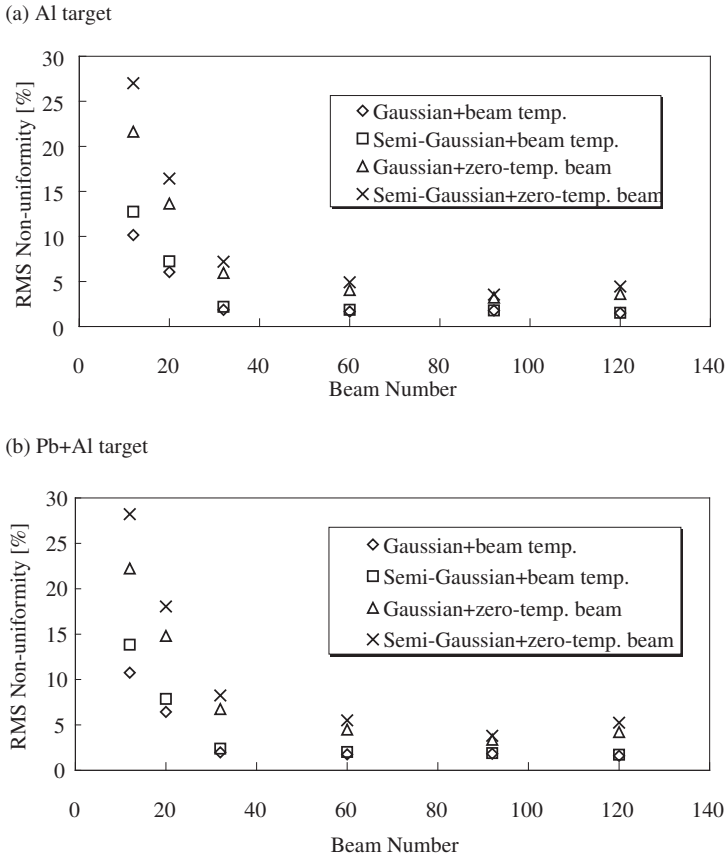

Figure 3.13: The RMS non-uniformity versus the HIB total number in the cases of a) Al layer target and b) Pb+Al layer target with the chamber radius of 5m. The marked diamonds, triangles, squares, and crosses mean the results in the cases of the Gauss distribution (G2) with and without the temperature effect, and of the semi-Gaussian distribution with and without the temperature effect, respectively.

(a) short ranging effect

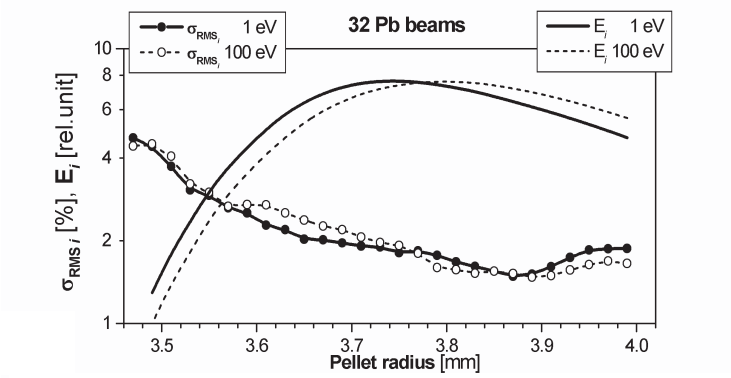

(b) target temperature v.s. RMS non-uniformity

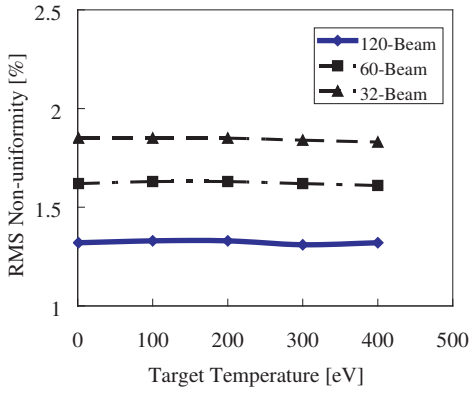

Figure 3.14: (a) The deposition energy of beam particles and RMS non-uniformity at each surface in the case with the beam temperature effect and target temperature (1 eV and 100 eV) for Al layer target, the chamber radius of 5 m, 32-beam system, and the semi-Gaussian distribution. (b) The RMS non-uniformity versus the target temperature.

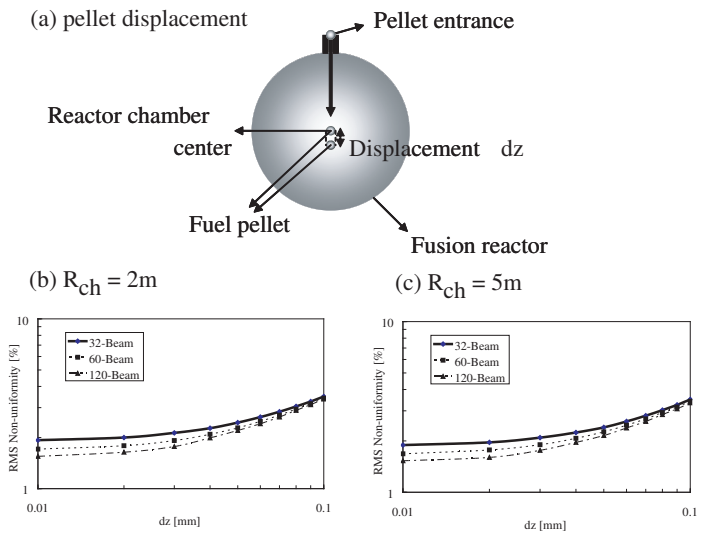

Figure 3.15: (a) Pellet displacement from the chamber center. The pellet displacement versus the RMS non-uniformity for the camber radius of (b) 2 m and (c) 5 m in the cases of 32, 60 and 120-beam systems.

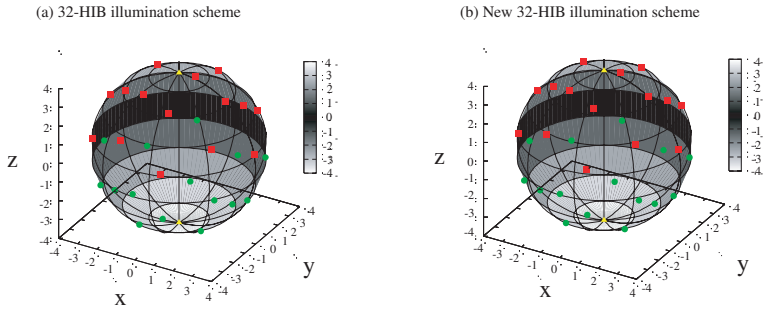

Figure 3.16: (a) Normal 32-HIBs illumination system. (b) New 32-HIBs illuminaiton system.

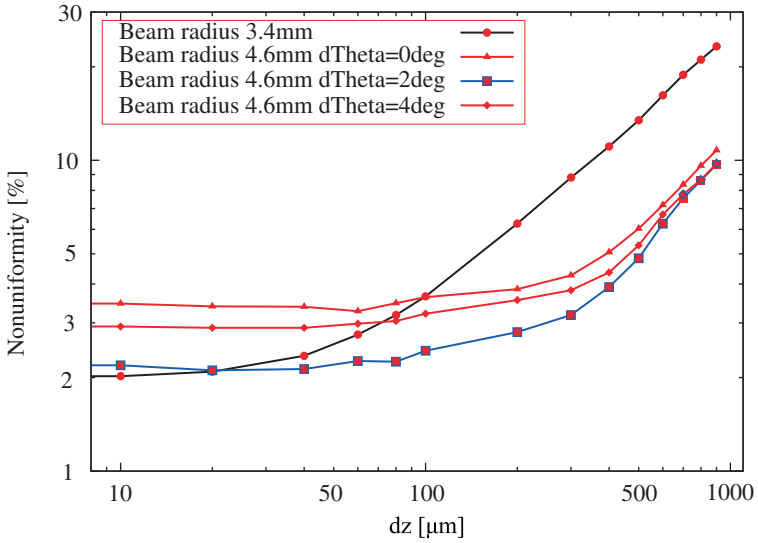

Figure 3.17: The RMS non-uniformity v.s. target displacement from the reactor chamber center in the cases of normal 32-HIBs illumination, using the large HIB radius and large HIB radius + new illumination scheme

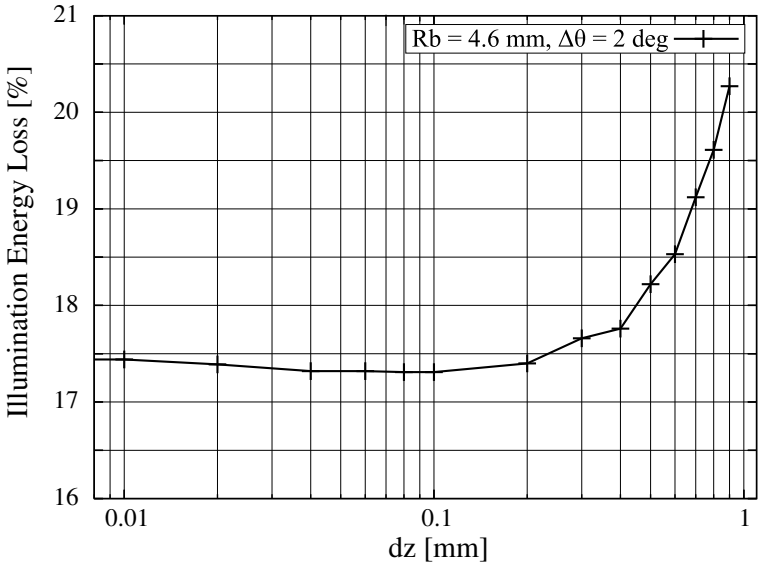

Figure 3.18: HIB energy loss as a function of pellet displacement.

Chapter 4

Target Hydrodynamics

4.1 Introduction

After impinging of the HIB particle to the fuel target, the pusher layer is ablated by thermal expansion due to the HIB deposition energy. Then the pusher layer pushes the DT fuel to a central direction. The DT fuel is compressed and achieved a high density/temperature state after a void close. During DT compression (target implosion) phase, an ablation front must be uniformed to be realize an effective implosion and fuel burning [37, 52]. However, a limited-HIB number illumination may induce the non-uniform ablation front and the non-uniform target implosion in a realistic case. Moreover, the pellet displacement from the chamber center as mentioned in Chapter 3 influence the non-uniform implosion and gain reduction.

Then, in order to calculate the fuel target implosion more realistically (of course include the pellet displacement effect), I couple the hydrodynamics code with the HIB illumination code [53] and analyze the target implosion during and after the HIB pulse duration.

The target energy gain required for energy production by ICF can be evaluated by considering a reactor energy balance as shown in Fig. 4.1. A driver pulse delivers an energy E_d to the target, which releases an amount of fusion energy E_{fus}. The energy gain is $G = E_{fus}/E_d$. The fusion energy is first converted into thermal energy of a blanket in a reactor chamber and then converted into electricity by a standard thermal cycle with an efficiency η_{th}. A fraction f of the electric power is recirculated to a the driver system, which converts it into beam energy with an efficiency η_d. The energy balance for

this cycle can be written $f\eta_d\eta_{th}G = 1$. Taking $\eta_{th} = 40\%$ and requiring that the recirculated fraction of electrical energy be smaller than 1/4, we find the condition $G\eta_d > 10$. For a driver efficiency in the range of $\eta_d = 10 - 33\%$, the condistion leads to a target gain of $G = 30 - 100$ required for power production. Especially, the required fusion gain is about 30 for the HIF because the HIB driver efficiency is about $\eta_d = 30\%$.

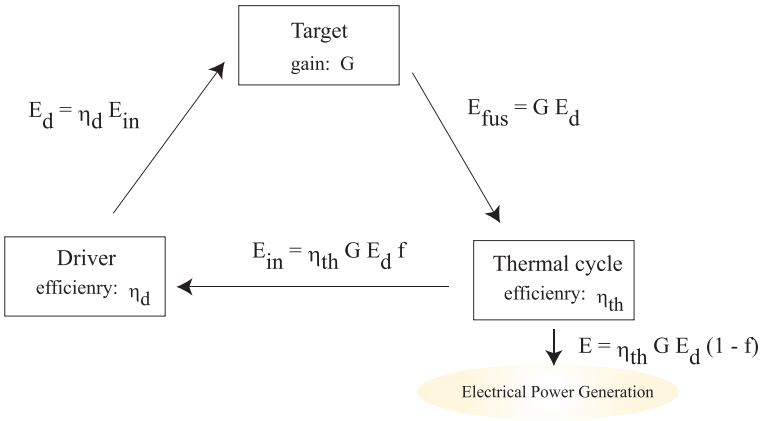

Figure 4.1: Energy balance of an ICF reactor.

In this chapter, a direct-indirect mixture implosion mode is proposed and discussed in heavy ion beam (HIB) inertial confinement fusion (HIF) in order to release sufficient fusion energy in a robust manner. On the other hand, the HIB illumination non-uniformity depends strongly on a target displacement gdzh in a reactor. In a direct-driven implosion mode dz of ~ 20 μm was tolerance and in an indirect-implosion mode dz of ~ 100 μm was allowable [10–13]. In the direct-indirect mixture mode target, a low-density foam layer is inserted, and radiation energy is confined in the foam layer. In the foam layer the radiation transport is expected in the lateral direction for the HIB illumination non-uniformity smoothing. Two-dimensional implosion simulations are performed, and show that the HIB illumination non-uniformity is well smoothed.

4.2 Simulation model

In HIF, the pulsed HIBs are illuminated on a fuel target. During the HIB illumination, the fuel target temperature becomes higher and higher. Therefore, the behavior of the target can be treated as a plasma hydrodynamics. In our developed hydrodynamics code, we solve basic hydrodynamic equations as follows.

4.2.1 Hydrodynamics

The physical model employed in this study is based on a three-temperature (an ion, an electron and a radiation temperatures) fluid model, because the high density state of a pellet material during the beam-interaction, implosion and burning phases is done. I also employ a heat conduction and a radiation transport effects. To capture the target material, I employ the color function [54]. Generally, calculation of a implosion is difficult to solve because the density, pressure and temperature gradient are very large, especially the burning phase. Therefore, in order to calculate high order accuracy in space and time, the R-CIP method [55–59] is employed for the advection term of a basic hydrodynamics equations.

A HIB ICF pellets employed in this study are presented in Figs. 4.2 (a), (b) and (c) in the cases of without a foam, a 0.5 mm thickness foam and a 1.0 mm thickness foam, respectively. The DT fuel contained is about 3.0 mg. The Pb-beam power pulse shape is shown in Fig. 4.3. The total Pb-ion-beam input energy is about 4 MJ. The ion-beam pulse duration is 34 nsec and the peak power is 320 TW. The Pb ion particle energy is 8 GeV.

4.2.2 Basic equations

The hydrodynamic basic equations are as follows:

$$\frac{\partial \rho}{\partial t} + (\mathbf{u} - v_r' \mathbf{n_r}) \cdot \nabla \rho \;\; = \;\; -\rho \nabla \cdot \mathbf{u}, \tag{4.1}$$

here, the ρ is target mass density in MKS unit and $\mathbf{u}$, v_r', $\mathbf{n_r}$ are advection velocity, mesh velocity for the ALE method [60–62] and unit vector for the

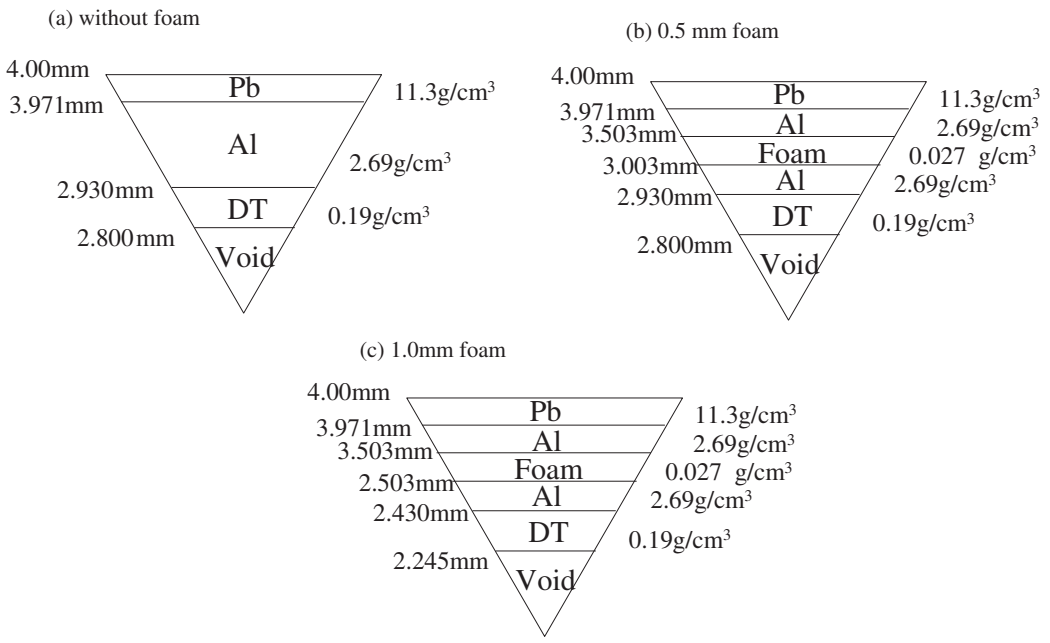

Figure 4.2: Fuel target structure in the cases of (a) without the foam, (b) the 0.5 mm foam and (c) the1.0 mm foam, respectively.

radial direction, respectively.

$$\frac{\partial v_r}{\partial t} + (\mathbf{u} - v_r'\mathbf{n_r}) \cdot \nabla v_r = -\frac{1}{\rho}\nabla(P+q)_r, \tag{4.2}$$

$$\frac{\partial v_\theta}{\partial t} + (\mathbf{u} - v_r'\mathbf{n_r}) \cdot \nabla v_\theta = -\frac{1}{\rho}\nabla(P+q)_\theta, \tag{4.3}$$

$$\frac{\partial v_\phi}{\partial t} + (\mathbf{u} - v_r'\mathbf{n_r}) \cdot \nabla v_\phi = -\frac{1}{\rho}\nabla(P+q)_\phi. \tag{4.4}$$

The v_r, v_θ, and v_ϕ are target plasma velocity for the radial, θ and ϕ directions, respectively. The P and q are total pressure and an artificial viscosity [55, 63].

$$C_{vi}\frac{\partial T_i}{\partial t} + (\mathbf{u} - v_r'\mathbf{n_r}) \cdot \nabla T_i = -\frac{P_{thi}+q}{\rho} \cdot \mathbf{u} + H_i - K_{ie} + S_i, \tag{4.5}$$

$$C_{ve}\frac{\partial T_e}{\partial t} + (\mathbf{u} - v_r'\mathbf{n_r}) \cdot \nabla T_e = -\frac{P_{the}}{\rho} \cdot \mathbf{u} + H_e + K_{ie} - K_{re} + S_e, \tag{4.6}$$

$$C_{vr}\frac{\partial T_r}{\partial t} + (\mathbf{u} - v_r'\mathbf{n_r}) \cdot \nabla T_r = -\frac{P_{thr}}{\rho} \cdot \mathbf{u} + H_r + K_{re}. \tag{4.7}$$

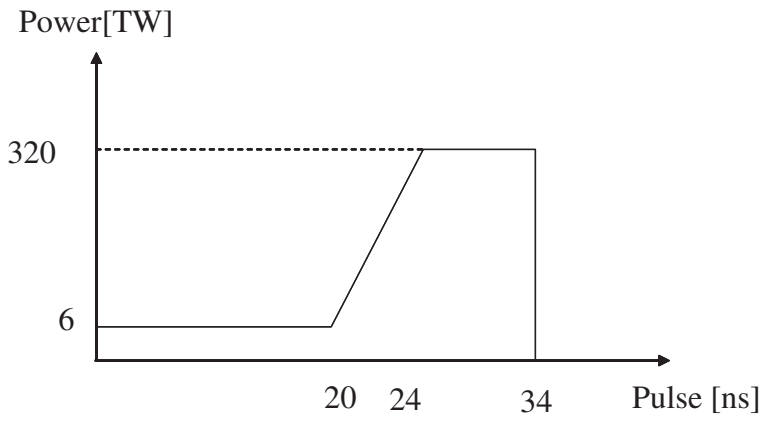

Figure 4.3: Input HIB pulse.

The C_{vi}, C_{ve} and C_{vr} show a specific heats of an ion, an electron and a radiation, respectively. T_i, T_e, and T_r are an ion, an electron and a radiation temperatures. Moreover the P_{thi}, P_{the} and P_{thr} are thermal pressures of an ion, an electron and a radiation, respectively. In the energy equation, the H_i and H_e are heat conduction terms, and K_{ie}, K_{re} are heat exchange terms between an ion-electron and a radiation-electron, respectively. The S_i and S_e are the deposition energy by the stopping power calculated by HIB-Illumination code.

4.2.3 Heat conduction

The ion and electron temperatures have an effect of heat conduction [64–67] in each temperatures. The heat conduction rates of the ion and the electron are as follows:

$$H_i = \frac{1}{\rho}\nabla\kappa_i\nabla T_i, \tag{4.8}$$

$$H_e = \frac{1}{\rho}\nabla\kappa_e\nabla T_e, \tag{4.9}$$

$$\kappa_i = 4.3\times10^{-12}T_i^{5/2}(\log\Lambda)^{-1}M^{-1/2}Z^{-4}, \tag{4.10}$$

$$\kappa_e = 1.83\times10^{-10}T_e^{5/2}(\log\Lambda)^{-1}Z^{-1}. \tag{4.11}$$

4.2.4 Radiation transport

In this study, a flux limited radiation transport of a diffusion approximation is employed as follows [68, 69]:

$$C_{vr}\frac{\partial T_r}{\partial t} = \frac{1}{\rho}\nabla \mathbf{F}, \tag{4.12}$$

$$= \frac{1}{\rho}\nabla \kappa_r \nabla T_r, \tag{4.13}$$

$$\kappa_r = \frac{16}{3}\sigma L_R T_r^3, \tag{4.14}$$

here, the $\mathbf{F}$ and κ_r are a radiation flux and conductivity.

4.2.5 Enegy exchange

The energy exchange terms in Eqs. (4.5) and (4.6) are solved by these equations as follows [65, 66]:

$$K_{ie} = C_{vi}\omega_{ie}(T_i - T_e), \tag{4.15}$$

$$K_{re} = C_{ve}\omega_{re}(T_e - T_r), \tag{4.16}$$

here, the ω_{ie} and ω_{re} are ion-electron and radiation-electron collision frequencies as follows, respectively.

$$\omega_{ie} = \frac{Z^2 e^4 n_i \ln\Lambda\sqrt{m_e}}{32\sqrt{2}\pi\epsilon_0^2 M m_p (kT_e)^{3/2}}, \tag{4.17}$$

here, Z is charge state, e elementary charge, n_i ion number density, m_e electron mass, ϵ_0 permittivity of free space, M mass number, k the Boltzmann's constant, and T_e electron temperature in [K].

$$\omega_{re} = \omega'_{re} + \omega_{cr}, \tag{4.18}$$

here,

$$\omega'_{re} = 8.5\times 10^{-14}(<Z>^2<Z>n_i/MT_e^{1/2}C_{ve})I_g, \tag{4.19}$$

$$I_g = \int_0^\infty \frac{\xi(e^{\xi u}-e^u)}{(\xi-1)(e^{\xi u}-1)(e^u-1)}du, \tag{4.20}$$

here, $u = h\nu/kT_e$, $\xi = T_e/T_r$. h and ν are the Plank's constant and collision frequency.

$$\omega_{cr} = \frac{128}{3}\frac{e^4\sigma}{m_e^3c^6}T_r^4, \tag{4.21}$$

here, σ is the Stefan's constant.

4.2.6 Fusion reaction

The number densities of deuterium and tritium change after the fusion reaction. Moreover α-particle and neutrons are produced by the nuclear reaction. To include these effect, we employ the DT, DD and DHe^3 fusion reactions [21, 70] as follows: DHe^3 and DT reactions are

$$\mathrm{D} + {}^3\mathrm{He} \rightarrow {}^4\mathrm{He}(3.67\mathrm{MeV}) + \mathrm{p}(14.67\mathrm{MeV}), \tag{4.22}$$
$$\mathrm{D} + \mathrm{T} \rightarrow {}^4\mathrm{He}(3.5\mathrm{MeV}) + \mathrm{n}(14.1\mathrm{MeV}). \tag{4.23}$$

The reaction cross sections are

$$< \sigma v > = \exp(x_1 - \frac{x_2}{T^{x_5}} + \frac{x_3}{T + x_4}), \tag{4.24}$$
$$x_1 = -47.6101500072032,$$
$$x_2 = 31.7647772245972,$$
$$x_3 = 2802.93951496279,$$
$$x_4 = 374.186068136729,$$
$$x_5 = 0.286712265913130\ (for\ \mathrm{DHe}^3\ reactions). \tag{4.25}$$

The coefficients of the DT reaction are

$$x_1 = -49.9580809680824,$$
$$x_2 = 18.1155080330636,$$
$$x_3 = 895.149425658926,$$
$$x_4 = 135.888636700177,$$
$$x_5 = 0.366290140624939\ (for\ \mathrm{DT}\ reactions). \tag{4.26}$$

The DD reactions are

$$\mathrm{D} + \mathrm{D} \rightarrow \mathrm{T}(1.01\mathrm{MeV}) + \mathrm{p}(3.03\mathrm{MeV}), \tag{4.27}$$
$$\mathrm{D} + \mathrm{D} \rightarrow {}^3\mathrm{He}(0.82\mathrm{MeV}) + \mathrm{n}(2.45\mathrm{MeV}). \tag{4.28}$$

The cross section is

$$
\begin{aligned}
<\sigma v> &= \exp(x_1 - \frac{x_2}{T^{x_5}} + \frac{x_3 T}{(T^2 + x_4)^2}), && (4.29)\\
x_1 &= -49.1789720673151,\\
x_2 &= 15.3267580380585,\\
x_3 &= -4168271.58512757,\\
x_4 &= 36677.9694366768,\\
x_5 &= 0.365303247159742. && (4.30)
\end{aligned}
$$

The number density change by the fusion reaction. Therefore, the number densities of the deuterium, tritium, α particle, neutron and He^3 are re-calculated by Eq. (4.31).

$$
\begin{aligned}
n_D^{n+1} &= n_D^n + (-n_D n_T \langle\sigma v\rangle_{DT} - n_D^2 \langle\sigma v\rangle_{DD}\\
&\quad - n_D n_{He^3} \langle\sigma v\rangle_{DHe^3})\Delta t, && (4.31)\\
n_T^{n+1} &= n_T^n + (-n_D n_T \langle\sigma v\rangle_{DT} + n_D^2/4\langle\sigma v\rangle_{DD})\Delta t, && (4.32)\\
n_\alpha^{n+1} &= n_\alpha^n + (n_D n_T \langle\sigma v\rangle_{DT} + n_D n_{He^3} \langle\sigma v\rangle_{DHe^3})\Delta t, && (4.33)\\
n_{He^3}^{n+1} &= n_{He^3}^n + (n_D^2/4\langle\sigma v\rangle_{DD} - n_D n_{He^3} \langle\sigma v\rangle_{DHe^3})\Delta t, && (4.34)\\
n_n^{n+1} &= n_n^n + (n_D^2/4\langle\sigma v\rangle_{DD} + n_D n_T \langle\sigma v\rangle_{DT})\Delta t, && (4.35)\\
n_p^{n+1} &= n_p^n + (n_D^2/4\langle\sigma v\rangle_{DD} + n_D n_{He^3} \langle v\rangle_{DHe^3})\Delta t. && (4.36)
\end{aligned}
$$

4.2.7 Alpha particle deposition

After the fuel ignition, the α-particle is produced by fusion reaction as follows [71, 72]:

$$\mathrm{D} + \mathrm{T} \rightarrow \mathrm{He} + \mathrm{n} + 17.6\mathrm{MeV}, \quad (4.37)$$

here, D, T, He and n are the deuterium, tritium, α-particle and neutron, respectively. The neutron goes through the outside of target plasmas without interaction with the hot plasma. However, the fuel target is heated by the α-particle deposition because the mean free path of the α-particle in the high density plasmas is short. Therefore, in order to include this effect, the α-particle deposition on the plasmas is solved as the diffusion approximation as follows:

$$\frac{\partial T_e}{\partial t} = \frac{1}{\rho C_{ve}} \omega_{\alpha e} E_\alpha n_\alpha, \tag{4.38}$$

$$\frac{\partial T_i}{\partial t} = \frac{1}{\rho C_{vi}} \omega_{\alpha i} E_\alpha n_\alpha. \tag{4.39}$$

The $\omega_{\alpha e}$ and $\omega_{\alpha i}$ are collision frequency between the electron-α particle and the ion-α particle, respectively. E_α and n_α are α-particle energy (i.e. 3.5 MeV) and number density of the α-particle. In Eqs. (4.38) and (4.39), n_α is solved by this equation:

$$\begin{aligned} \frac{\partial n_\alpha}{\partial t} &= -\nabla D_\alpha \nabla n_\alpha + n_D n_T < \sigma v >_{DT} \\ &\quad + n_D n_{He^3} < \sigma v >_{DHe^3} - \omega_\alpha n_\alpha, \end{aligned} \tag{4.40}$$

here, D_α is a diffusion coefficient of the α-particle. The n_D, n_T, $< \sigma v >_{DT}$ and $< \sigma v >_{DHe^3}$ are number density of the deuterium, tritium and the cross sections of D-T and D-He^3 reactions, respectively. To solve these equations, we also use the ADI method same as a heat conduction term.

$$D_\alpha = \frac{1}{3} \frac{E_\alpha}{m_\alpha \omega_\alpha}. \tag{4.41}$$

The m_α is mass of α-particle.

$$\omega_\alpha = \omega_{\alpha i} + \omega_{\alpha e}, \tag{4.42}$$

$$\omega_{\alpha i} \approx 9.0 \times 10^{-8} (\frac{1}{\mu_\alpha} + \frac{1}{\mu_i}) \frac{\mu_\alpha^{1/2}}{E_\alpha^{3/2}} n_i Z_\alpha^2 Z^2 \ln \Lambda, \tag{4.43}$$

here, $\mu_\alpha = m_\alpha / m_p$ and $\mu_i = m_i / m_p$.

$$\omega_{\alpha e} \approx \begin{cases} \frac{1.6 \times 10^{-9} n_e Z^2 \ln \Lambda_{ie}}{\mu T_e^{3/2}} & \text{if } T_e[eV] > \frac{3.5 \times 10^6}{4 \times m_e / m_p}, \\ \frac{1.7 \times 10^{-4} \mu^{1/2} n_e Z^2 \ln \Lambda_{ie}}{E_\alpha^{3/2}} & \text{else.} \end{cases}$$

4.3 Simulation results

4.3.1 Without foam

In order to study relationship between the HIB energy deposition on an energy absorber of a fuel pellet and the non-uniformity smoothing effect by the radiation transport effect on a pellet implosion, we calculate the target plasma hydrodynamics and fuel ignition by using the hydrodynamics code coupling with the HIB illumination code. We employ a 32-HIBs illumination system. In this thesis, two-dimensional (in spherical coordinate) simulations are performed, and the two-dimensional HIB illumination time-dependent pattern at ϕ=90 deg is employed from the HIB illumination code [53].

Figure 4.2(a) shows the fuel target. The Pb, Al and DT layer thicknesss and mass densities are 0.03 mm, 0.40 mm, 0.10 mm, 11.3 g/cm^3, 2.69 g/cm^3 and 0.19 g/cm^3 , respectively. The HIB pulse is as shown in Fig 4.3. In this case, the total HIB energy is 4.0 MJ.

Figures 4.4 $\sim$ 4.6 show the target materials, the density and the total pressure at 0 nsec, 24 nsec, 33 nsec, 35 nsec and 36 nsec, respectively. Figures 4.7 and 4.8 present the ion temperature and the radial velocity at 24 nsec, 33 nsec, 35 nsec and 36 nsec, respectively.

Figure 4.9 presents a mean density and a mean radiation temperature averaged over the θ direction at 0.37 nsec, 34.9 nsec and 36.2 nsec, respectively.

The averaged HIB illumination non-uniformity is 2.3 % in this case. The Pb beam ions impinge the pellet surface as shown in Fig. 4.9. The HIB deposition energy distribution induces an ablation region at the front of the DT fuel, and then about one-third of Al pusher mass pushes the DT fuel. From Figs. 4.5, we can see the low density region outside of the ablation front.

The limited number of beams induce the large non-uniform compression. We can see the large non-uniformly ablation front from the profile of the ion temperature, especially at 33 nsec and 35 nsec (see Fig. 4.7). We also confirm that the large non-uniform implosion is done from the target density, the total pressure and the radial velocity profile. Especially, the fuel DT is compressed non-uniformly near the void close.

Figure 4.10 presents (a) the gain curve, (b) the maximum ion temperature and (c) the mean ρR as a function of pellet displacement dz from the chamber

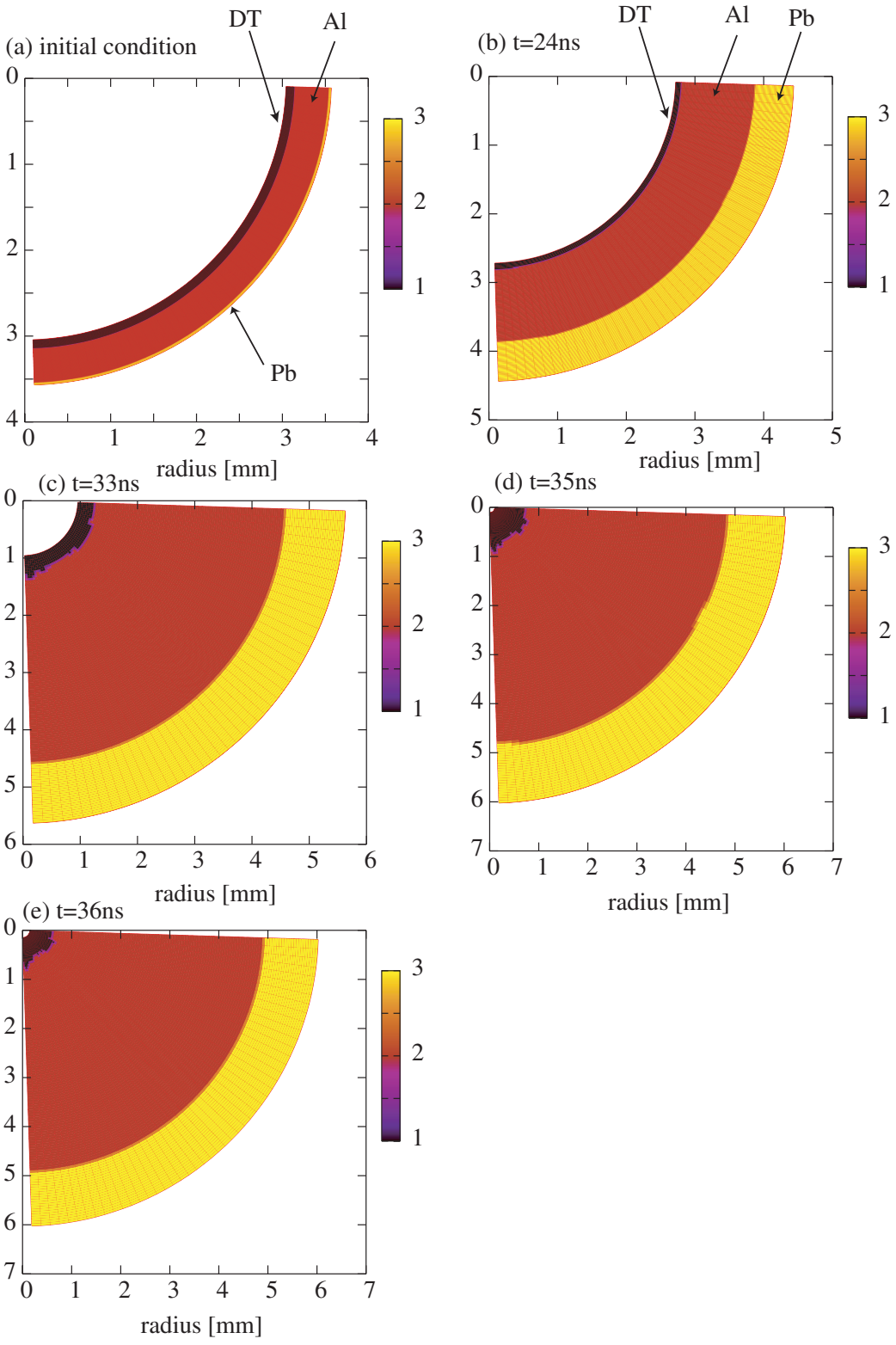

Figure 4.4: The target materials in the case without the foam. The value of 1, 2, and 3 present the DT fuel, the Al pusher and the Pb tamper, respectively.

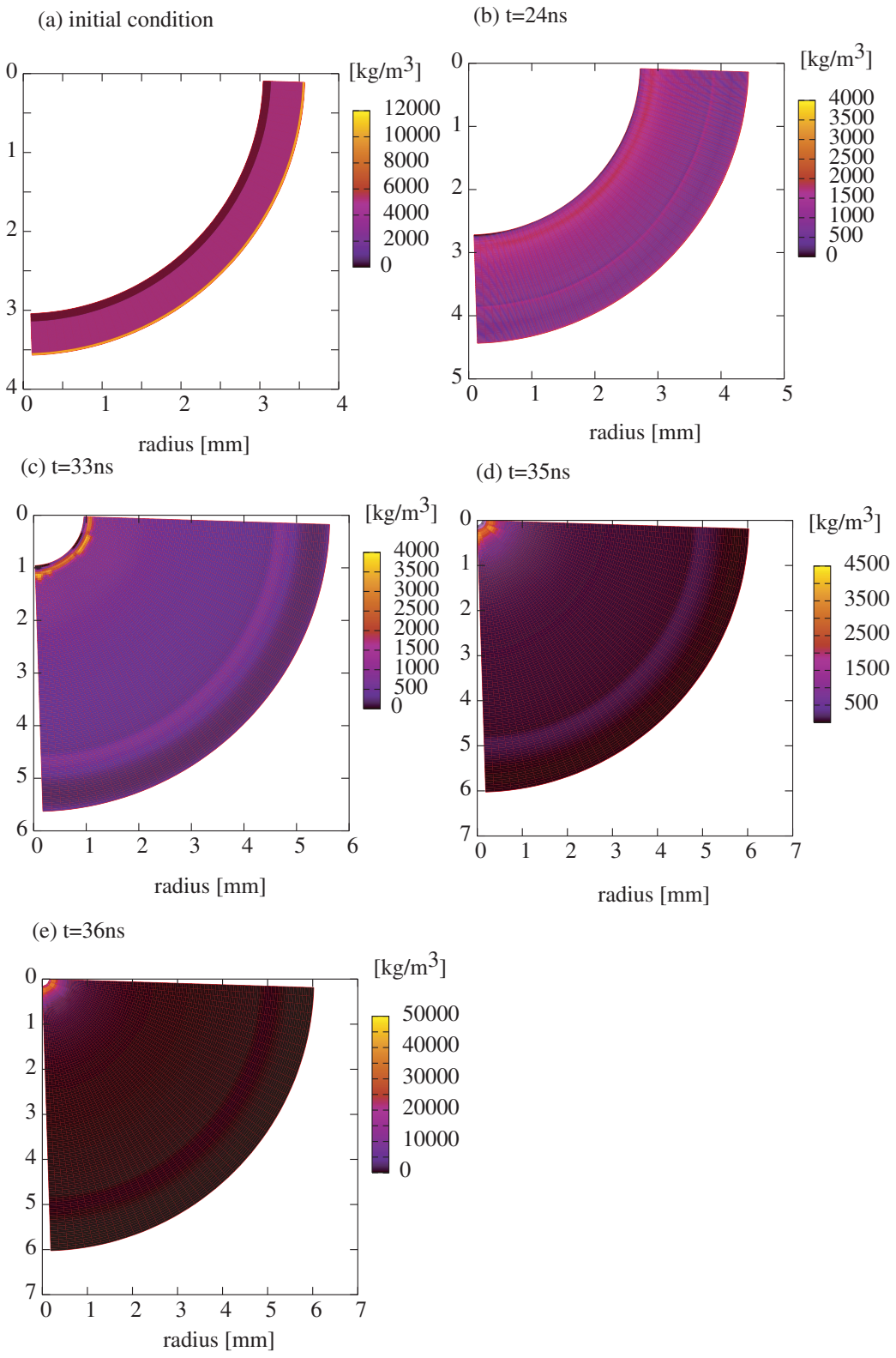

Figure 4.5: The target density profile in the case without the foam.

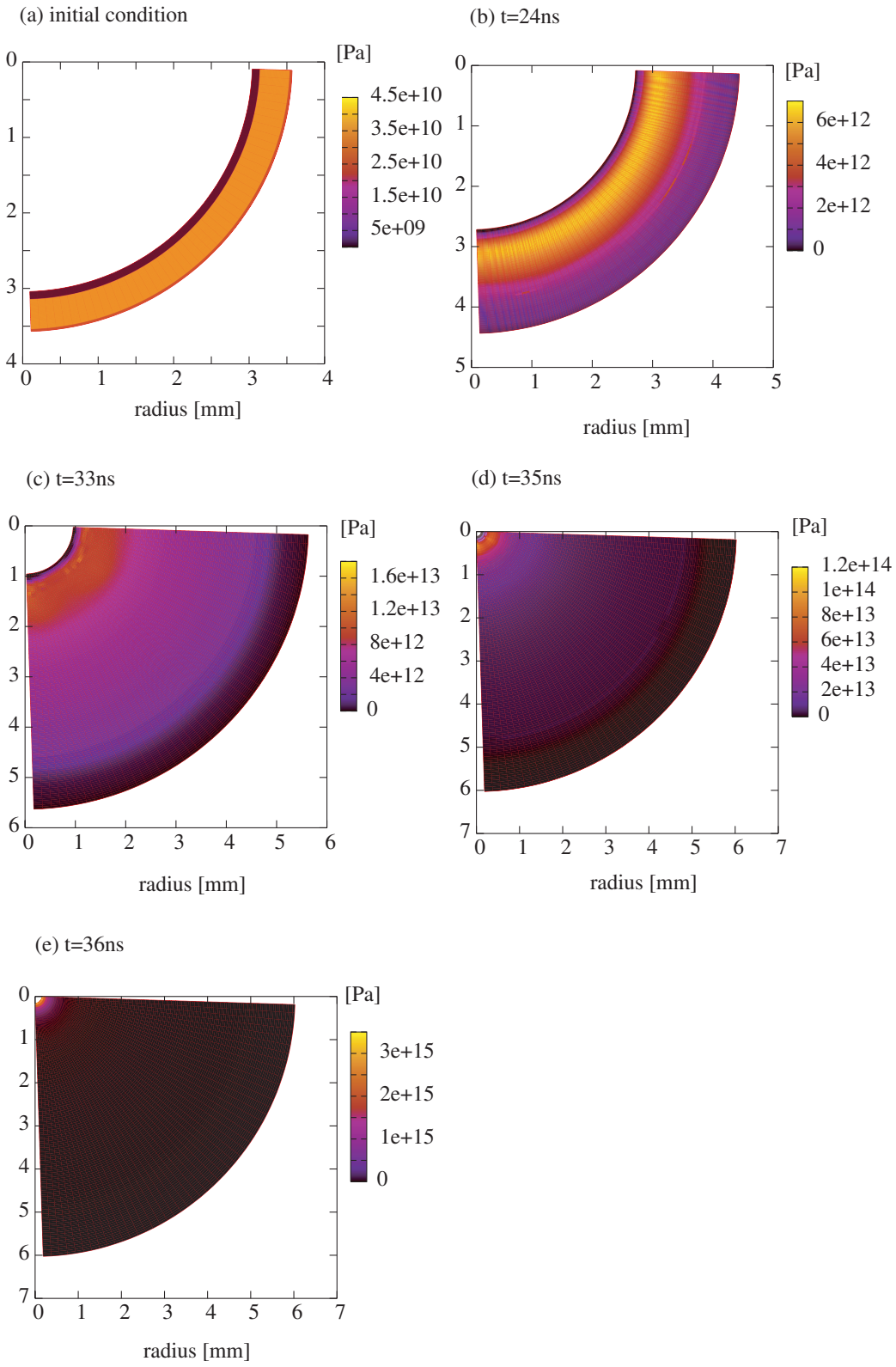

Figure 4.6: The total pressure in the case without the foam.

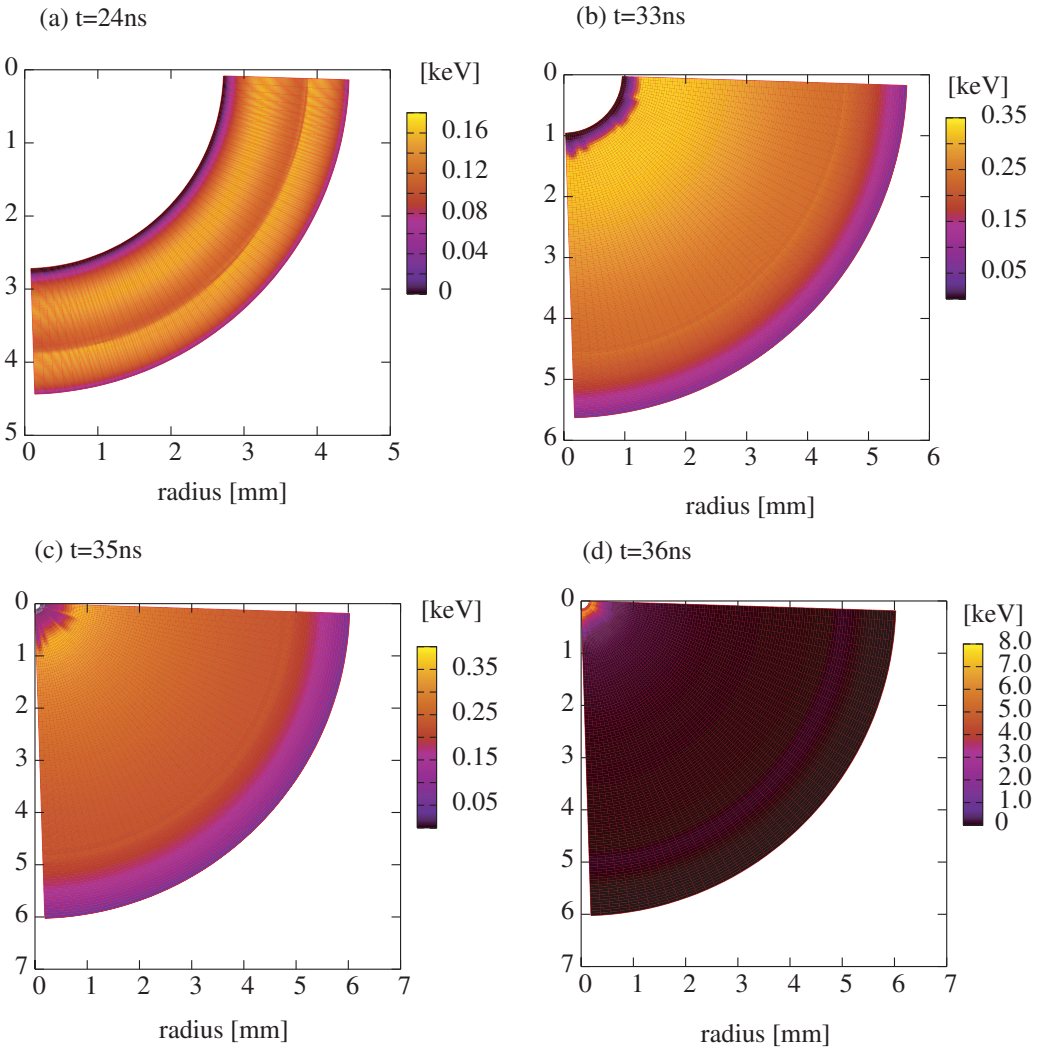

Figure 4.7: The target ion temperature in the case without the foam.

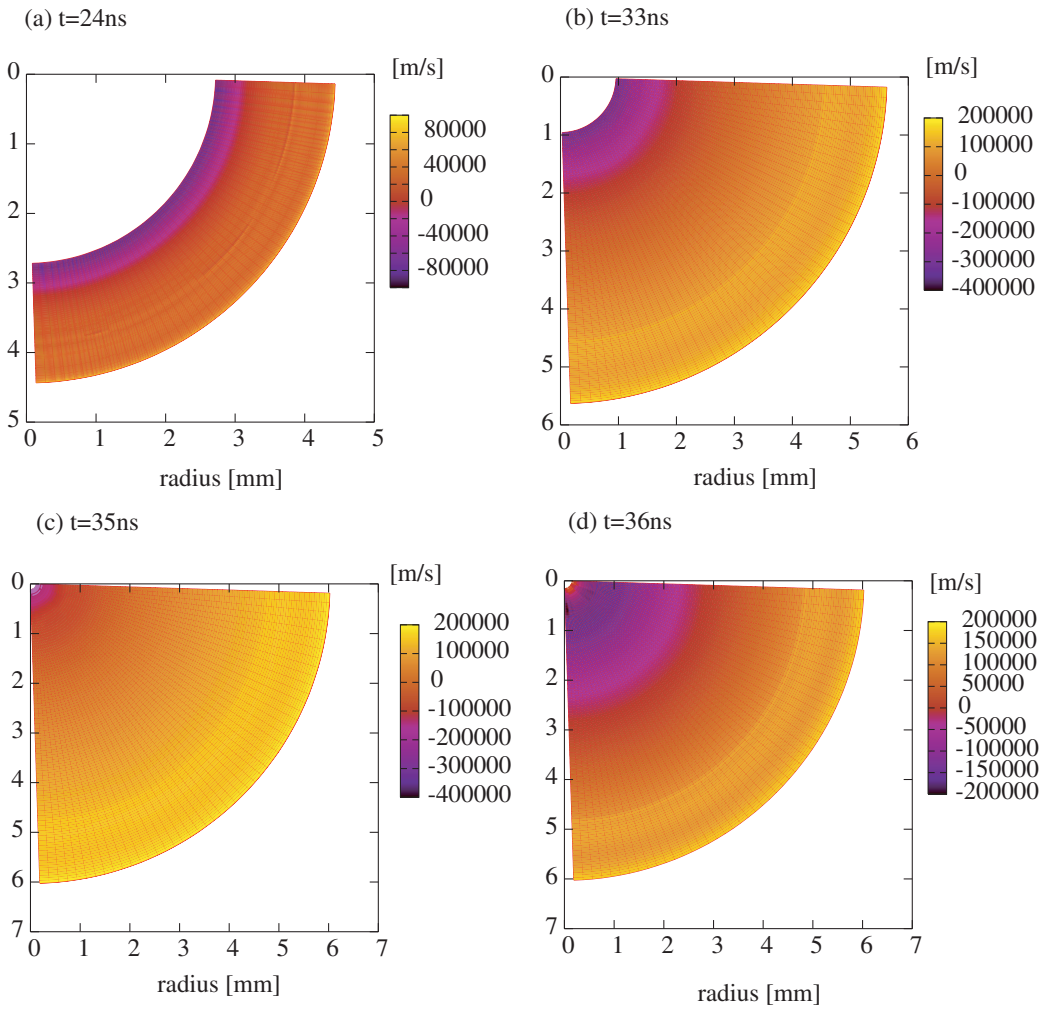

Figure 4.8: The radial velocity in the case without the foam.

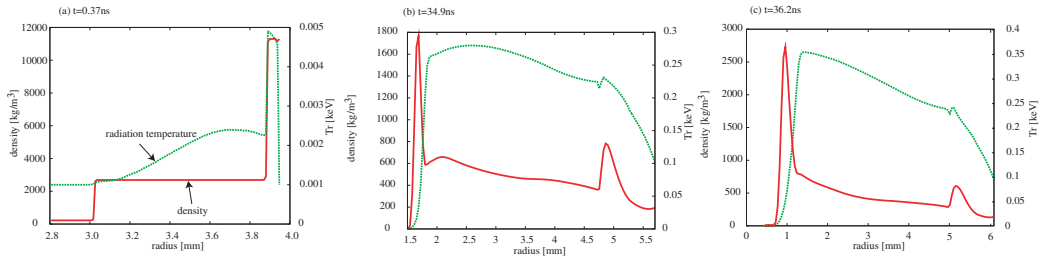

Figure 4.9: The mean density and the mean radiation temperature averaged over the θ direction in the case of without foam at (a) 0.37 ns, (b) 34.9 ns and (c) 36.2 ns, respectively.

center. In this study, we calculate the mean ρR using this equation [64, 73],

$$\bar{\rho R} = \frac{\int\int\int_0^R \rho r \rho r^{g-1} dr d\theta d\phi}{\int\int\int_0^R \rho r^{g-1} dr d\theta d\phi}. \tag{4.44}$$

Here, the g is geometry factor (1 is cartesian, 2 cylindrical and 3 spherical coordinate). As described in Introduction in this Chapter, the gain must be larger than 30 in order to obtain sufficient fusion energy by ICF. However, the gain decrease dramatically when the pellet displacement becomes larger and larger. Therefore, it may be difficult to use the fusion electric power generation system in this case even dz = 0. Moreover, we can also see that the maximum ion temperature and the mean ρR are decreased for a large pellet displacement.

Figures 4.11 and 4.12 are implosion non-uniformity of (a) the target density, (b) the total pressure, (c) the ion temperature and (d) the radial-velocity at the void closure time and maximum ρR time as a function of dz, respectively. The non-uniformity is calculated by root mean square (RMS). We employ the maximum value as a non-uniformity for a radial direction. From these figures, the implosion non-uniformity increase for large pellet displacement.

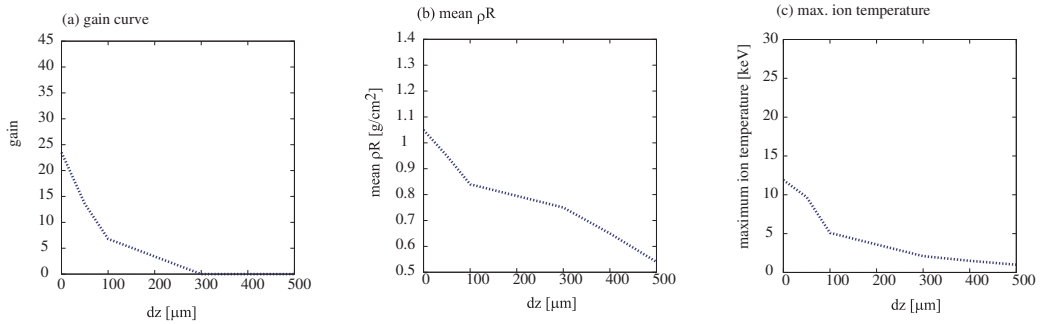

Figure 4.10: (a) The gain curve, (b) the mean ρR calculated by Eq. 4.44 and (c) the maximum ion temperature v.s. pellet displacement in the case without the foam.

4.3.2 With foam

In the direct-indirect mixture mode target, a low-density foam layer is inserted as shown in FIg. 4.2(b), and radiation is confined in the foam layer. In the foam layer the radiation transport is expected in the lateral direction for the HIB illumination non-uniformity smoothing. Figure 4.2(b) present the fuel target, and consisted of five layers of a solid Pb, a solid Al, a foam Al, a solid Al, and DT. The foam Al density is 0.01 times the Al solid density. We call the "direct-indirect mixture implosion mode" this target. In this section, we also employ the 32-HIBs illumination system. Figures 4.13 to 4.17 are the target material, the density, the total pressure, the ion temperature and the radial velocity at 0 nsec, 34 nsec, 42 nsec, 46 nsec and 52 nsec in the case of the 0.5 mm foam, respectively.

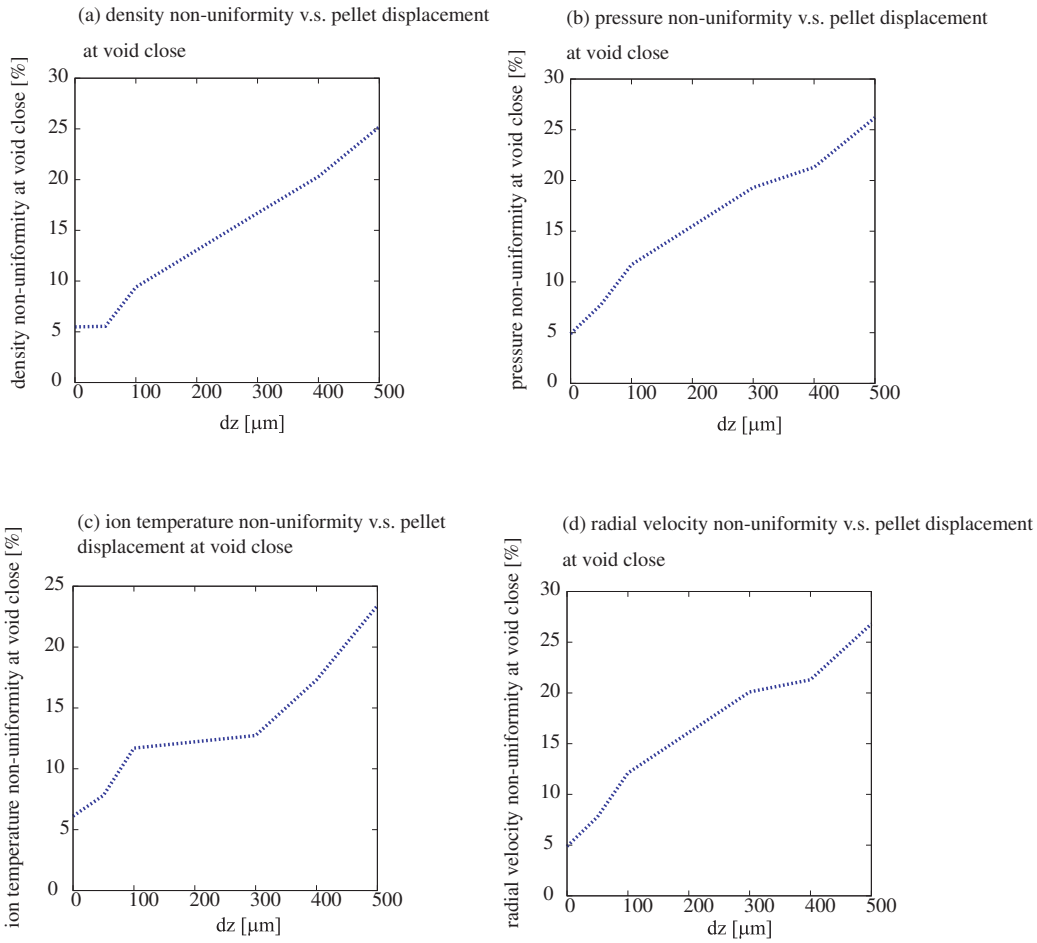

Figure 4.11: (a) The density, (b) the total pressure, (c) the ion temperature and (d) the radial velocity non-uniformity v.s. pellet displacement dz at void close in the case without the foam.

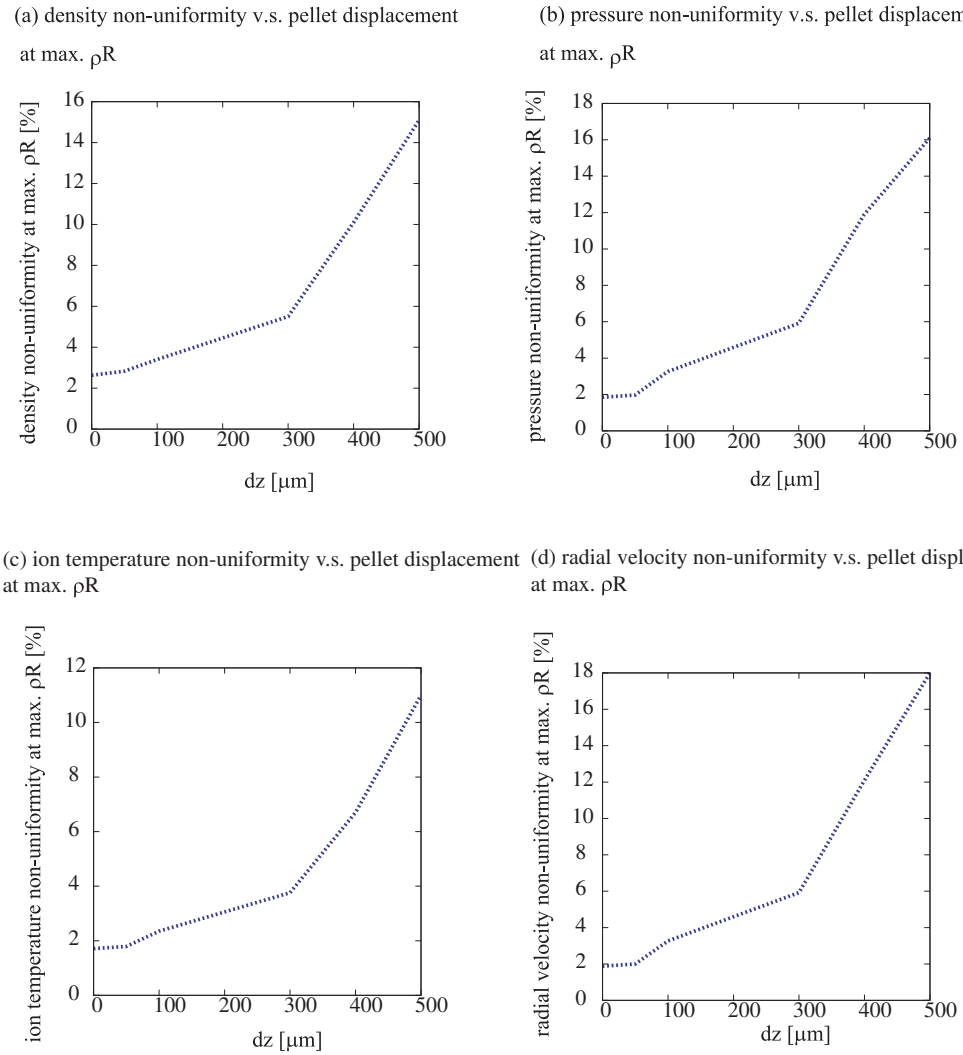

Figure 4.12: (a) The density, (b) the pressure, (c) the ion temperature and (d) radial velocity non-uniformity v.s. pellet displacement dz at time of maximum ρR in the case without the foam.

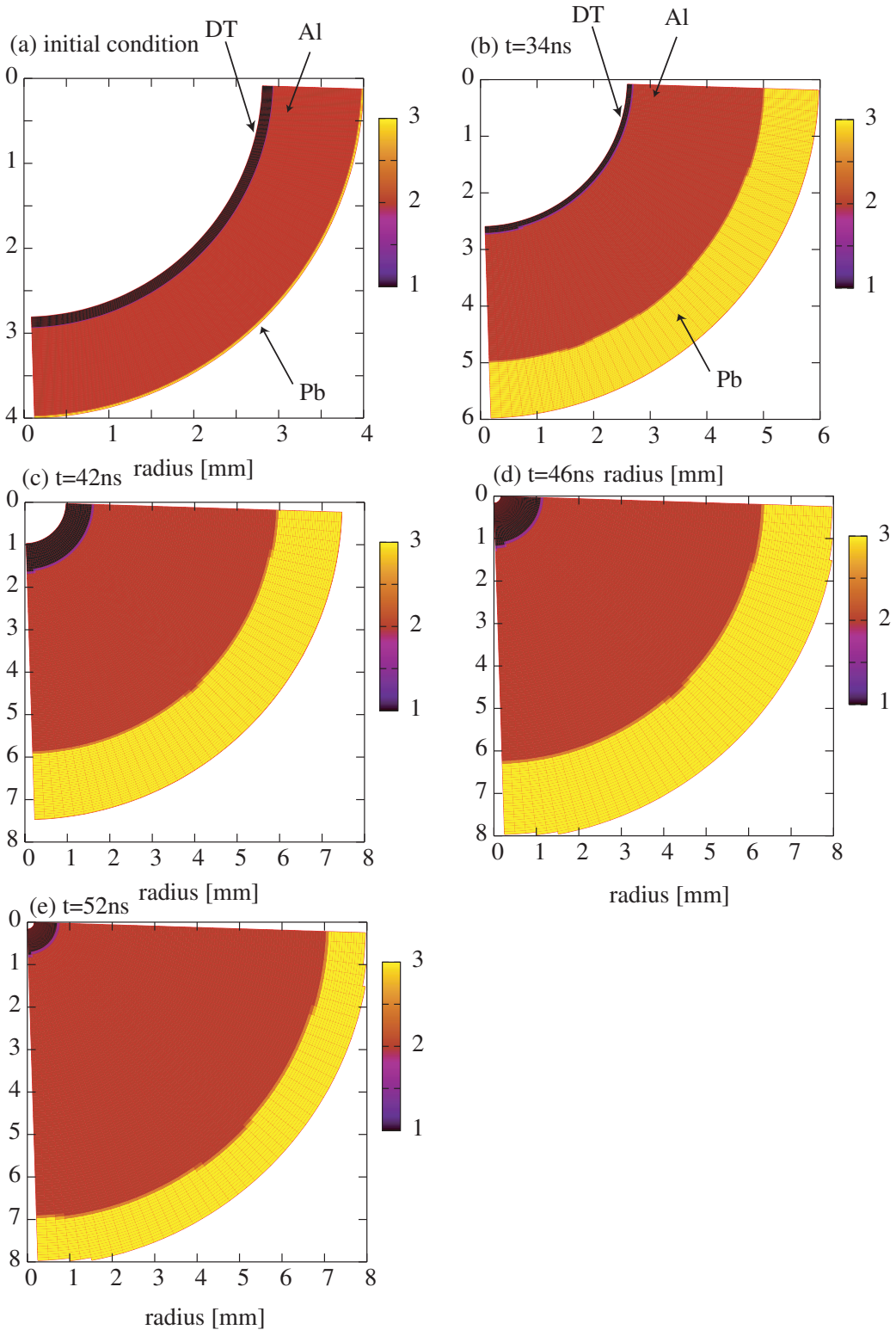

Figure 4.13: The target materials in the case of the 0.5mm foam. The value of 1, 2, and 3 present the DT fuel, Al pusher and Pb tamper, respectively.

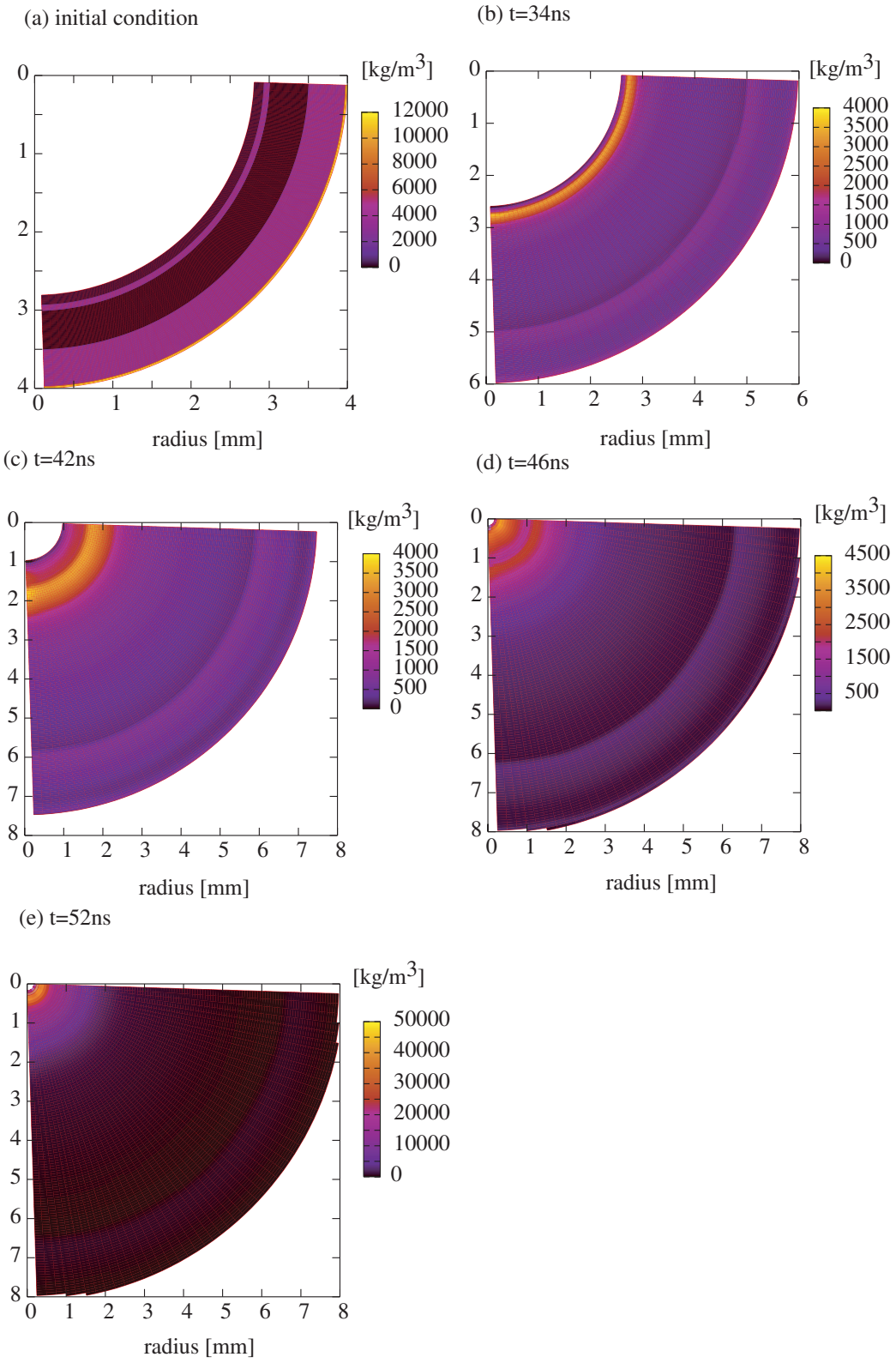

Figure 4.14: The target density profile in the case of the 0.5 mm foam.

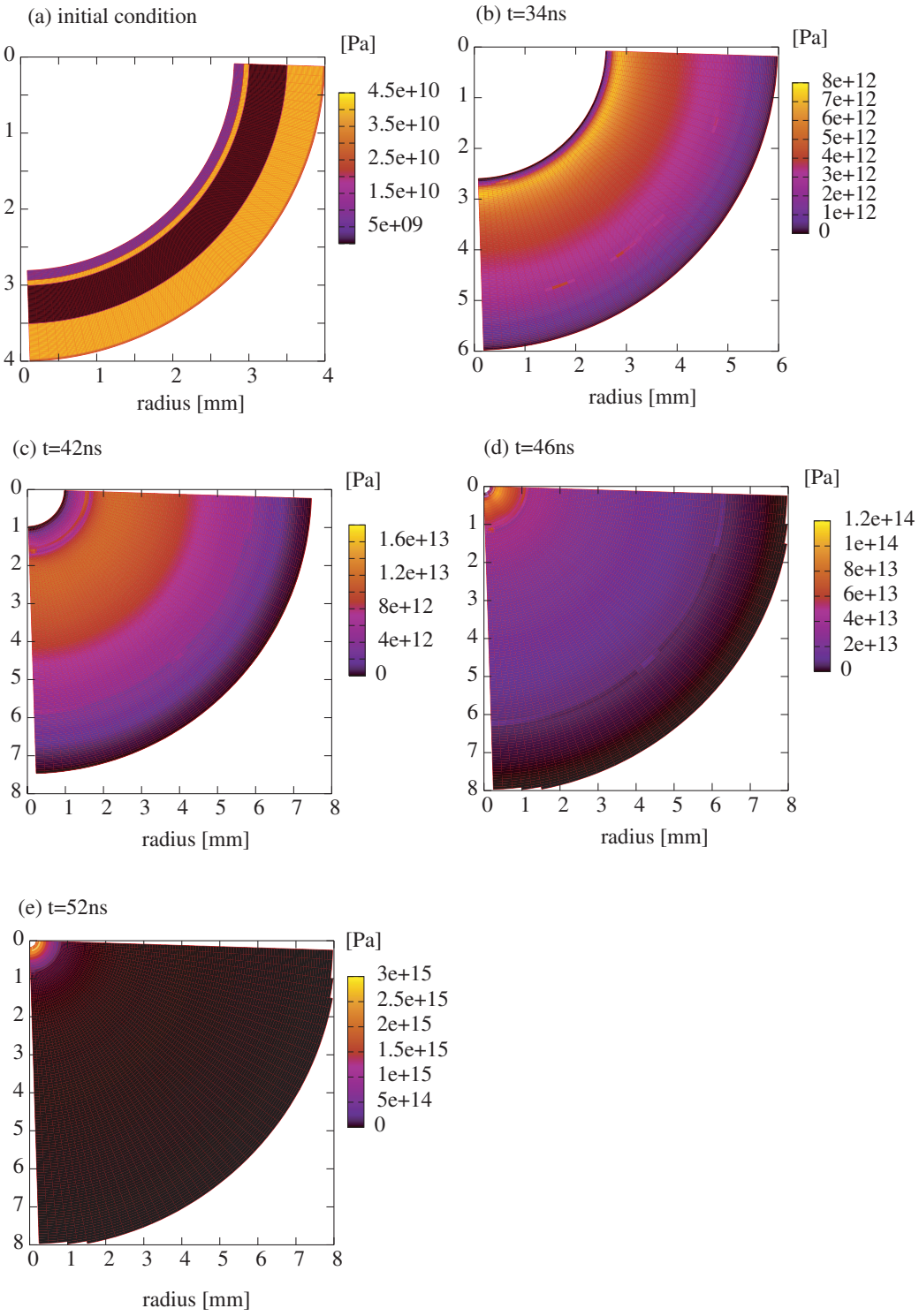

Figure 4.15: The target total pressure in the case of the 0.5 mm foam.

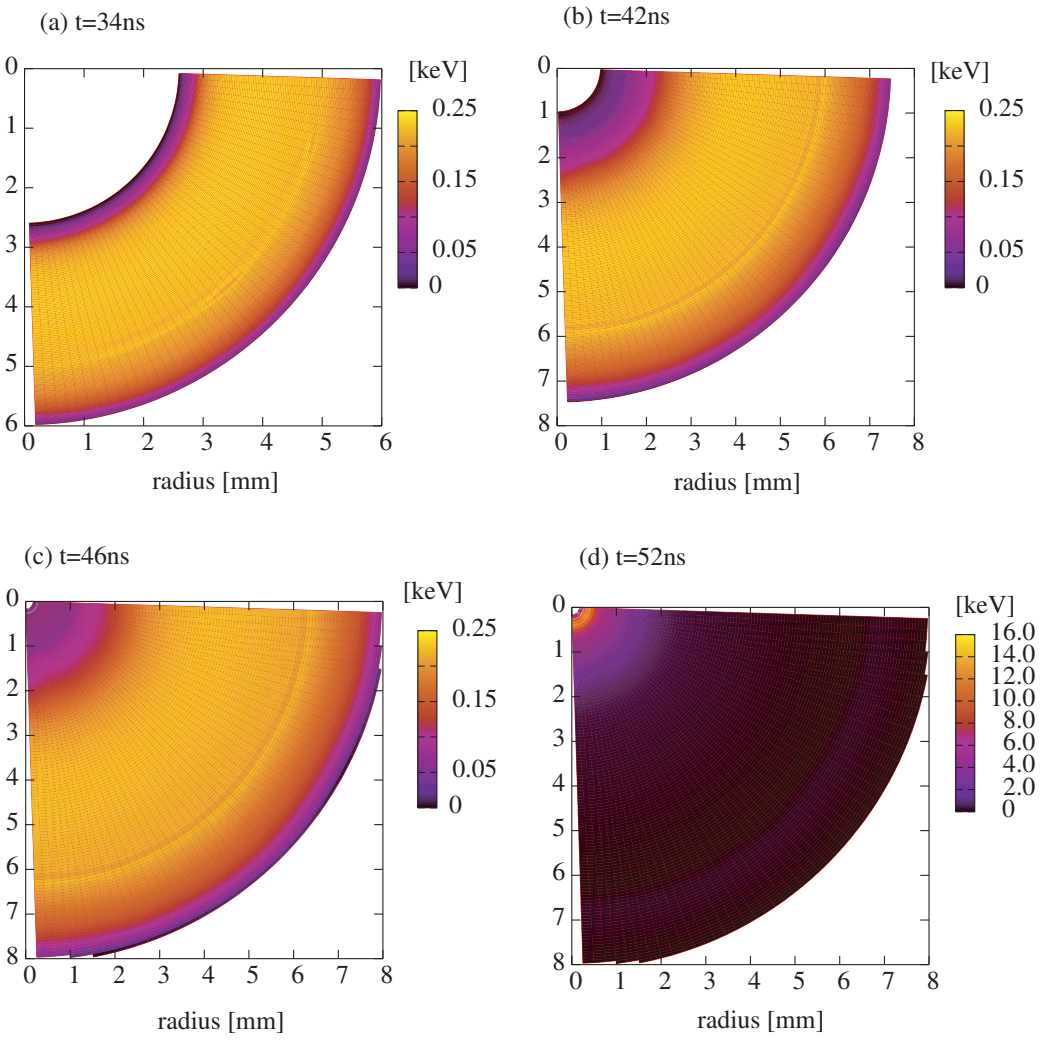

Figure 4.16: The target ion temperature in the case of the 0.5 mm foam.

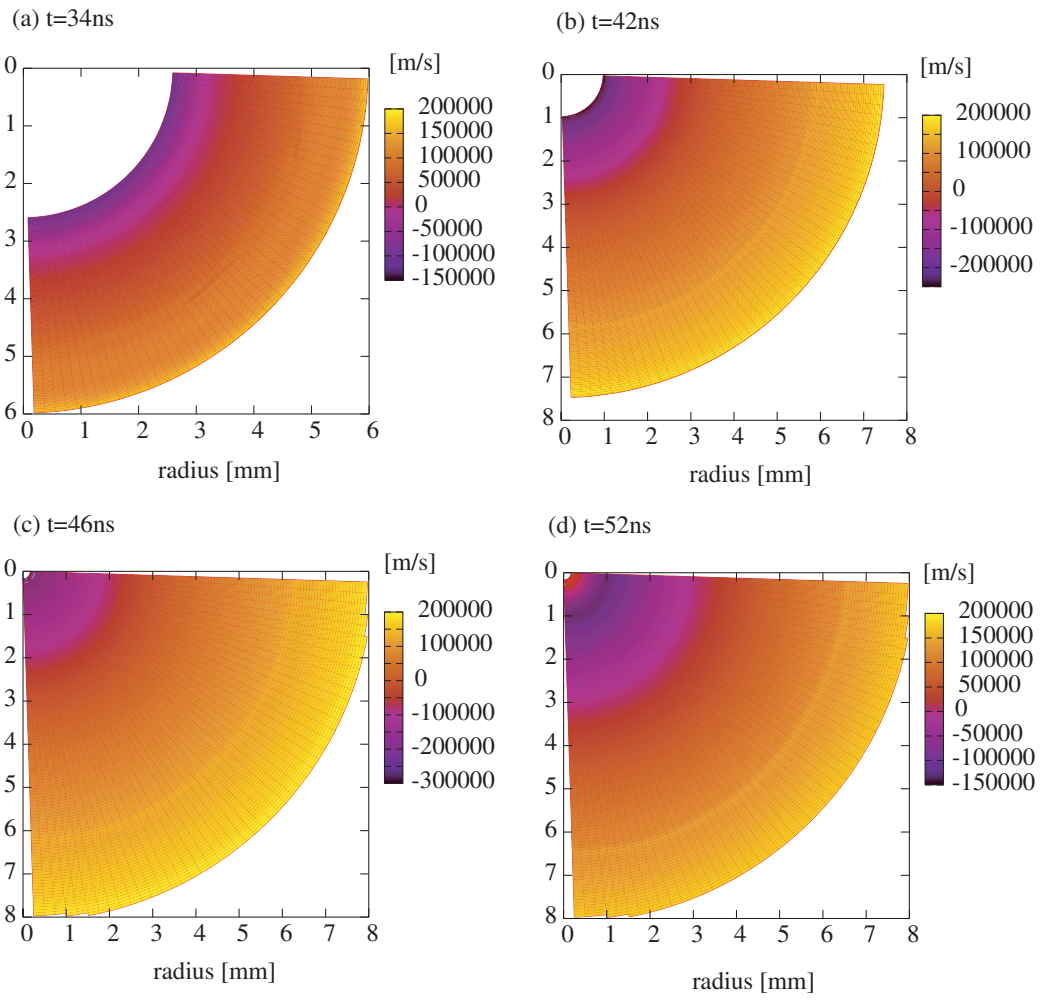

Figure 4.17: The radial velocity in the case of the 0.5 mm foam.

Figures 4.18 show the mean target density and the mean radiation temperature at (a) 0.29 nsec, (b) 40.4 nsec and (c) 44.6 nsec, respectively.

We can see that the HIB particle stop at the outside of foam layer. The heated Al layer produces the radiation energy. The radiation energy is confined in the foam layer, and smooth the HIB illumination non-uniformity. To check the radiation transport effect on the implosion non-uniformity smoothing, we compare the results for the cases with the radiation transport (ON) and without the radiation transport (OFF).

Figures 4.19 $\sim$ 4.21 show the target materials, the density and the total pressure at 0 nsec, 34 nsec, 42 nsec, 46 nsec and 52 nsec in the case of the radiation transport OFF, respectively. Figures 4.22 and 4.23 present the ion temperature and the radial velocity at 34 nsec, 42 nsec, 46 nsec and 52 nsec in the case of the radiation transport OFF, respectively.

From Figs. 4.19 $\sim$ 4.17, we can confirm that the more uniform implosion is done compared with the case of the radiation transport OFF (see also Fig. 4.24).

Especially, the fuel DT is compressed uniformly near the void close in the case of the radiation transport ON.

Figures 4.25 (a), (b) and (c) show the deposition energy due to the stopping power at (a) 20 nsec, (b) 24 nsec and (c) 34 nsec, respectively. Figures 4.25 (d), (e) and (f) show the target ion temperature for the cases of the radiation transport OFF ((d), (e) and (f)) and the radiation transport ON ((g), (h) and (i)) at 20 nsec, 24 nsec and 34 nsec. The time of 20 nsec, 24 nsec and 34 nsec are the end of the foot pulse, start of the main pulse and end of the pulse duration, respectively. From Fig. 4.25, we can see the implosion non-uniformity is suppressed from the main pulse by the radiation transport effect.

To confirm the radiation transport effect on the implosion non-uniformity smoothing, we pick up the radiation temperature profiles at 34 nsec and 42 nsec as a function of the θ angle in the cases of the 0.5 mm foam (radiation transport ON and OFF) and without the foam (see Fig. 4.26). The radiation temperature large non-uniformity in the θ direction can be seen in the case of the radiation transport OFF and the case without the foam. On the other hand, the raidation non-uniformity becomes smaller in the case of the radiation transport ON compared with the case of OFF. From above results, we can also confirm that the non-uniformity is smoothed by the radiation transport effect.

Figure 4.27 present the time dependence of the RMS non-uniformity of

the radiation temperature at the ablation front in the cases of the radiation transport ON and OFF. From Fig. 4.27, we can see that the implosion non-uniformity at the ablation front becomes small effectively by the main pulse in the case of the radiation transport ON. The foam layer is compressed gradually during the main pulse. During the main pulse and the compression of the foam layer, the implosion non-uniformity can be smoothed by the radiation transport effect.

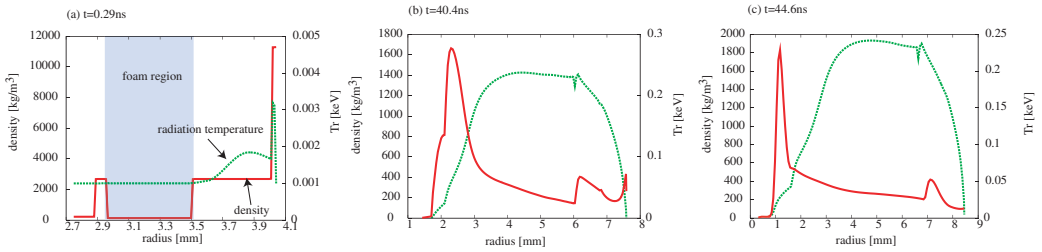

Figure 4.18: The mean density and the mean radiation temperature averaged for the θ direction at (a) 0.29 nsec, (b) 40.4 nsec and (c) 44.6 nsec in the case of the 0.5 mm foam, respectively.

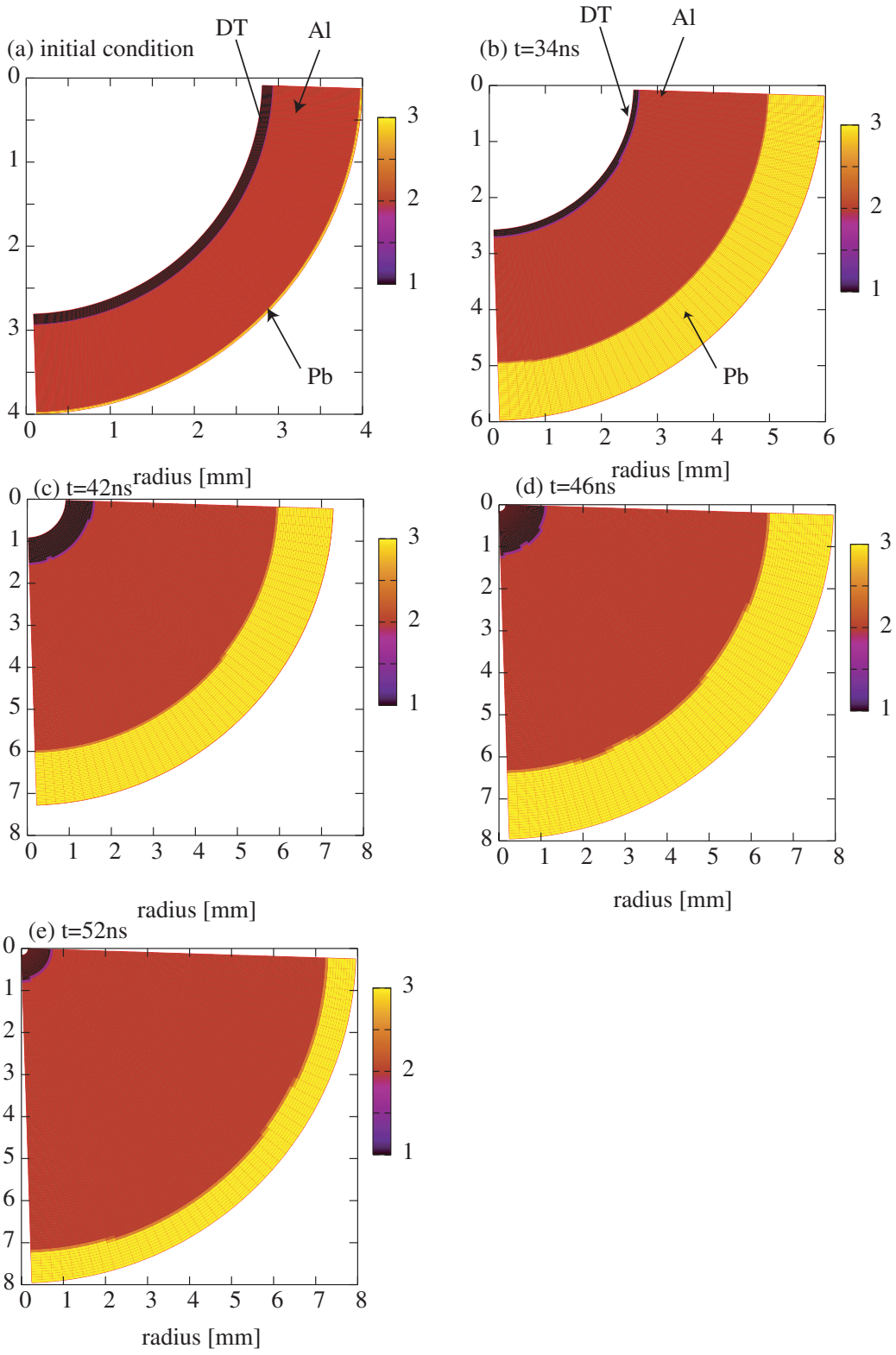

Figure 4.19: The target materials in the case of the 0.5mm foam (radiation transport OFF). The value of 1, 2, and 3 present the DT fuel, Al pusher and Pb tamper, respectively.

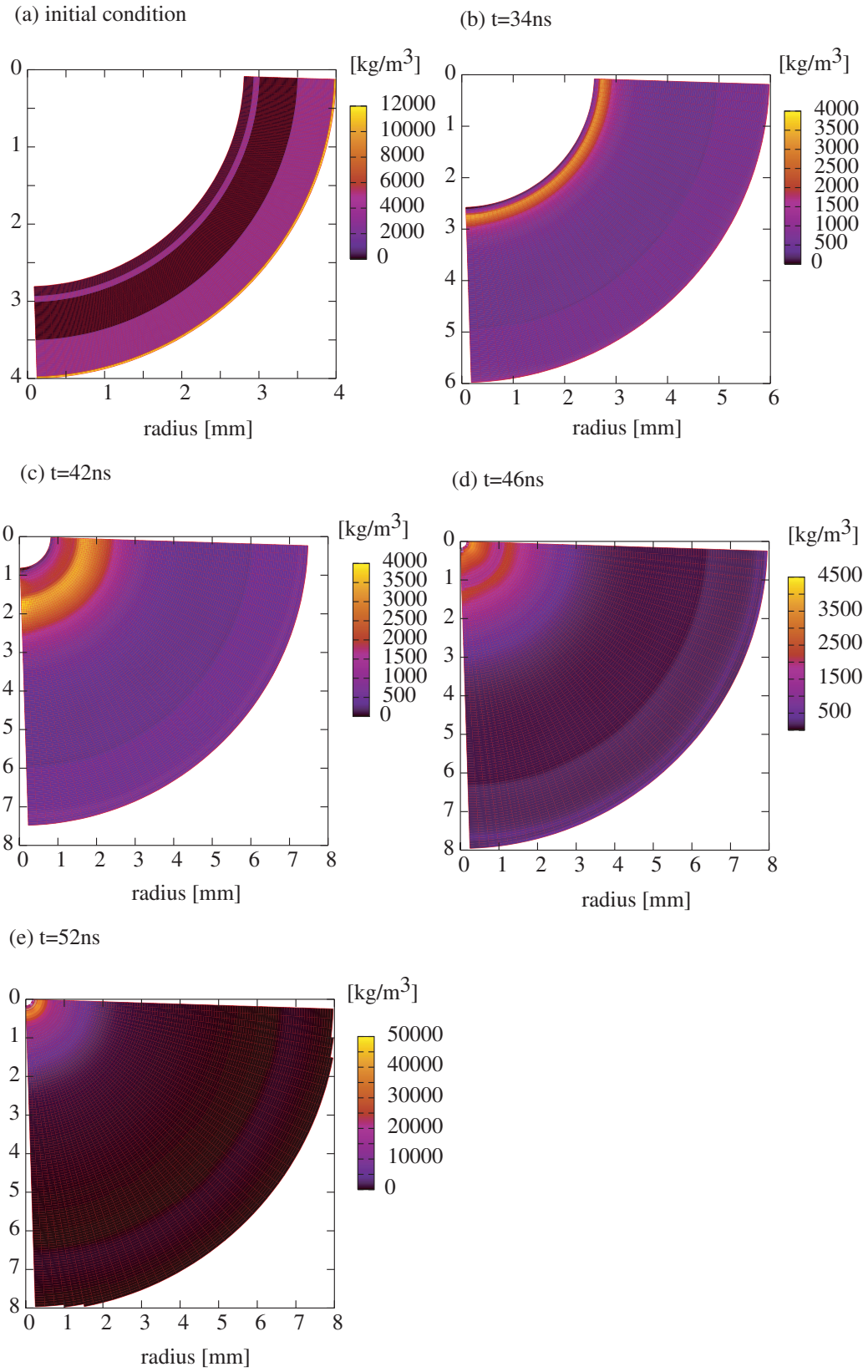

Figure 4.20: The target density profile in the case of the 0.5 mm foam (radiation transport OFF).

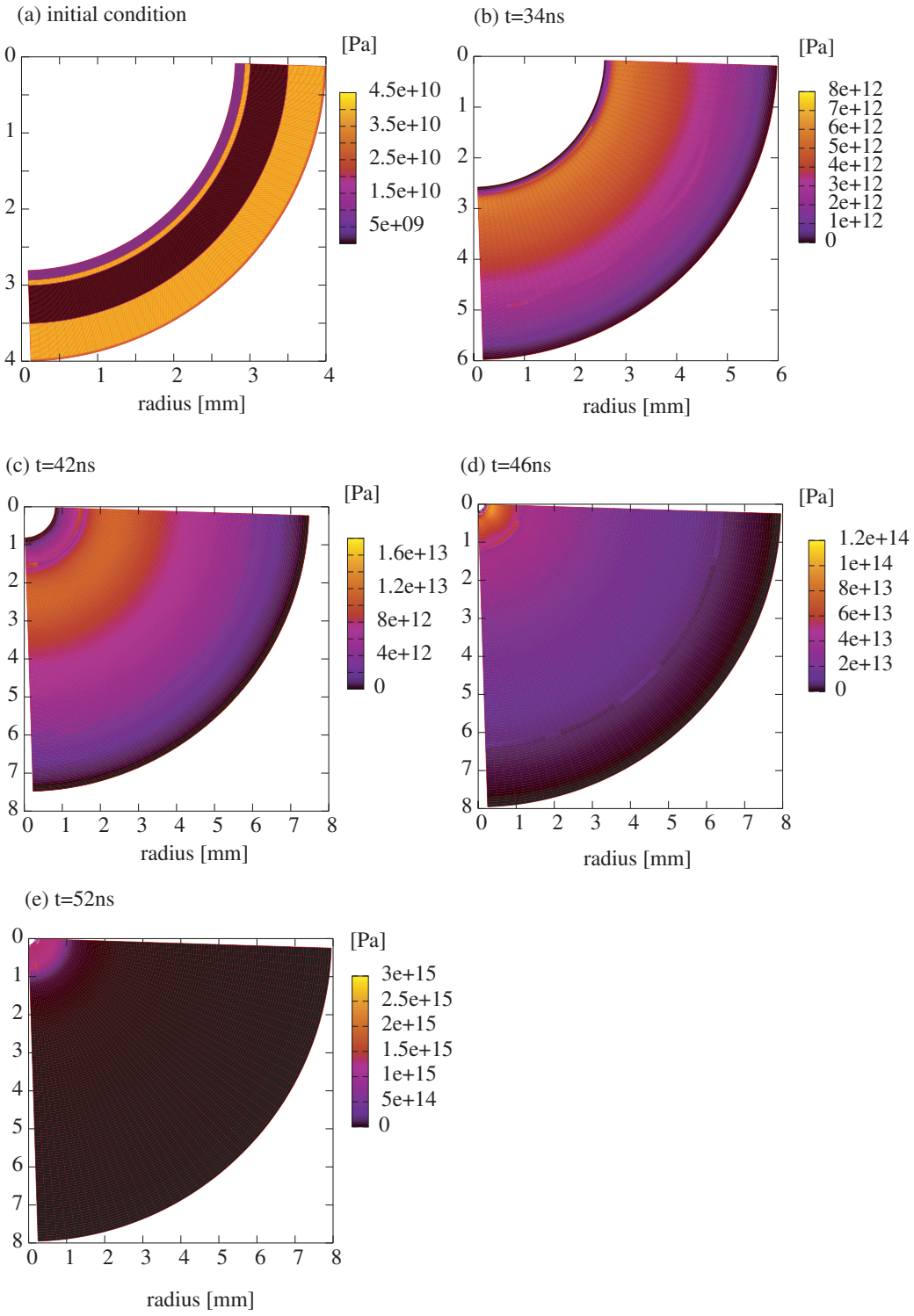

Figure 4.21: The target pressure in the case of the 0.5 mm foam (radiation transport OFF).

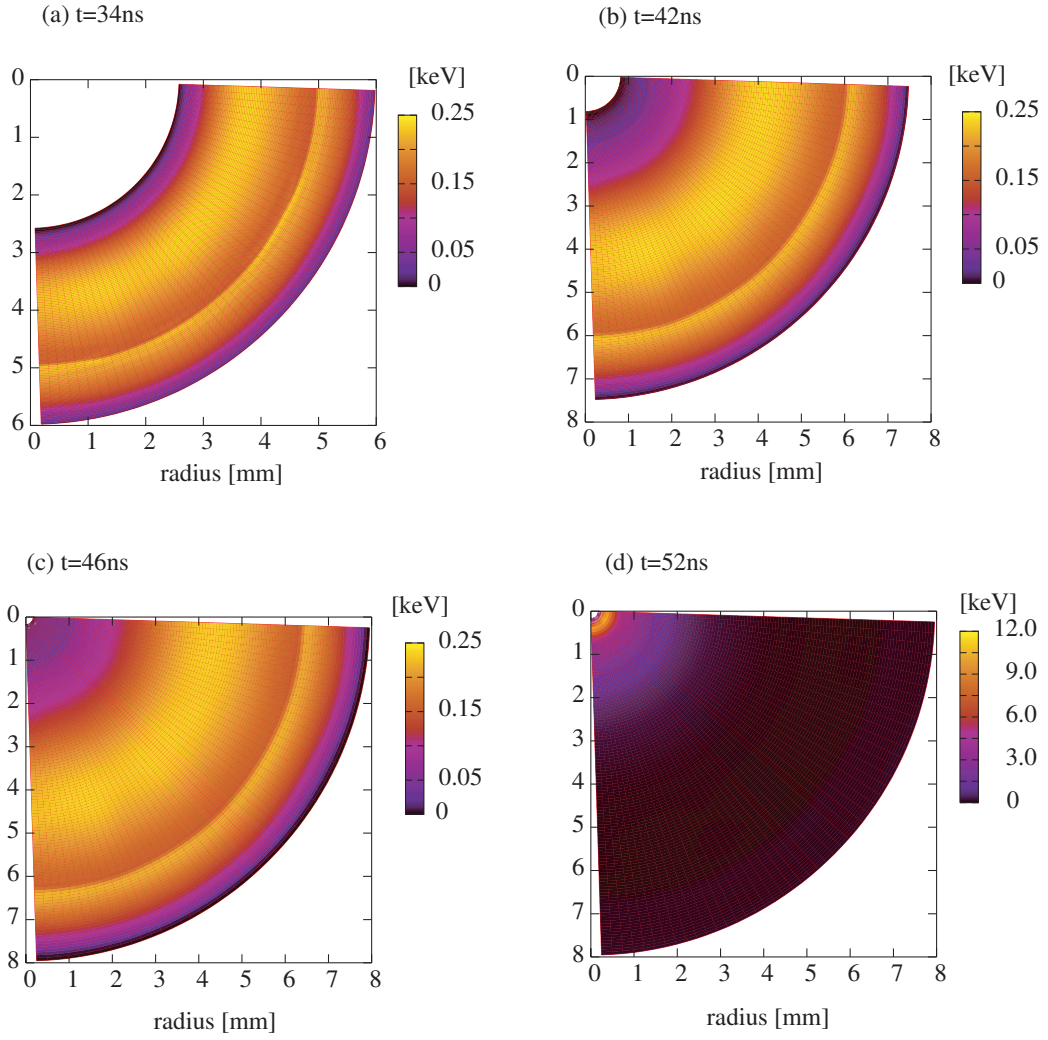

Figure 4.22: The target ion temperature in the case of the 0.5 mm foam (radiation transport OFF).

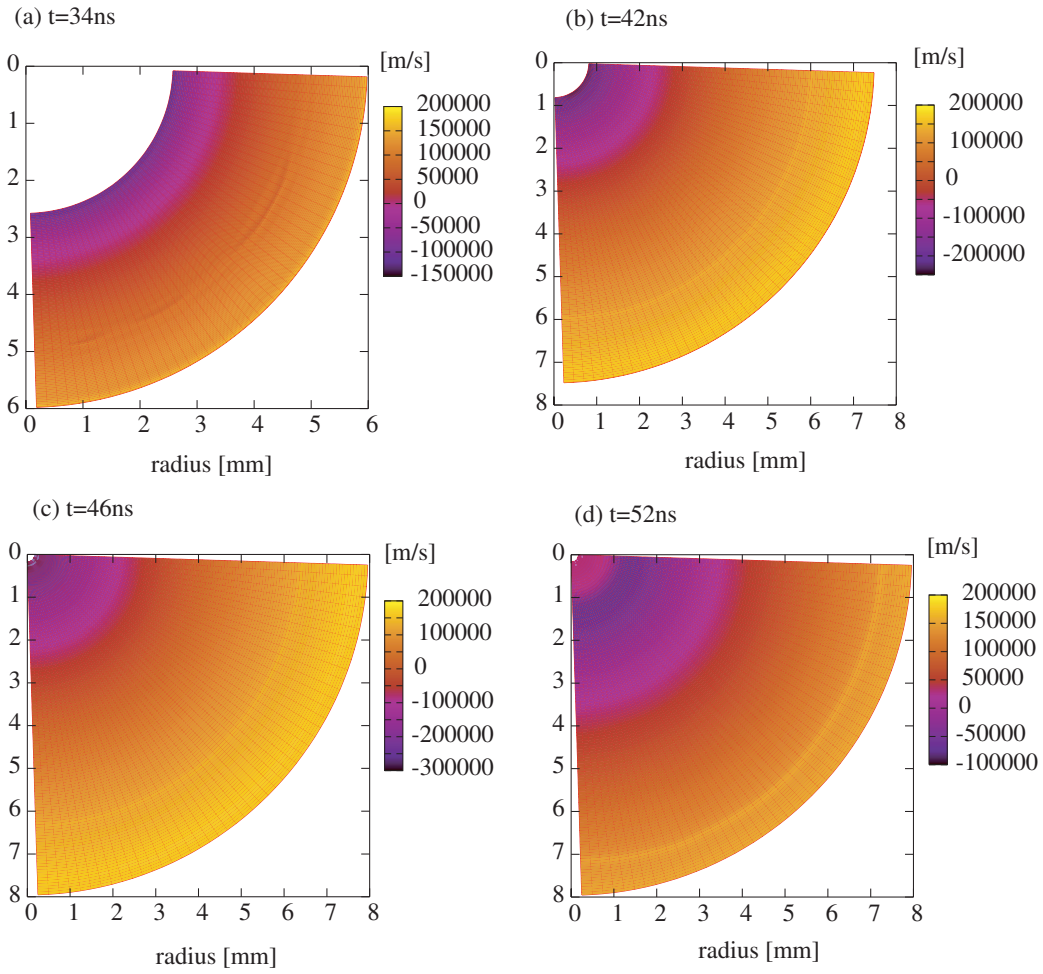

Figure 4.23: The radial velocity in the case of the 0.5 mm foam (radiation transport OFF).

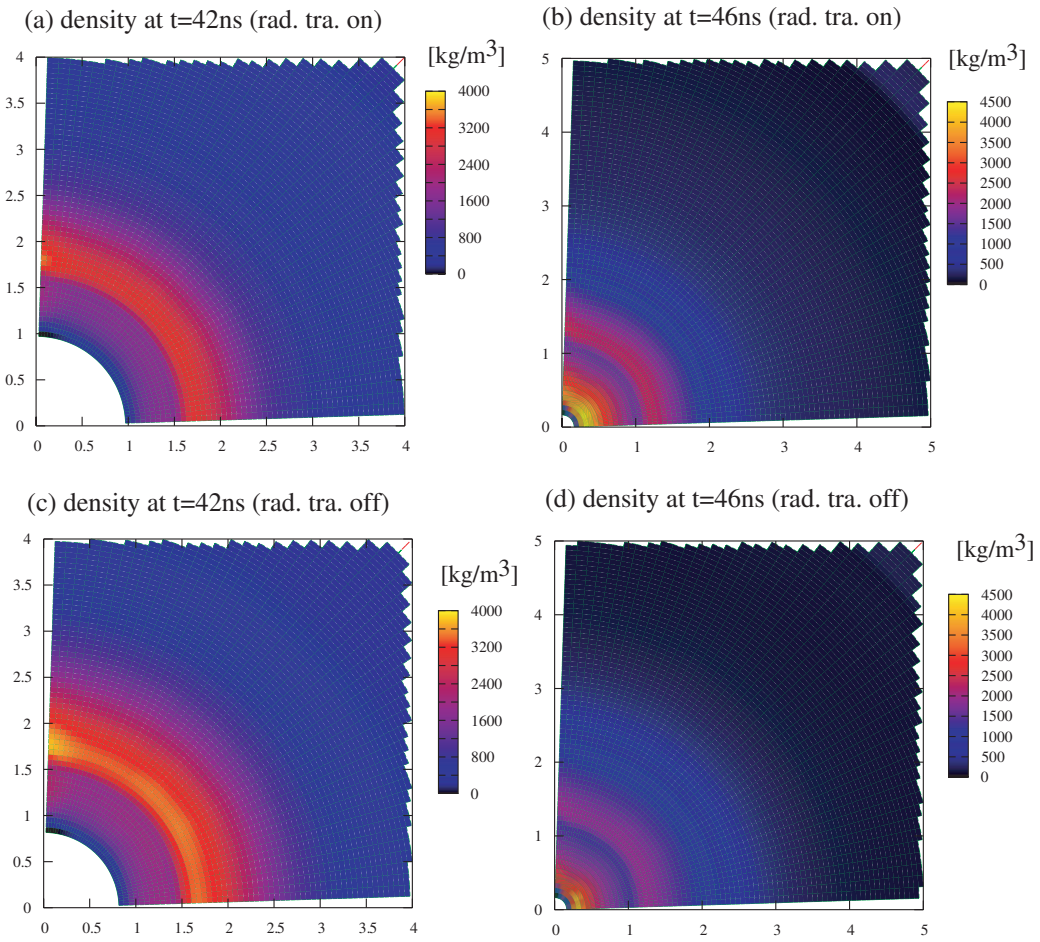

Figure 4.24: The focused target density profile in the case of the 0.5 mm foam at the (a) 42 nsec and (b) 46 nsec (radiation transport ON). Figure (c) and (d) present the radiation transport OFF case at the 42 nsec and 46 nsec, respectively.

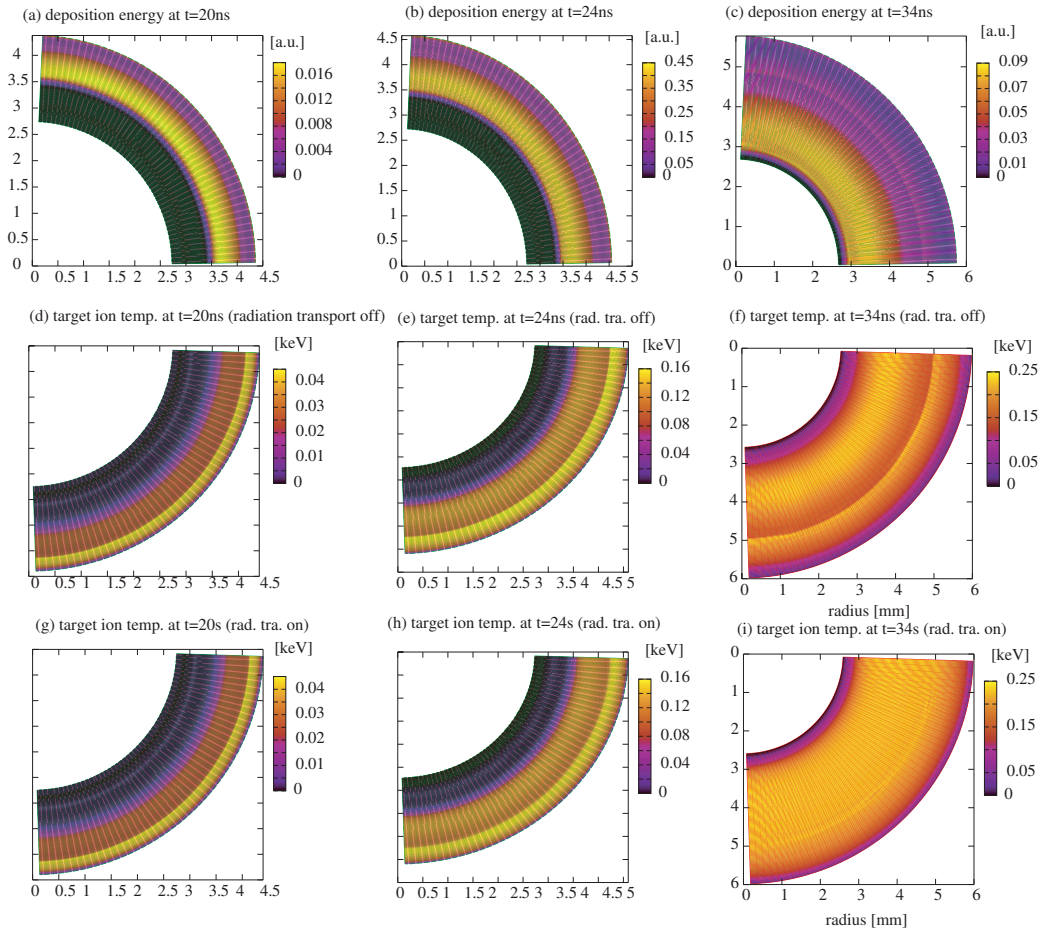

Figure 4.25: Figures (a), (b) and (c) present the deposition energy due to the stopping power at the 20 nsec, 24 nsec and 34 nsec, respectively. Figures (d) $\sim$ (i) are the target ion temperature in the cases of the radiation transport ON ((d), (e) and (f)) and OFF ((g), (h) and (i)) at the 20 nsec, 24 nsec and 34 nsec, respectively.

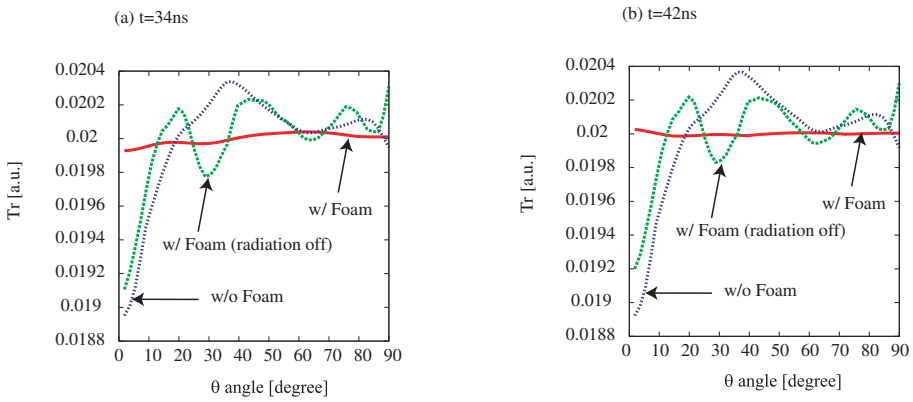

Figure 4.26: The radiation temperature v.s. θ angle at the (a) 34 nsec and (b) 42 nsec in the cases of the radiation transport ON, the radiation transport OFF and without the foam, respectively.

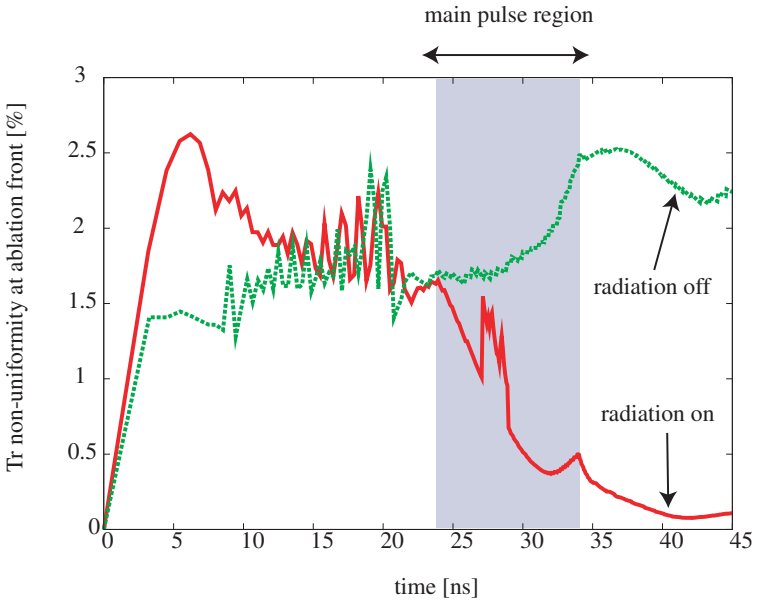

Figure 4.27: Time dependence of the RMS non-uniformity of the radiation temperature at the ablation front in the cases of radiation transport ON and OFF

Figure 4.28 present (a) the gain curve, (b) the mean ρR and (c) the maximum ion temperature in the cases radiation transport ON, OFF and without the foam, respectively. From Fig. 4.28, we can confirm that the pellet gain in the case with the foam is larger than 30 up to dz of about 300 μm pellet displacement. However, the gain becomes smaller with the increase in the pellet displacement in the cases of the radiation transport OFF and without the foam. The maximum ion temperature and the mean ρR decrease for a large pellet displacement in the case of the radiation transport OFF. On the other hand, the mean ρR and the maximum ion temperature in the case of the radiation transport ON are still large compared with those in the cases of the radiation transport OFF and without the foam. From these results, the radiation transport effect at the the low density region plays an important role to release the effective power production by ICF. In ICF, the tolerable pellet displacement from the fusion reactor center was about 20 μm for direct-driven implosion and about 100 μm for indirect-driven implosion, respectively [11–13, 50]. From our results, allowable dz in the direct-indirect mixture drive mode in HIF is about 300 μm.

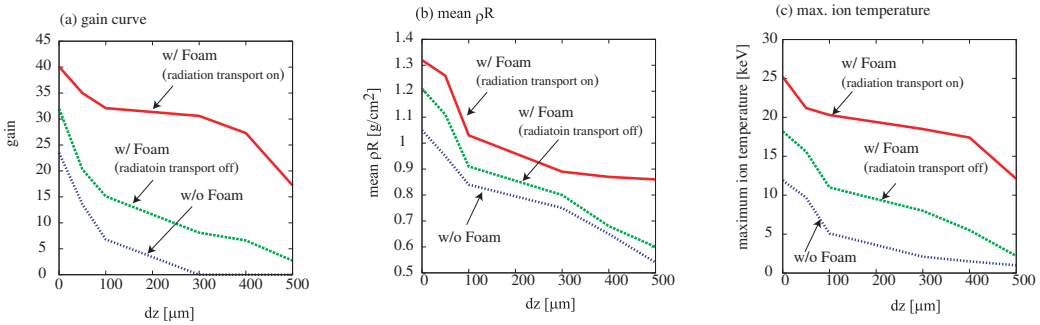

Figure 4.28: (a) The gain curve, (b) the mean ρR and (c) the maximum ion temperature in the cases of the radiation transport ON, OFF and without the foam.

Figures 4.29 and 4.30 show the implosion non-uniformity of (a) the target density, (b) the total pressure, (c) the ion temperature and (d) the radial velocity at the void closure time and maximum ρR time as a function of dz in the cases of the radiation transport ON, OFF and without the foam. From these figures, the implosion non-uniformity becomes large in the cases

of the radiation transport OFF and without the foam compared that with the radiation transport ON case. These results also indicate that the radiation transport effect at low density region can relax the non-uniform implosion. Especially at the maximum ρR, the non-uniformity is small compared with that at the void close time. This result shows that the effective fuel burning can be realized in spite of the large pellet displacement of dz $\sim$300 μm .

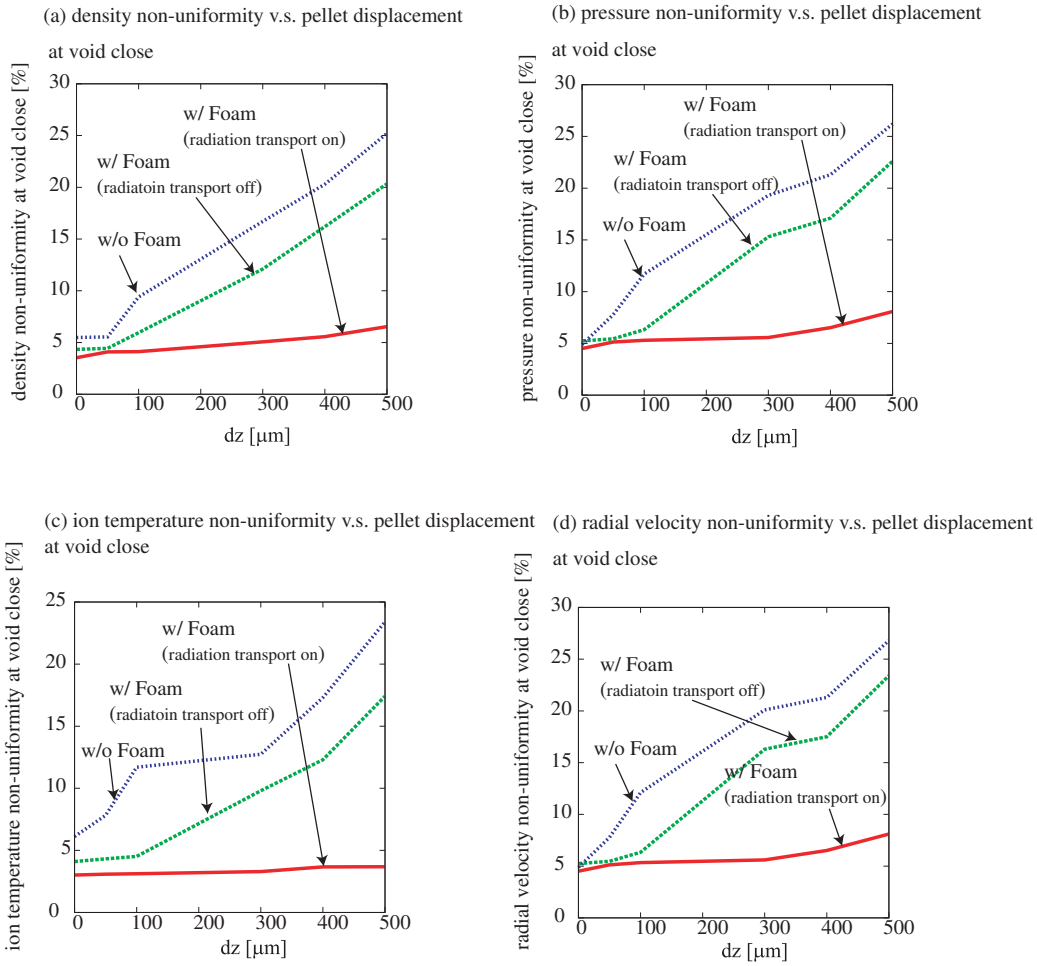

Figure 4.29: The non-uniformity of (a) the target density, (b) the total pressure, (c) the ion temperature and (d) the radial velocity at the void closure time as a function of dz in the cases of the radiation transport ON, OFF and without the foam.

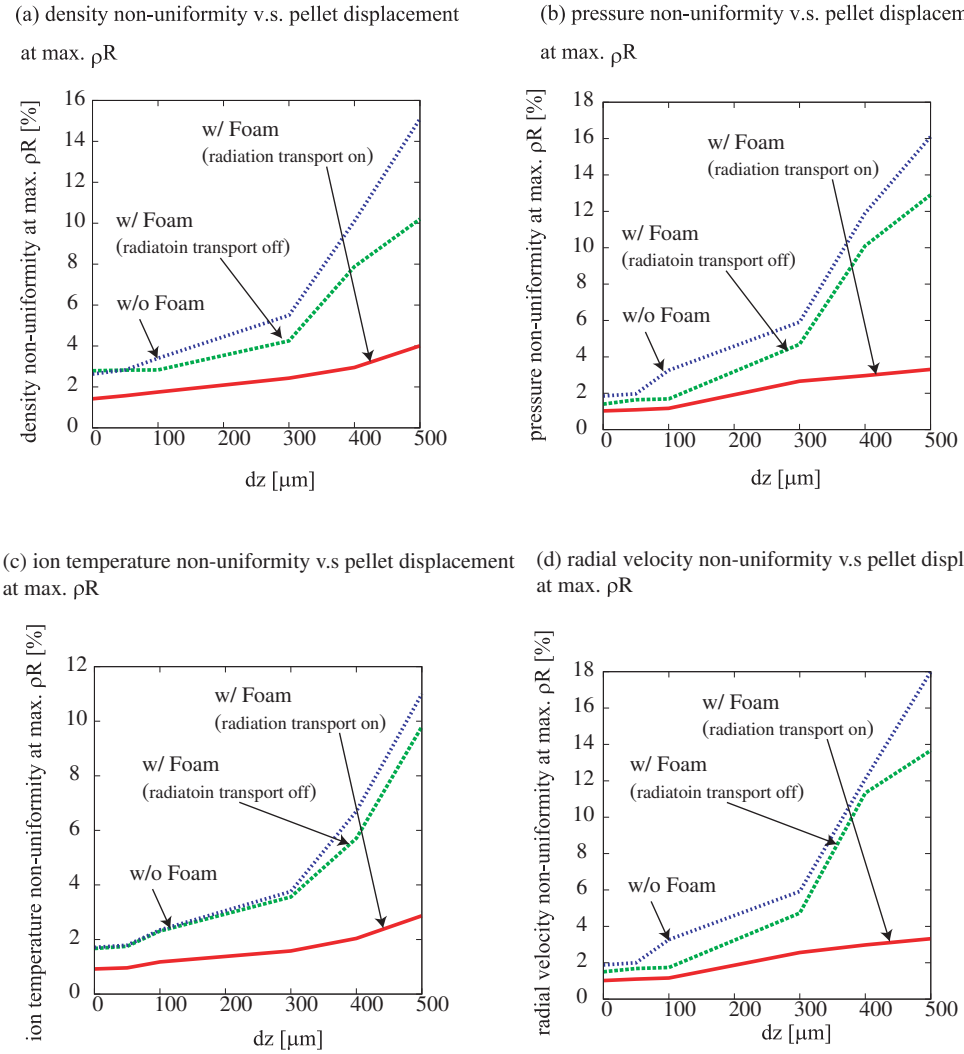

Figure 4.30: The non-uniformity of (a) the target density, (b) the total pressure, (c) the ion temperature and (d) the radial velocity at the time of maximum ρR time as a function of dz in the cases of the radiation transport ON, OFF and without the foam.

4.3.3 Effect of foam thickness

In this section, the effect of foam thickness on the direct-indirect mixture implosion is presented. We employ the target including the 1.0 mm thickness foam as shown in Fig. 4.2(c).

Figure 4.31 presents the mean target density and the radiation temperature in the case of the 1.0 mm thickness foam at (a) 0.50 nsec, (b) 43.6 nsec and (c) 47.3 nsec, respectively.

The deposition energy is distributed at the Pb layer as a tamper and at the ablation Al layer in the case of the 1.0 mm thickness foam (see Fig. 4.31 (a)).

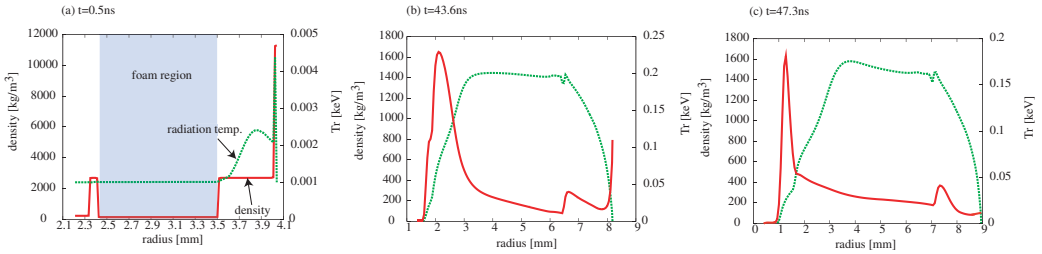

Figure 4.31: The mean density and the mean radiation temperature in the case of the 1.0 mm foam v.s target radius at the (a) 0.50 nsec, (b) 43.6 nsec, and (c) 47.3 nsec, respectively.

Figure 4.32 presents the radiation temperature at the ablation front as a function of θ angle at the (a) 34 nsec and (b) 42 nsec in the cases of 1.0 mm and 0.5 mm foams, respectively.

The radiation non-uniformity in the case of the 1.0 mm foam is almost same in the case of the 0.5 mm foam.

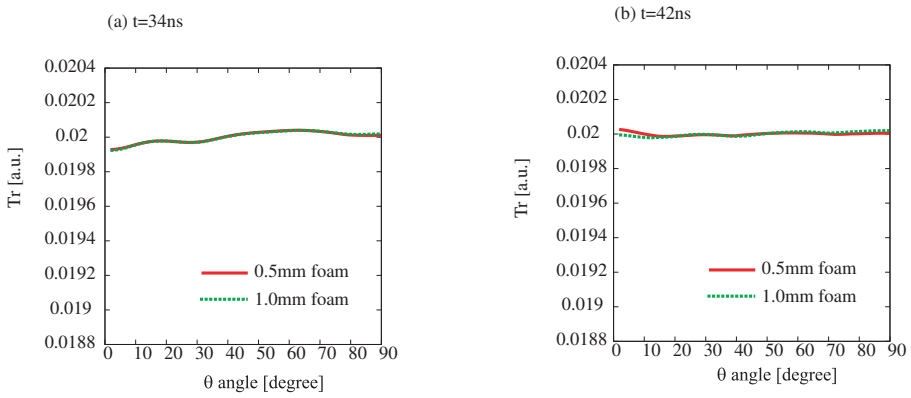

Figure 4.32: The radiation temperature v.s. θ angle at the (a) 34 nsec and (b) 42 nsec, respectively.

Figure 4.33 shows the time dependence of the RMS non-uniformity of the radiation temperature at the ablation front in the cases of 1.0 mm and 0.5 mm foams. From Fig. 4.33, we can see that the radiation temperature non-uniformity at the ablation front becomes small effectively at the main pulse region in both the cases.

Figure 4.34 presents the time dependence of radiation energy confined at the low density region in the cases of the 1.0 mm foam, the 0.5 mm foam and without the foam. The radiation energy is increased from the main pulse. The conversion efficiencies of the HIB total energy to the radiation energy are $\sim$ 4.5 % for the 1.0 mm foam, $\sim$ 4.5 % for the 0.5 mm foam and $\sim$ 1.5 % for without the foam. From these results, we find that the implosion mode in the case with the foam is a mixture of direct- and indirect- driven modes.

Figure 4.35 show (a) the gain curve, (b) the mean ρR and (c) the maximum ion temperature in the cases of 1.0 mm and 0.5 mm foams, respectively.

We can see that the required pellet gain is satisfied in the cases of 1.0 mm and 0.5 mm foams for the displacement of dz=0. However, the pellet gain is

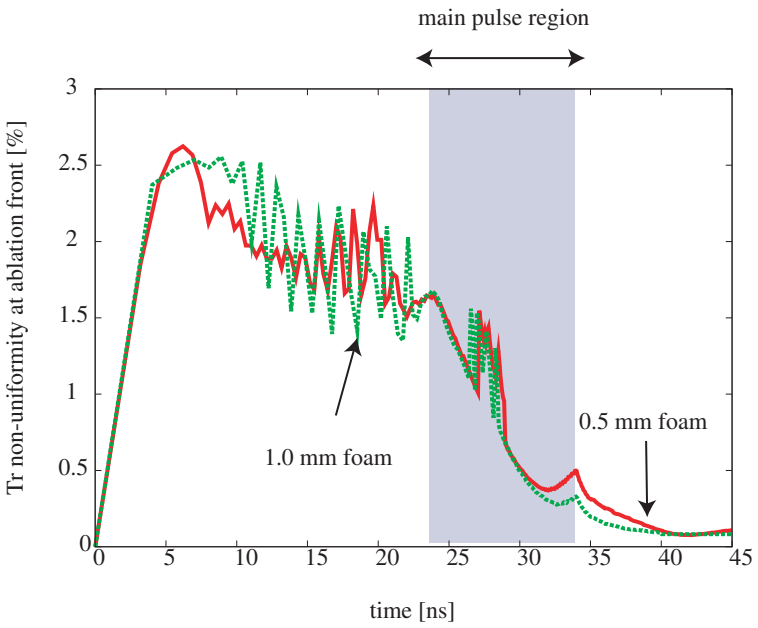

Figure 4.33: Time dependence of the RMS non-uniformity of the radiation temperature at the ablation front in the cases of 1.0 mm and 0.5 mm foams.

small in the case of the 1.0 mm foam compared wth that in the case of the 0.5 mm foam. The implosion velocity is not enough high to ignite the DT fuel efficiently because the 1.0 mm foam thickness was too thick to create a sufficient implosion driving pressure. Therefore, the pellet gain decreases for the large pellet displacement in the case of the 1.0 mm foam.

Figures 4.36 and 4.37 show the implosion non-uniformity of (a) the target density, (b) the total pressure, (c) the ion temperature and (d) the radial velocity at the void closure time and maximum ρR time as a function of dz in the cases of the 1.0 mm foam, the 0.5 mm foam and without the foam.

The implosion non-uniformity in the case without the foam becomes large for the large pellet displacement. In the case of the 1.0 mm foam, the non-uniformity is also small. However, the pellet gain is small compared with that in the 0.5 mm foam case as described above. These results indicate that the foam thickness is important to obtain a sufficient fusion energy output.

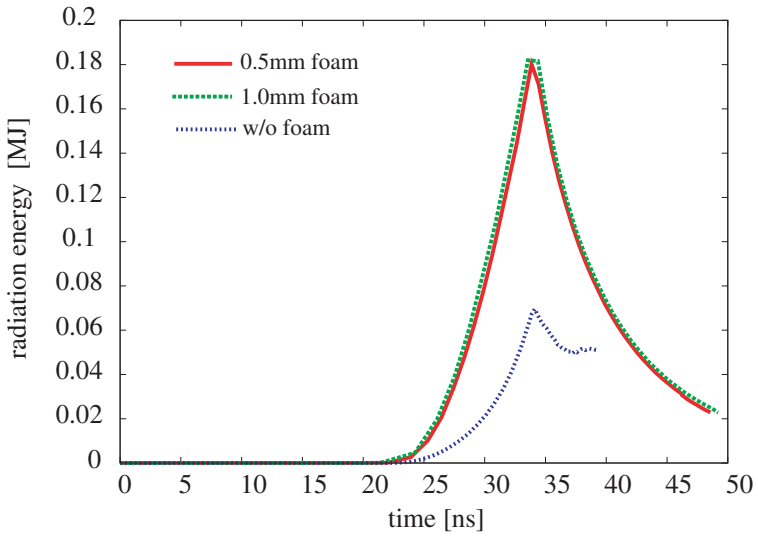

Figure 4.34: Time dependence of the confined radiation energy at the low density region in the cases of the 1.0 mm foam, the 0.5 mm foam and without the foam.

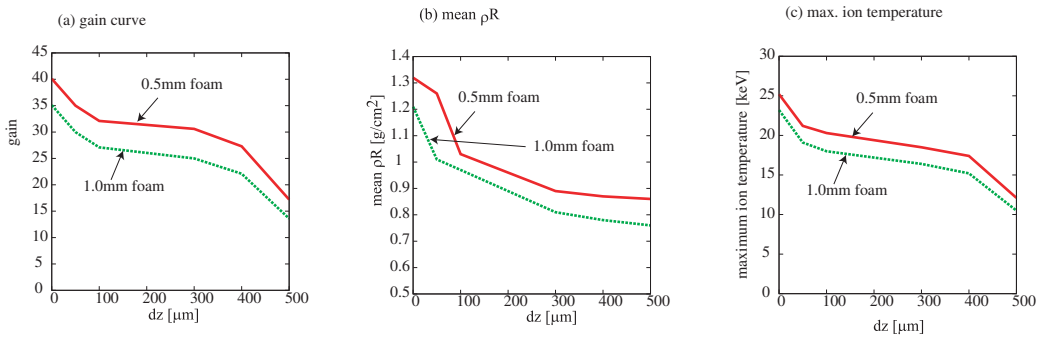

Figure 4.35: (a) The gain curve, (b) the mean ρR and (c) the maximum ion temperature in the cases 1.0 mm and 0.5 mm foams.

(a) density non-uniformity v.s. pellet displacement at void close

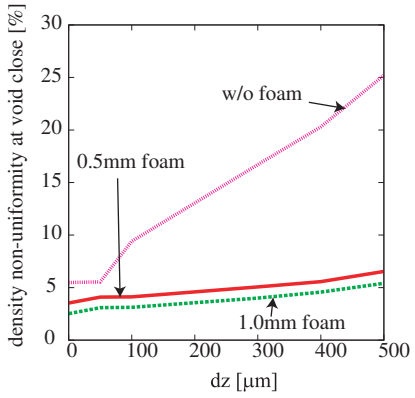

(b) pressure non-uniformity v.s. pellet displacement at void close

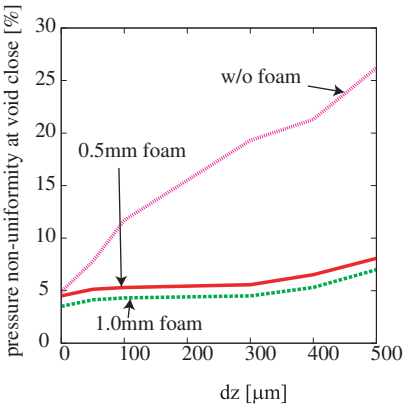

(c) ion temperature non-uniformity v.s. pellet displacement at void close

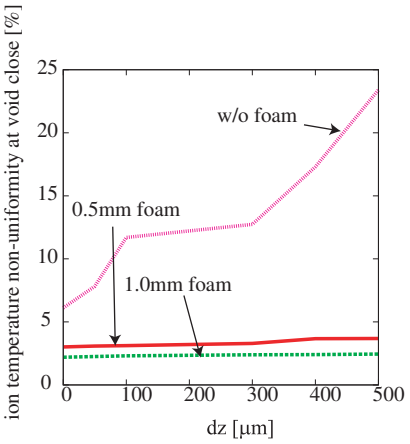

(d) radial velocity non-uniformity v.s. pellet displacement at void close

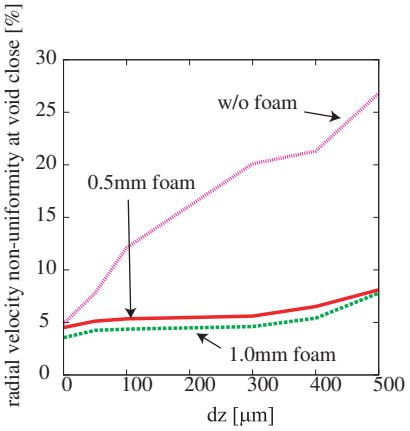

Figure 4.36: The non-uniformity of (a) the target density, (b) the total pressure, (c) the ion temperature and (d) the radial velocity at the void closure time as a function of dz in the cases of the 1.0 mm foam, the 0.5 mm foam and without the foam.

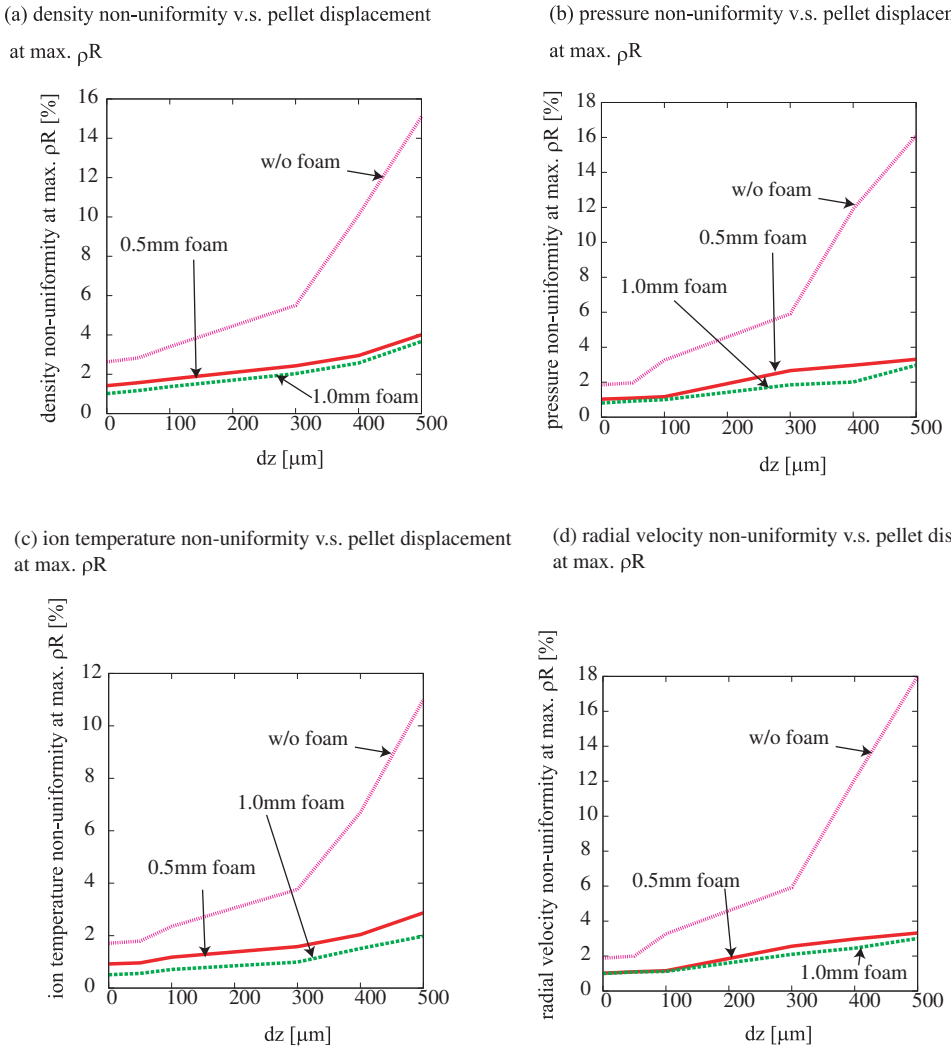

Figure 4.37: The non-uniformity of (a) the target density, (b) the total pressure, (c) the ion temperature and (d) the radial velocity at the time of maximum ρR time as a function of dz in the cases of the 1.0 mm foam, the 0.5 mm foam and without the foam.

4.4 Discussions

In this chapter, we discuss the target implosion using the 32-HIBs illumination system. The direct-driven fuel target implosion is weak against the beam non-uniformity. However, in the low density foam region, the radiation energy can be confined and the implosion non-uniformity is smoothed. Therefore, we employ the foam layer for the fuel target in order to increase the radiation energy confined and to expect a uniform target implosion. In our target with the foam, the direct-indirect mixture implosion mode is realized. From our calculation results, the trapped radiation energy at the low density region in the case with the foam (direct-indirect mixture mode) is large compared with that in the case without the foam (direct-driven mode). The peak conversion efficiencies are ~ 4.5 % in the case of the 1.0 mm foam, ~ 4.5 % in the case of the 0.5 mm foam and ~ 1.5 % in the case without the foam. The foam thickness is important to release sufficient fusion energy. For the 0.5 mm thickness foam case, the implosion non-uniformity is suppressed effectively and sufficient fusion energy is obtained in HIF. It was also found that the direct-indirect mode target is robust against the target displacement of dz. In the direct-indirect mixture mode, the allowable displacement was dz of ~ 300 μm.

Chapter 5

Conclusions

To solve the energy problem, we set out to achieve the energy production system by HIF as mentioned in Chapter 1. The HIF has several problems. In this study, we focus on these problems of HIF as follows:

- HIB final transport
- HIB-target interaction
- Target hydrodynamics, fuel ignition and energy gain

In Chapter 2, we proposed the insulator beam guide for the focusing heavy ion beam neutralization. Plasma electrons are emitted from the plasma generated on the insulator inner surface. The electrons move with the heavy ion beam, and the beam space charge is neutralized effectively by the electrons. By the PIC simulation, it is confirmed that the heavy ion beam propagates efficiently and is focused well through the insulator beam guide, which may be made of one kind of ceramics and may absorb a part of reactor gas leaked to a beam port. We also confirm that the heavy ion beam is kept in a high quality and an emittance growth is suppressed through the insulator guide. We also presented the HIB stability analyses. We estimate the stability boundary for a focusing HIB propagating without an influence of the two-stream instability. The focusing HIB is also safe from the filamentation instability. Therefore the results shown in this paper presented that the HIB ions are focused successfully onto a fuel pellet located at a reactor center without severe influences of instabilities.

In Chapter 3, we studied the HIB deposition non-uniformity in a direct-driven HIB-ICF pellet. For various beam parameters and different reactor chamber radii we investigated the energy deposition non-uniformity using 12, 20, 32, 60, 92 and 120-beam irradiation systems. The HIB diverges slightly by the beam temperature. We include the effect of a beam longitudinal temperature and the beam transverse emittance. In our simulation results we confirm that the HIB illumination non-uniformity is 1.52 % in the case of the Al mono-layer structure target, the beam temperature of 100MeV, the 120-beam system, and the semi-Gaussian particle density distribution. In the case of the Pb+Al target structure, 1.72 %. On the other hand, the RMS non-uniformity using the Gaussian beam including the beam temperature is close to the non-uniformity for the semi-Gaussian distribution with the temperature effect (1.49 % for Al layer, 1.60 % for Pb+Al layer). From these results, we expect that the fuel can be successfully imploded and the fusion energy can be released from a direct-driven fuel pellet in HIB ICF using the Gaussian or semi-Gaussian HIBs. Moreover we analyzed the spectrum of the HIB illumination non-uniformity in the spherical target. As a result, the deposition energy non-uniformity in the target includes higher modes with sufficiently low amplitudes. Therefore the mode analyses also demonstrate that by using an appropriate illumination pattern and the selected HIB illumination parameter values the sufficiently low non-uniformity can be realized. From the relationship between the chamber radius and the HIB illumination non-uniformity in the cases of 32, 60, and 120-beam systems, with the beam temperature and the semi-Gaussian distribution particle number density, the RMS non-uniformity does not change much with the change in the reactor chamber radius as shown in Fig. 3.9 at a realistic chamber radius R_{ch} of about $3 \sim 6$ m. In this parameter range of R_{ch} we can expect that the HIB illumination non-uniformity is suppressed less than a few %. We also demonstrated the important effect of the HIB transverse emittance in Fig. 3.10. The results show that the beam transverse emittance should be sufficiently low and that the reactor chamber radius should be optimized. In HIB ICF, the target temperature increases during the HIB pulse duration. Therefore we also calculated the relationship between the target temperature and the HIB illumination non-uniformity. We found that even if the target temperature increases in a typical temperature range in HIB ICF, the RMS non-uniformity does not change much. This result presents that the RMS non-uniformity is kept low during the HIB pulse illumination onto a direct-driven pellet in ICF. Moreover we investigated the non-uniformity growth

due to the little pellet displacement of the pellet position from the chamber center. The calculation results demonstrated that the pellet displacement is a serious problem in HIF. We also estimate the effect of acceleration non-uniformity in radial direction. From this estimation, we expect that the effect of acceleration non-uniformity is not serious problem to archive an effective implosion.

In Chaper 4, we discuss the target implosion using the 32-HIBs illumination system. The direct-driven fuel target implosion is weak against the beam non-uniformity. However, in the low density foam region, the radiation energy can be confined and the implosion non-uniformity is smoothed. Therefore, we employ the foam layer for the fuel target in order to increase the radiation energy confined and to expect a uniform target implosion. In our target with the foam, the direct-indirect mixture implosion mode is realized. From our calculation results, the trapped radiation energy at the low density region in the case with the foam (direct-indirect mixture mode) is large compared with that in the case without the foam (direct-driven mode). The peak conversion efficiencies are ~ 4.5 % in the case of the 1.0 mm foam, ~ 4.5 % in the case of the 0.5 mm foam and ~ 1.5 % in the case without the foam. The foam thickness is important to release sufficient fusion energy. For the 0.5 mm thickness foam case, the implosion non-uniformity is suppressed effectively and sufficient fusion energy is obtained in HIF. It was also found that the direct-indirect mode target is robust against the target displacement of dz. Our simulation results present that a large pellet displacement of $\sim$ 300 μm is allowed in order to obtain sufficient fusion energy in HIF.

I wish to realize an electrical power generation by HIF with several results in this thesis. The solution of the energy problem is my earnest desire.

Acknowledgments

Firstly, I would like to acknowledge Professor Shigeo Kawata (Utsunomiya University) for his exact directions, accurate advices, and useful comments in my life as a student of doctoral program, not only in my studies. Professor Kawata could always indicate me the right way using his unbounded intelligence in physics, engineering, and general subjects. Without Professor Kawata, all of the results presented in this thesis would have been impossible to obtain.

I would like to thanks to Prof. Satoshi Ogasawara (Utusnomiya University) for his useful advises on this thesis.

I would like to thanks to Prof. Takeshi Nagasawa (Utusnomiya University) for his valuable advise on this thesis.

I would like to thanks to Prof. Mutsumasa Suzuki (Utusnomiya University) for his lecture of sub-major subject concerning to superconductor and useful comments for this thesis.

I would like to thanks to Prof. Noboru Yugami (Utusnomiya University) for his advise on my researches and useful comments.

I would like to express thanks to Prof. Kazuhiko Horioka (Tokyo Institute of Technology) for his supports of my researches and helpful advice on this thesis.

I also would like to thanks to Prof. Shunichi Nakai (Utusnomiya University) for his lecture of radiation energy as my sub-major subject.

I would like to express thanks to Dr. Takashi Kikuchi (Utsunomiya University) for his excellent advise on my researches and helpful support on this thesis.

Also, I would like to thank Dr. Takashi Nakamura (Tokyo Institute of Technology) for his special advices on numerical simulation techniques.

I would like to thank Dr. Aleksandar Ogoyski (Tech. Univ. Varna, Bulgaria) for his advices and comments about a beam illumination.

I would also like to present our thanks to colleagues in Japan and U.S. HIF VNL research groups for their fruitful discussions on this subject.

I would like to thank Mrs. Yumi Nakajima and Mrs. Shigeko Tezuka of her greatful desk works.

I would like to thanks to Kawata laboratory members (Mr. Shuji Miyazaki, Mr. Kei Sakai, Mr. Ryo Sonobe, Mr. Hideaki.Fujiu, Mr. Kentarou Miyazawa, Mr. Masahide Seino, Mr. Masaki Nakamura, Mr. Shoutarou Hasumi, Mr. Hideaki Sugiura, Mr. Yuichi Saiou, Mr. Yushihisa Akasaka, Mr. Yoshimasa Wakatsuki, Mr. Naoki Onuma, Mr. Hajime Nagano, Mr. Tetsuya Ozaki and Mr. Takahiro Watanabe), many seniors, juniors (Mr. Toru Sasaki in Tokyo Institute of Technology et al.), and compeer could help my campus life to be fruitful.

In addition, I would like to thank the Japan Scholarship Foundation for the great financial supports in my life as a postgraduate. Moreover, this work was partly supported by the JSPS (Japan Society for the Promotion of Science) and MEXT (Ministry of Education, Culture, Sports, Science and Technology).

At last but not least, I would like to thank my family for their supports throughout my life.

Finally, special thanks to my dear wife for her many supports.

References

[1] S.Atzeni and J.Meyer-ter-Vehn, "The physics of inertial fusion", Oxford University Press (2004).

[2] R.L. Kauffman, L.J.Suter, C.B.Darrow, J.D.Kilkenny, H.N.Kornblum, D.S.Montgomery, D.W.Phillion, M.D.Rosen, A.R.Theissen, R.J.Wallace and F.Ze, "High temperatures in inertial confinement fusion radiation cavities heated with 0.35 μm light", Phys. Rev. Lett. **73** 2320 (1994).

[3] M.Tabak and D.Callahan-Miller, "Design of a distributed radiator target for inertial fusion driven from two sides with heavy ion beams", Phys. Plasmas **5** 1895 (1998).

[4] M.Tabak and D.Callahan-Miller, D.D.-M.Ho and G.B.Zimmerman, "Design of distributed radiator target for inertial fusion driven from two sides with heavy ion beams", Nucl. Fusion **38** 509 (1998).

[5] D.A.Callahan, "Interaction between neighboring beams in heavy ion fusion reactor chamber", Appl. Phys. Lett. **67**, L3254 (1995).

[6] B.A.Hammel, C.J.Keane, M.D.Cable, D.R.Kania, J.D.Kilkenny, R.W Lee and R.Pasha, "X-ray spectroscopic measurements of high densities and temperatures from indirectly driven inertial confinement fusion capsules", Phys. Rev. Lett. **70** 1263 (1993).

[7] M.D.Cable, S.P.Hatchett, J.A.Caird, J.D.Kilkenny, H.N.Kornblum, S.M.Lane, C.Laumann, R.A Lerche, T.J.Murphy, J.Murray, M.B.Nelson, D.W.Phillion, H.Powell and D.B.Ress, "Indirectly driven, high convergence inertial confinement fusion implosions", Phys. Rev. Lett. **73** 2316 (1994).

[8] S.H.Glenzer, L.J.Suter, R.E.Turner, B.J.MacGowan, K.G.Estabrook, M.A.Blain, S.N.Dixit, B.A.Hammel, R.L.Kauffman, R.K.Kirkwood, O.L.Landen, M.-C.Monteil, J.D.Moody, T.J.Orzechowski, D.M.Pennington, G.F.Stone and T.L.Weiland, "Energetics of Inertial Confinement Fusion Hohlraum Plasmas", Phys. Rev. Lett. **80** 2845 (1998).

[9] T.Kikuchi, M.Nakajima and K.Horioka, "A quasi-equilibrium beam compression in a recirculator for heavy ion inertial fusion", Phys. Plasmas **9**, 3476 (2002).

[10] T.Someya, A.I.Ogoyski, S.Kawata and T.Sasaki, "Heavy-ion beam illumination on a direct-driven pellet in heavy-ion inertial fusioin", Phys. Rev. ST-AB **7** 044701 (2004).

[11] P.W.Petzoldt, N.B.Alexander, T.J.Drake, D.T.Goodin, K.Jonestrask and R.W.Stemke, "Experimental target injection and tracking system", Fusion Sci. Tech. **44** 138 (2003).

[12] P.W.Petzoldt, M.Cherry, N.B.Alexander and D.T.Goodin, "Design of an inertial fusion energy target tracking and position prediction system", Fusion Sci. Tech. **39** 678 (2001).

[13] D.T.Goodin, N.B.Alexander, C.R.Gibson, A.Nobile, R.W.Petzoldt, N.P.Siegel and L.Thompson, "Developing target injection and tracking for inertial fusion energy power plants", Nuclear Fusion **41** 527 (2001).

[14] C.L.Olson, "Chamber transport", Nucl. Inst. Meth. Phys. Res. A **464** 118 (2001).

[15] R.B.Miller, "Intense charged particle beams", Plenum Press, New York (1985).

[16] S.Humphries, Jr., "Charged particle beams", John Wiley and Sons, Inc. (1990).

[17] C.Deutsch, S.Kawata and T.Nakamura, "Accelerator system and final beam transport in heavy ion inertial confinement fusion", J.Plasma Fusion Res. **77** 441 (1996).

[18] S.Hanamori, S.Kawata, S.Kato, T.Kikuchi, A.Fujita, Y.Chiba and T.Hikita, "Intense-Proton-Beam transport through an insulator beam guide", Jpn. J. Appl. Phys. **37** L471 (1998).

[19] E.S.Weibel, "Spontaneously growing transverse waves in a plasma due to an anisotropic velocity distribution", Phys. Rev. Lett. **2** 83 (1959).

[20] H.C.Miller, "Surface flashover of insulators", IEEE Trans. Electr. Insul. **24** 765 (1989).

[21] NRL Plasma Formulary, (2000).

[22] T.Okada and K.Niu, "Filamentation and two-stream instabilities of light ion beams in fusion target chambers", J. Phys. Soc. Jnp. **50** 3845 (1981).

[23] T.Okada and K.Niu, "Electromagnetic instability and stopping power of plasma for relativistic electron beams", J. Plasma Phys. **23** 423 (1980).

[24] T.Okada and K.Niu, "Effect of collision on the relativistic electromagnetic instability", J. Plasma Phys. **24** 483 (1980).

[25] R.F.Hubbard and D.A.Tidman, "Filamentation instability of ion beams focused in pellet-fusion reactors", Phys. Rev. Lett. **41** 866 (1978).

[26] P.F.Ottinger, D.Mosher and S.A.Goldstein, "Microstability of a focused ion beam propagating through a z-pinch plasma", Phys. Fluids **22** 332 (1979).

[27] J.D.Lindl, R.L.McCrory and E.M.Campbell, "Progress toward ignition and burn propagation in inertial confinement fusion", Phys. Today **45** 32 (1992).

[28] W.J.Hogan, R.Bangerter and G.L.Kulcinski, "Energy from inertial fusion", Phys. Today **42** 42 (1992).

[29] J.Sasaki, T.Nakamura, Y.Uchida, T.Someya, K.Shimizu, M.Shitamura, T.Teramoto, A.B.Blagoev and S.Kawata, "Beam non-uniformity smoothing using density valley formed by heavy ion beam deposition in inertial confinement fusion fuel pellt", Jpn. J. Appl. Phys. **40** 968 (2001).

[30] D.R.Welch, D.V.Rose, B.V.Oliver, T.C.Genoni, R.E.Clark, C.L.Olson and S.S.Yu, "Simulation of intense heavy ion beams propagating through a gaseous fusion target chamber", Phys. Plasmas **9** 2344 (2002).

[31] T.Someya, S.Kawata, T.Nakamura, A.I.Ogoyski, K.Shimizu and J.Sasaki, "Beam final transport and direct-drive pellet implosion in heavy-ion fusion", Fusion Sci. Tech. **43** 282 (2003).

[32] W.M.Sharp, D.A.Callahan M.Tabak, S.S.Yu, P.F.Peterson, D.T.Welch, D.V.Rose and C.L.Olson, "Modeling chamber transport for heavy-ion fusion", Fusion Sci. Tech. **43** 393 (2003).

[33] M.Murakami, "Irradiation system based on dodecahedron for inertial confinement fusion", Appl. Phys. Lett. **66** 1587 (1995).

[34] M.Murakami, K.Nishihara and H.Azechi, "Irradiation nonuniformity due to imperfections of laser beams", J. Appl. Phys. **74** 802 (1993).

[35] S.Skupsky and K.Lee, "Uniformity of energy deposition for laser driven fusion", J. Appl. Phys. **54** 3662 (1983).

[36] S.Kawata and K.Niu, "Effect of nonuniform implosion of target on fusion parameters", J. Phys. Soc. Jpn. **53**, 3416 (1984).

[37] M.H.Emery, J.H.Orens, J.H.Gardner and J.P.Boris, "Influence of nonuniform laser intensities on ablatively accelerated targets", Phys. Rev. Lett. **48** 253 (1982).

[38] G.A.Magelssen and W.P.Gula, "Scaling laws for single-shell DT gas-filled spherical target for heavy-ion fusion", Phys. Fluids **25** 898 (1982).

[39] R.C.Davidson, *High Energy Density Physics* (The Natinal Academics Press, Washington D.C., 2003).

[40] F.C.Young, D.Mosher, S.J.Stephanakis, S.A.Goldstein and T.A.Mehlhorn, "Measurements of enhanced stopping of 1-MeV deuterons in target-ablation plasmas", Phys. Rev. Lett. **49** 549 (1982).

[41] K.A.Long and N.A.Tahir, "Range shortening, radiation transport, and Rayleigh-Taylor instability phenomena in ion-beam-driven inertial-fusion-reactor-size targets: Implosion, ignition, and burn phases", Phy. Rev. A **35** 2631 (1987).

[42] T.A.Mehlhorn, "A finite material temperature model for ion energy deposition in ion-driven inertial confinement fuison targets", J. Appl. Phys. **52** 6522 (1981).

[43] T.A.Mehlhorn, J.M.Peek, E.J.McGuire, J.N.Olson and F.C.Young, "Current status of calculations and measurements of ion stopping power in ICF plasmas", Sandia National Laboratories Report, No. SAND83-1519 (1983).

[44] T.Peter and J.Meyer-ter-Vehn, "Energy loss of heavy ions in dense plasma I. Linear and nonlinear Vlasov theory for the stopping power", Phys. Rev. A **43** 1998 (1991).

[45] T.Peter and J.Meyer-ter-Vehn, "Energy loss of heavy ions in dense plasma II. Nonequilibrium charge states and stopping powers", Phys. Rev. A **43** 2015 (1991).

[46] Chi-Kang Li and R. D. Petrasso, "Charged-particle stopping powers in inertial confinement fusion plasmas", Phys. Rev. Lett. **70** 3059 (1993).

[47] M.Murakami and J.Meyer-ter-Vehn, "Radiation symmetrization in indirectly driven ICF targets", Nuclear Fusioin **31** 1333 (1991).

[48] P.Wang, T.M.Mehlhorn and J.J.MacFarlane, "A unified self-consisten model for calculating ion stopping power in ICF plasma", Phys. Plasmas **5** 2977 (1998).

[49] K.A.Long and N.A.Tahir, "Heavy ion beam ICF fusion: The thermodynamics of ignition and the achievement of high gain in ICF fusion targets", Phy. Lett. A **91** 451 (1982).

[50] P.W.Petzoldt, D.T.Goodin, A.Nikroo, E.Stephens, N.Siegel, N.B.Alexander, A.R.Raffray, M.Tillack, F.Najmabadi, S.I.Krasheninnikov and R.Gallix, "Direct drive target survival during injection in an inertial fusion energy power plant", Nuclear Fusion **42** 1351 (2002).

[51] R.A.Sacks, R.C.Arnold and G.R.Magelssen, "Irradiation uniformity of spherical heavy-ion-driven ICF targets", Nuclear Fusion **22** 1421 (1982).

[52] M.H.Emery, J.H.Gardner, R.H.Lehmberg and S.P.Obenschain, "Hydrodynamic target response to an induced spatial incoherence-smoothed laser beam", Phys. Fluids B **3** 2640 (1991).

[53] A.I.Ogoyski, T.Someya and S.Kawata, "Code OK1 - Simulation of multi-beam irradiation on a spherical target in heavy ion fusion", Comp. Phys. Comm. **157** 160 (2004).

[54] F.Xiao, "Implementations of multi-fluid hydrodynamic simulations on distributed memory computer with a fully parallelizable preconditioned Bi-CGSTAB method", Comp. Phys. Comm **137** 274 (2001).

[55] Y.Ogata and T.Yabe, "Shock capturing with improved numerical viscosity in primitive Euler representation", Comp. Phys. Comm. **119** 179 (1999).

[56] H.Takewai and T.Yabe, "The cubic-interpolated pseudo particle method: application to nonlinear and multi-dimensional hyperbolic equations", J. Comp. Phys. **70** 355 (1987).

[57] T.Utsumi, T.Kunugi and T.Aoki, "Stability and accuracy of the cubic interpolated propagation scheme", Comp. Phys. Comm. **101** 9 (1997).

[58] F.Xiao, T.Yabe and T.ITo, "Constructing oscillation preventing scheme for advection equation by rational function", Comp. Phys. Comm **93** 1 (1996).

[59] F.Xiao, T.Yabe, G.Nizam and T.Ito "Constructing a multi-dimensional oscillation preventing scheme for the advection equation by a rational function ", Comp. Phys. Comm **94** 103 (1996).

[60] C.W.Hirt, A.A.Amsden and J.L.Cook, "An arbitrary lagrangian-Eulerian computing method for all flow speeds", J. Comp. Phys. **135** 203 (1997).

[61] M.Kucharik, J.Limpouch, R.Liska and P.Vachal, "ALE simulations of high-velocity impact problem", Czech. J. Phys. **54** 391 (2004).

[62] A.L.Nichols, R.Couch, J.D.Maltby, R.C.McCallen, I.Otero and R.Sharp, "Coupled thermal/chemical/mechanical modeling of energetic materials in ALE3D", UCRL-JC-124706 (1996).

[63] M.L.Wilkins, "Use of artifical viscosity in multidimensional fluid dynamic calculaitons", Comp. Phys. **36** 281 (1980).

[64] J.P.Christiansen, D.E.T.F.Ashby and K.V.Roberts, "MEDUSA a one-dimensional laser fusion code", Comp. Phys. Comm. **7**, 271 (1974).

[65] N.A.Tahir, K.A.Long and E.W.Laing, "Method of solution of a three-temperature plasma model and its application to inertial confinement fusion target design studies", J. Appl. Phys. **60** 898 (1986).

[66] N.A.Tahir and R.C.Arnold, "Radiation-driven inertial fusion targets for implosion experiments: Theorical analysis and numerical simulations", Phys. Fluids B **3** 1717 (1991).

[67] G.S.Fraley, E.J.Linnebur, R.J.Mason and R.L.Morse, "Thermonuclear burn characteristics of compressed deuterium-tritium microsphers", The Physics of Fluids **17** 474 (1974).

[68] N.J.Turner and J.M.Stone, "A module for radiation hydrodynamic calculations with ZEUS-2D using flux-limited diffusion", Astr. J. Supp. Series **135** 95 (2001).

[69] T.A.Brunner, "Forms of approximate radiation transport", Sandia National Laboratories Report, No.SAND2002-1778 (2002).

[70] T.Watanabe and H.Akao, "Analytical curve fitting for maxwellian reactivities", J.Plasma Fusion Res. **74** 850 (1998).

[71] K.Nozaki and K.Nishihara, "Thermonuclear reaction wave in high-density plasma", J. Phys. Soc. Jpn. **43** 1393 (1977).

[72] N.Asano, K.Nishihara, K.Nozaki and T.Taniuti, "Weak thermonuclear reaction wave in high-density plasma", J. Phys. Soc. Jpn. **41** 1774 (1976).

[73] N.A.Tahir and K.A.Long, "MEDUSA-KA: A one-dimensional computer code for inertial confinement fusion target design", report of KfK, KfK3454 (1983).

Appendix A

Achievement

A.1 Journal papers

1. T.Someya, S.Kawata, T.Nakamura, A.I.Ogoyski, K.Shimizu and J.Sasaki, "Beam final transport and direct drive pellet implosion in heavy ion fusion", Fusion Science and Technology, **43** 282 (2003).

2. S.Kawata, T.Someya, T.Nakamura, S.Miyazaki, K.Shimizu and A.I.Ogoyski, "Heavy ion beam final transport through an insulator guide in heavy ion fusion", Laser and Particle Beams, **21** 27 (2003).

3. A.I.Ogoyski, T.Someya, S.Kawata and T.Sasaki, "Heavy ion beam irradiation non-uniformity in inertial fusion", Physics Letter A, **315** 372 (2003).

4. J.-L.Vay, S.Kawata, T.Nakamura, J.Sasaki, T.Someya and C.Deutsh, "Conducting versus insulating walls in a heavy ion reaction chamber", Laser and Particle Beams, **21** 41 (2003).

5. T.Someya, A.I.Ogoyski, S.Kawata and T.Sasaki, "Heavy ion beam illumination on a direct-driven pellet in heavy-ion inertial fusion", Physical Review ST-AB, **7** 044701-1 (2004).

6. A.I.Ogoyski, T.Someya and S.Kawata, "Code OK1-Simulation of multi-beam irradiation on a spherical target in heavy ion fusion", Computer Physics Comm., **157** 160 (2004).

7. T.Someya, A.I.Ogoyski, S.Kawata and T.Sasaki, "Heavy ion beam illumination uniformity in heavy ion beam inertial confinement fusion", IEEJ. , **124** 85 (2004).

8. A.I.Ogoyski, S.Kawata and T.Someya, "Code OK2 A simulation code of ion illumination on an arbitrary shape and structure target", Computer Physics Comm., **161** 143 (2004).

9. A.I.Ogoyski, S.Kawata, T.Someya, A.B.Blagoev and P.H.Popov, "32-Beam irradiation on a spherical heavy ion fusion pellet", Journal of Physics D, **37** 2392 (2004).

10. T.Someya, S.Kawata, T.Kikuchi and A.I.Ogoyski, "HIB illumination on a target in HIF", Nucl. Inst. and Meth. in Phys. Res. A, **544** 406 (2005).

11. S.Kawata, R.Sonobe, T.Someya and T.Kikuchi, "Final beam transport in HIF", Nucl. Inst. and Meth. in Phys. Res. A, **544** 98 (2005).

12. T.Kikuchi, T.Someya and S.Kawata, "Beam pulse duration dependence on target implosion in heavy ion fusion", IEEJ., **125** 515 (2005).

A.2 International conferences

1. A.I.Ogoyski, T.Someya, T.Sasaki and S,Kawata, "Heavy ion beam illumination non-uniformity", Inertial Fusion Sciences and Applications 2003, Proc. Book p.694, Monterey, USA, Sep., 2003.

2. S.Kawata, T.Someya, A.I.Ogoysky and T.kikuchi, "Heavy ion beam illumination on an ICF direct-driven pellet", The 46th Annual Meeting of the Division of Plasma Physics, Bulletin of the APS p.338, Savannah, USA, Nov., 2004.

3. T.Someya, T,Kikuchi, K.Miyazaki, S.Kawata and A.I.Ogoyski, "HIB irradiation on direct-driven fuel target in heavy ion fusion", IEEE International Conference on Plasma Science, Abst. Book p.88, Monterey, USA, Jun., 2005.

4. T.Someya, T.Kikuchi, K.Miyazawa, S.Kawata and A.I.Ogoyski, "Heavy ion beam interaction with a direct-driven pellet", Inertial Fusion Sciences and Applications 2005, Proc. Book, Biarritz, France Sep., 2005.